University of Rhode Island

DigitalCommons@URI

2017

Experimental Studies on Mitigating the Risk of Air Blast Loading

Emad Ahmad Makki
University of Rhode Island, emakki@my.uri.edu

EXPERIMENTAL STUDIES ON MITIGATING THE

RISK OF AIR BLAST LOADING

BY

EMAD AHMAD MAKKI

A DISSERTATION SUBMITTED IN PARTIAL FULFILLMENT OF THE

REQUIREMENTS FOR THE DEGREE OF

DOCTOR OF PHILOSOPHY

IN

MECHANICAL ENGINEERING AND APPLIED MECHANICS

UNIVERSITY OF RHODE ISLAND

2017

DOCTOR OF PHILOSOPHY DISSERTATION

OF

EMAD AHMAD MAKKI

APPROVED:

Dissertation Committee:

Major Professor   Arun Shukla

David G. Taggart

K. Wayne Lee

Nasser H. Zawia
DEAN OF THE GRADUATE SCHOOL

UNIVERSITY OF RHODE ISLAND

2017

ABSTRACT

Blast loading events that arise from the detonation of explosives pose a severe threat to the lives of civilians and military personnel alike. Such dangers typical of a detonation event include but are not limited to an intense, sudden initial pressure spike, extreme temperatures due to the burning of gases released by the explosive, and damage to the integrity of surrounding structures. It is therefore the purpose of the studies detailed in this manuscript to investigate various methods of mitigating the dangers posed by shock loading, as well as to investigate a novel impact mitigation device.

To address the danger presented by high velocity glass fragments generated by windows that have failed due to shock loading, a study was conducted to evaluate the effectiveness of coated laminated safety glass panels' ability to contain glass fragments when subject to shock loading over a range of temperature conditions. Using a shock tube apparatus, fully clamped specimens were loaded under room temperature (25 °C), low temperatures (-10 and 0 °C), and high temperatures (50, 80, 110 °C). For each experiment, the incident and reflected shock wave pressure profiles were recorded and three-dimensional Digital Image Correlation was used to analyze high-speed images and compute the full-field deformation, in-plane strains, and velocities during the blast-loading event. A post-mortem study of the sandwich specimen was performed to investigate the effectiveness of such materials under different temperatures to withstand these shock loads. The composite panel showed great endurance during the blast loading for temperatures from 0 to 80 °C, however was unable to contain glass fragments at -10 °C and 110 °C.

A new system was designed to mitigate the impact forces during a collision using shock loading. The device consists of a cylindrical composite bladder sealed on one end by an inflation valve and on the other by an aluminum sheet of variable thickness. The bladder is pressurized and as an impactor nears the device, it strikes a striker-needle which ruptures the aluminum sheet, thus producing a shockwave just prior to impact. This produced shock wave decelerates the impactor and creates momentum (impulse) opposing that impulse transmitted from the impactor. Drop weight experiments were performed to show the applicability of this anti-shock device in reducing the momentum of the incoming body. A range of variables including needle length, bladder pressure, impact velocity, and drop mass were tested to better understand the processes involved. Time lapse photography coupled with 2D Digital Image Correlation (DIC) was used to obtain the striker full field motion data during the drop-weight experiments. It was found that the device effectively mitigates impact for higher impact velocities and for higher bladder pressures, decreasing peak loads during impact by up to 58% and energy imparted on the structure by 40%.

An experimental study was also conducted to examine the induced pressure from the interaction of a planar shock front and perforated plates under fixed and free-standing boundary conditions using the shock-tube facility. Two series of experiments with variations in the blockage ratio, net hydraulic diameter, shapes, and sizes of the orifices, were conducted. During each experiment, pressure histories caused by the interaction of the incident shock wave with the plates were recorded. During the fluid structure interaction time, the side-view images of the targets were recorded using a single high-speed camera to identify the motion response of each plate configuration.

The influence of varying the incident shock wave Mach number on the pressure profile was examined under clamped boundary conditions. The experimental results show that as the blockage ratio of the freestanding perforated plate decreased from 100% to 65%, the reflected peak pressure decreased by 26%, and the maximum impulse imparted to the perforated plate decreased by 33%. During the fluid-structure interaction process, as the blockage ratio of the freestanding perforated plate decreased from 100% to 65%, the plate's momentum, velocity and kinetic energy decreased by approximately 60%, 61%, and 84% respectively.

Finally, investigations were conducted to investigate the performance of different surface roughness (R_a) of 1018 mild low carbon steel panels under blast loading. Specimens were machined to have three different surface finishes of 0.8, 1.4, and 5.0 µm. The shock tube apparatus was utilized to generate controlled blast loadings on simply supported specimens. For each experiment, incident and reflected shock wave pressure profiles were recorded, and three-dimensional Digital Image Correlation was used to analyze high-speed images and compute the full-field deformation, in-plane strains, and velocities during the blast loading event. In addition, another high speed camera was utilized to record the side-view deformation images and this information was used to validate the data obtained from the 3D stereovision DIC technique. The results indicated that the impulse imparted to the plate decreased as the surface roughness increased from 0.8 µm to 5.0 µm. Due to this impulse reduction along with high surface roughness, the plates demonstrated a decrease in back face deflection, in-plane strain and out-of-plane velocity.

ACKNOWLEDGMENTS

First, and foremost, sincere thankfulness and praise are due to almighty ALLAH, who bestowed upon me the ability and skills to accomplish this Ph.D. dissertation. Second, the completion of this Ph.D. dissertation and extensive body of work behind it would not have been possible without the positive supportive involvement of the people and organizations acknowledged below.

I would like to thank Dr. Arun Shukla for his continuous guidance and support throughout this research. He is not only an outstanding professor and mentor, but a truly inspirational human being. It has been an honor for me to be one of his Ph.D. students. I am gratefully indebted for his trust in my research skills to be a part of such a significant area of study. Since my start at The University of Rhode Island and throughout all phases of my academic and research studies, Prof. Arun Shukla has generously provided me with his expertise, invaluable knowledge, insights, guidance, support, encouragement, enthusiasm, and enlightening inspiration. I also gratefully appreciate his enthusiastic supervision style, which has made me a better researcher by providing me with guidance, support, encouragement, and time to publish and present the results of this work nationally and internationally throughout the course of my Ph.D. journey.

I would also like to sincerely thank Dr. David G. Taggart, Dr. K. Wayne Lee, and Dr. Sumanta Das for agreeing to serve as my committee members. Many thanks also due to Dr. Murat Yazici and Dr. Idris Karen for their continuous assistance and valuable suggestions and comments. Also a special thanks to Dr. D.M.L. Meyer for her guidance and enthusiasm for teaching.

PREFACE

This dissertation presents experimental studies of various blast and impact mitigation techniques. This dissertation is prepared using the manuscript format. This dissertation is carried out in different stages, with each chapter specifically analyzing a particular problem in detail. The aforementioned chapters are namely the response of coated laminated glass panels subjected to combined blast and temperature loadings; novel impact mitigation technique using shock loading; blast performance of perforated structures; the influence of surface roughness on blast mitigation.

Chapter 1 provides an overview of previous and current published literature of subject matter relevant to this dissertation. Topics include a brief background on different blast mitigation techniques and why they are important in the naval, aerospace and defense industry. This chapter also serves to provide an overview of the relevant research in literature, the possible data gaps that exist, as well as an introduction to the studies within this dissertation.

Chapter 2 details the results of blast-loading experiments conducted on coated laminated safety glass (LSG) panels subject to a range of temperature conditions. The sandwich composite consists of a PVB interlayer; two glass panels; and outer protective films. As concluded by many studies, the majority of human harm caused by shock-loading events is not a result of the shock-wave directly, but of unsecured objects such as glass shards that are propelled at high velocities by the shockwave. As such, it is the purpose of LSG panels to, rather than mitigates blast, secure any glass fragments that might otherwise be propelled at lethal velocities by the shock wave. It is therefore imperative that the aforementioned PVB interlayer remain intact. The

purpose of this chapter was to characterize tensile behavior of the coating material subject to blast loading as a function of temperature. It was found that, generally speaking, the presence of the coating has a major influence on the LSG's ability to contain glass fragments generated by shock loading. More specifically, the most effective containment was achieved between 0 ℃ and 80 ℃, and the coating experienced failure at -10 ℃ and 110 ℃. This chapter follows the formatting guidelines specified by *the Journal of Dynamic Behavior of Materials*.

Chapter 3 presents a novel anti-shock device intended to mitigate the effects of normal impact loading, and details the results of drop-test experiments performed to simulate impact loading imparted onto the device. The device mitigates the impact loading by releasing an opposing shock wave just prior to the impact, thus reducing the effect of the impact load. Results of the drop-test experiments conducted conclude that the device can reduce peak load by as much as 58%, and can reduce the energy imparted on a structure by up to 40%. This chapter has been prepared for submission to *the Journal of Experimental Techniques*.

Chapter 4 examines the induced pressure from the interaction of a planar shock front and perforated plates under different boundary conditions using the shock-tube facility. Two series of experiments with variations in the blockage ratio, net hydraulic diameter, shapes, and sizes of the orifices, were conducted. In the first part of this study, shock wave loading experiments on free standing perforated plates were conducted to evaluate the reflected pressure pulses and the motion response for all the targets with and without perforations. The second part of this study conducted on clamping all of the targets inside the shock-tube to evaluate the reflected and

transmitted pressure pulses. During each experiment, pressure histories caused by the interaction of the incident shock wave with the plates were recorded. The side-view images of the targets were recorded using a single high-speed camera to identify the motion response of each plate configuration. This chapter has been prepared for submission to *the Journal of Engineering Structures.*

Chapter 5 details the results of blast-loading experiments conducted on different surface roughness of 1018 mild low carbon steel panels. These experiments were performed to understand the potential use of changing the surface texture of the panels and reducing the total work done by the shock load, thus improving the overall structural response. Specimens were machined to have three different surface finishes of (0.8, 1.4, and 5.0) μm. The shock tube apparatus was utilized to generate controlled blast loadings. The real-time deformation of the specimens was recorded using two high-speed cameras. Three-dimensional Digital Image Correlation was used to analyze the high-speed images and compute the full-field deformation, in-plane strains, and velocities during the blast-loading event. The results indicated that the impulse imparted to the plate decreased as the surface roughness (R_a) increased from 0.8 μm to 5.0 μm. Due to this impulse reduction along with high surface roughness, the plates demonstrated a decrease in back face deflection, in-plane strain and out-of-plane velocity. This chapter has been prepared for submission to *the Journal of Impact Engineering*.

Chapter 6 provides some suggestions for future work to compliment or enhance the studies contained within this dissertation.

TABLE OF CONTENTS

LIST OF TABLES

CHAPTER 3

CHAPTER 4

LIST OF FIGURES

CHAPTER 2

CHAPTER 3

CHAPTER 4

CHAPTER 5

CHAPTER 1: INTRODUCTION AND LITERATURE REVIEW

In recent years, global conflicts have sparked an urgent necessity to research and develop innovative and effective methods of air blast mitigation. Specifically with regards to the recent surge in terrorist attacks carried out against both military personnel and civilians alike, which include but are not limited to Improvised Explosive Devices and Rocket Propelled Grenades, it has become necessary to develop more effective passive and active methods of mitigating the air blast waves generated by the detonation of such explosives. However, applications of blast mitigation techniques are not limited to military and defense applications. Blast and impact mitigation are also very relevant in process industry and in transportation, in which accidents can occur in the form of blast or impact loading events. It is, given this need, the purpose of the work detailed in this manuscript to investigate and analyze various methods of mitigating the effects of blast loading, as well as investigates a novel impact-mitigation device.

In order to better understand some of the topics that will be discussed in this chapter and those that follow, one must understand the difference between active and passive mitigation techniques. An active mitigation system is any mitigation technique that relies on a certain outside stimulus in order to be initiated [1, 2]. A basic example of this is an airbag system in an automobile, an impact mitigation system, which relies on input from sensors that detect a crash impact, thereby initiating deployment of the airbag [3-8]. Another example would be the water deluge systems utilized in UK offshore oil and gas platforms, which rely on sensors to detect gas leaks, and thereby initiating the release of water droplets into leak areas in order to mitigate the risk of a

gas explosion [9]. Current innovations in this area include the work conducted by the Defense Research Council, which has investigated panels filled with cells containing isolated chemical agents which act as a propellant when they interact. Thus, if the panel is subject to a blast loading effect, the cells rupture and the interaction is initiated, thus generating a gas buffer which opposes the blast wave [1]. While they can be effective, it can be seen that the processes and equipment required for active mitigations can be quite extensive and complex, and therefore costly. Furthermore, it is necessary in most cases that the system be initiated immediately upon impact, a feat which is difficult to achieve for most sensors. For these reasons, the more simple passive mitigation techniques are often preferred [2].

Passive mitigation systems do not rely on sensor input or other outside stimulus to be initiated, and instead utilize structural properties built into the design of the system [2]. This makes the passive system simpler and eliminates any reaction time between the event and the response. Common techniques employed in passive systems include impedance mismatching, sacrificial cladding, blast deflection, and blast and shockwave disruption [2]. One noteworthy example of a passive blast mitigation technique which utilizes impedance mismatching techniques consists of elastomeric layers containing air-filled microspheres [10]. Another good example of a passive blast mitigation technique which uses a water cavity between the incident blast wave and the structure to be protected was proposed by Shin et al. The authors identified that placing a water cavity delays the shock front and minimizes the magnitude of initial peak shock pressure by 40% [11].

With regards to blast mitigation, it is important to recognize that the phenomena generated by explosion events which pose a threat to human life are not limited to the high peak pressures that are a result of the initial explosion [12-14]. Clearly these peak pressures are harmful to humans and are thus their mitigation a topic of investigations detailed in this work, however succeeding events such as high temperatures produced from burning gasses, secondary debris and fragments, direct impact, and the compromise of structural integrity of surrounding structures also pose a significant threat and thus are also addressed in this work.

Chapter 2 of this manuscript addresses the problem of debris generated by harm to structures during a blast loading event, detailing the investigations and analysis of a passive mitigation technique in the form of sandwich structures designed to contain glass fragments generated from blast-loaded windows. Sandwich structures have proved useful in Naval and Aerospace applications due to their high stiffness to weight ratio and energy absorption capabilities [15-22], and thus it can be considered that similar configurations will have similar qualities when applied to glass structures. According to Wang et al, when sandwich structures are subjected to high-intensity impulse loadings, the core materials play a crucial role in the dynamic behavior and overall structural response [15]. The core properties assist in dispersing the mechanical impulse that is transmitted into the structure, and thus protect anything located behind it [15]. As concluded by many studies, the majority of human harm caused by shock-loading events is not a result of the shock-wave directly, but of unsecured objects such as glass shards that are propelled at high velocities by the shockwave [23-25]. Monolithic glass panes, necessary as they are, are often the culprit

in these sorts of injuries due to the fact that they offer little resistance to air blast loads. Thus, the development of blast-resistant windows has been a topic of interest among many researchers all over the world. There are many different types of blast-resistant panels, including clear, wired, tempered, and laminated safety glass (LSG) panels [26]. In comparison to most of the commercial glass panels, LSG panels have been proven to have better blast and impact resistance and hence have been the central focus of research on blast resistant windows [27-29]. Typical LSG panel consists of two glass plates bounded together by a polyvinyl butyral (PVB) polymer interlayer [30]. This interlayer holds the glass splinters and continues to deform significantly after the glass fractures, in which case, the composite structure exhibits large deformations and dissipates the blast energy. A recent investigation by P. Kumar and Shukla reported that a sandwich configuration consisting of a PVB interlayer, two glass panels, with outer protective films was the most effective at mitigating blast-loadings compared to other glass systems, such as tempered glass, wired glass, and LSG [29]. This promising sandwich structure needs more research to investigate the bounds of its utility. Thus, in this dissertation we aimed to evaluate the blast performance of this sandwich structure in a variety of temperature environments. It was found that, generally speaking, the presence of the coating has a major influence on the LSG's ability to contain glass fragments generated by shock loading. Considered across varying temperature conditions, the most effective containment was achieved between 0 ℃ and 80 ℃, and the coating experienced failure at -10 ℃ and 110 ℃.

Chapter 3 of this manuscript details the design and investigations conducted on a novel impact mitigation device. Such a device would be quite applicable to industries such as the transport industry, where impacts between civilians and transport vehicles (cars, trains, etc.) are responsible for numerous injuries and fatalities in the US and across the world [31]. Thus, creating devices that mitigate such impact have been the subject of many investigations [32-36]. The device consists of a cylindrical composite bladder sealed on one end by an inflation valve and on the other by an aluminum sheet of variable thickness. The bladder is pressurized and as an impactor nears the device, it strikes a striker-needle, which ruptures the aluminum sheet, thus producing a shockwave just prior to impact. This produced shock wave decelerates the impactor and creates momentum (impulse) opposing that impulse transmitted from the impactor, much like the reactant-filled panels discussed earlier in this chapter [1]. Drop weight experiments were performed to show the applicability of this anti-shock device in reducing the momentum of the incoming body. A range of variables including needle length, bladder pressure, impact velocity, and drop mass were tested to better understand the processes involved. It was found that the device effectively mitigates impact for higher impact velocities and for higher bladder pressures, decreasing peak loads during impact by up to 58% and energy imparted on the structure by 40%.

Chapter 4 of this manuscript details investigation conducted on the passive blast mitigation technique of applying perforations of various parameters to affected surfaces. Previous studies conducted by Ben-Dor et al have shown that orifice plates and grids can successfully mitigate the effects of shock loading [37-40]. Further, more

specific studies were conducted by Langdon et al, showing similar successes while using steel perforated plates to mitigate blast loading travelling down a tube while also showing that the damage imparted to the plate itself was reduced in the presence of perforations [2, 41, and 42]. Similar pressure-mitigating behaviors have been observed in Nano-structured porous materials [43] and reticulated foam [44]. While all previous studies revolve around fixed perforated plates, it is the purpose of this work to expand upon previous knowledge by observing the behavior of free-standing perforated plates. To do this, the identical perforated plates with varying perforation specifications were tested for both fixed and freestanding conditions, and the results observed. It was determined that pressure profiles at various distances from the plate behaved similarly for freestanding plates as with fixed plates.

Finally, Chapter 5 of this manuscript investigates a passive blast mitigation technique which holds the added benefit of being cost effective and easy to implement. This chapter details a series of blast experiments conducted on steel panels with varying degrees of surface roughness. Prior literature has explored the problem of shock wave interaction on the boundary layer over a rough wall in transonic circular bump geometry [45, 46]. However, shock being normally loaded or impinged onto a rough surface structure (as is typical with an explosive event) has not previously been investigated even though it is of importance in any treatment of shock wave attenuation. A 2-D numerical model, which is simulating interactions between a blast wave and a V-shaped or a cone-shaped structure, was developed by W. Peng et al. [47]. Normal, oblique, and Mach stem reflections are types of reflection when a blast wave impinges on a surface. The Normal reflection occurs when the incident angle is

0°. The angle between the incident shock front and the reflecting surface of a structure is defined as the incident angle [47]. The authors reported that when the incident angle is greater than 40°, Mach stem reflection occurred. The Mach stem reflection resulted in noteworthy decrease of reflected pressure, as well as the transmitted impulse. The influence of Mach stem reflection in reducing blast wave impact decreased with the decrease of blast intensity [47]. Based on results from shock loading experiments, conducted in this chapter, it was determined that blast mitigation improves as surface roughness increases, insofar as damage to the structure itself is concerned. That is to say, specimens with higher surface roughness values deformed less than specimens with lower surface roughness values when subject to the same loading.

REFERENCES

[1] Wadley, H. N. G., Dharmasena, K. P., He, M. Y., McMeeking, R. M., Evans, A. G., Bui-Thanh, T., & Radovitzky, R. (2010). An active concept for limiting injuries caused by air blasts. International Journal of Impact Engineering, 37(3), 317–323

[2] Langdon, G. S., Nurick, G. N., Balden, V. H., & Timmis, R. B. (2008). Perforated plates as passive mitigation systems. Defence Science Journal, 58(2), 238–247

[3] Zhang, G., Cao, L., Hu, J. and Yang, K. H. (2008). A field data analysis of risk factors affecting the injury risks in vehicle-to-pedestrian crashes. Annual Proceedings / Association for the Advancement of Automotive Medicine. Association for the Advancement of Automotive Medicine, 52, 199−214

[4] Broggi, A., Cerri, P., Ghidoni, S., Grisleri, P., & Jung, H. G. (2009). A new approach to urban pedestrian detection for automatic braking. IEEE Transactions on Intelligent Transportation Systems, 10(4), 594–605

[5] Carsten, O. M. J., & Tate, F. N. (2005). Intelligent speed adaptation: Accident savings and cost-benefit analysis. Accident Analysis and Prevention, 37(3), 407–416

[6] Lim, J. H., Park, J. S., Yun, Y. W., Jeong, S. B., & Park, G. J. (2015). Design of an airbag system of a mid-sized automobile for pedestrian protection. Proceedings of the Institution of Mechanical Engineers Part D-Journal of Automobile Engineering, 229(5), 656–669

[7] Yang, H.-I., Yun, Y.-W., & Park, G.-J. (2015). Design of a pedestrian protection airbag system using experiments. Proceedings of the Institution of Mechanical Engineers, Part D: Journal of Automobile Engineering

[8] Choi, S., Jang, J., Oh, C., & Park, G.-J. (2016). Safety benefits of integrated pedestrian protection systems. International Journal Of Automotive Technology, vol 17, Springer Nature, pp 473–482

[9] Pritchard D.K. (2006). Review of explosion mitigation measures for platform legs, 44(0). Health and Safety Laboratory Report No. HSL/2006/64

[10] Composite floor armour for military tanks and the like. US Patent No. USP 4404889.

[11] Shin, Y. S., Lee, M., Lam, K. Y., & Yeo, K. S. (1998). Modeling mitigation effects of water shield on shock waves. Shock and Vibration, 5(4), 225–234

[12] H. Scott Norville, GRTL (1987) Misty picture data: window glass experiment, final data report, Glass Research and Testing Laboratory, Texas Tech University, Lubbock, TX

[13] Norville HS, Harvill N, Conrath EJ, et al. (1999) Glass-Related Injuries in Oklahoma City Bombing. Journal of Performance of Constructed Facilities 13:50–56

[14] Smith D (Tampere, Finland, 2001) Glazing for injury alleviation under blast loading, United Kingdom practice. In Glass Processing Days Conference Proceedings, 335–340

[15] Wang, E., Gardner, N., & Shukla, A. (2009). The blast resistance of sandwich composites with stepwise graded cores. International Journal of Solids and Structures, 46(18–19), 3492–3502

[16] Ajdari, A., Jahromi, B. H., Papadopoulos, J., Nayeb-Hashemi, H., & Vaziri, A. (2012). Hierarchical honeycombs with tailorable properties. International Journal of Solids and Structures, 49(11–12), 1413–1419

[17] Dharmasena, K. P., Wadley, H. N. G., Xue, Z., & Hutchinson, J. W. (2008). Mechanical response of metallic honeycomb sandwich panel structures to high-intensity dynamic loading. International Journal of Impact Engineering, 35(9), 1063–1074

[18] Wadley, H. N. G., Dharmasena, K. P., O'Masta, M. R., & Wetzel, J. J. (2013). Impact response of aluminum corrugated core sandwich panels. International Journal of Impact Engineering, 62, 114–128

[19] Rubino, V., Deshpande, V. S., & Fleck, N. A. (2008). The dynamic response of end-clamped sandwich beams with a Y-frame or corrugated core. International Journal of Impact Engineering, 35(8), 829–844

[20] Xue, Z., & Hutchinson, J. W. (2004). A comparative study of impulse-resistant metal sandwich plates. International Journal of Impact Engineering, 30(10), 1283–1305

[21] Fahr, P., Yazici, M., & Shukla, A. (2016). Shock response of filled corrugated sandwich structures under extreme temperatures. Journal of Sandwich Structures and Materials

[22] Gardner, N., Wang, E., & Shukla, A. (2012). Performance of functionally graded sandwich composite beams under shock wave loading. Composite Structures, 94(5), 1755–1770

[23] H. Scott Norville, GRTL (1987) Misty picture data: window glass experiment, final data report, Glass Research and Testing Laboratory, Texas Tech University, Lubbock, TX

[24] Norville HS, Harvill N, Conrath EJ, et al. (1999) Glass-Related Injuries in Oklahoma City Bombing. Journal of Performance of Constructed Facilities 13:50–56

[25] Smith D (Tampere, Finland, 2001) Glazing for injury alleviation under blast loading, United Kingdom practice. In Glass Processing Days Conference Proceedings, 335–340

[26] Stephens RAC (2008) Determination of the resistance of laminated glass subjected to blast loading using high speed video [M.Sc. thesis]. Cranfield University.

[27] Puneet Kumar, Arun Shukla (2011) Dynamic response of glass panels subjected to shock loading. Journal of Non-crystalline Solids - J NON-CRYST SOLIDS 357:3917–3923

[28] Shetty MS, Wei J, Dharani LR, Stutts DS (2013) Analysis of Damage in Laminated Architectural Glazing Subjected to Wind Loading and Windborne Debris Impact. Buildings 3:422–441

[29] Zhang X, Hao H, Wang Z (2015) Experimental study of laminated glass window responses under impulsive and blast loading. International Journal of Impact Engineering 78:1–19

[30] UFC 4-010-01 (2003) Minimum Antiterrorism Standards for Buildings, Unified Facilities Criteria, Department of Defense, Washington D.C., USA

[31] Paden, B. E., Kelly, P. M., Hines, J. A., Bothman, D., & Simms, C. (2016). On the feasibility of life-saving locomotive bumpers. Accident Analysis and Prevention, 89, 103–110

[32] Lee, Y. H., Joo, Y. J., Park, J. S., Kim, Y. S., & Yim, H. J. (2014). Robust design optimization of frontal structures for minimizing injury risks of Flex Pedestrian Legform Impactor. International Journal of Automotive Technology, 15(5), 757–764

[33] Mallory, A., Fredriksson, R., Rosén, E., & Donnelly, B. (2012). Pedestrian Injuries By Source: Serious and Disabling Injuries in US and European Cases. Association for the Advancement of Automotive Medicine. Association for the Advancement of Automotive Medicine. Scientific Conference, 56, 13–24.

[34] Matsui, Y. (2014). Possibility of installing a data acquisition system in a pedestrian headform impactor. International Journal of Crashworthiness, 19(2), pp 115-125

[35] Niebuhr, T., Junge, M., & Achmus, S. (2015). Expanding pedestrian injury risk to the body region level: how to model passive safety systems in pedestrian injury risk functions. Traffic Injury Prevention, 16(5), 519–31

[36] Lv, X., Huang, X., Gu, X., Liu, W., & Li, G. (2016). Reliability-based multiobjective optimisation of vehicle bumper structure holes for the pedestrian flexible legform impact. International Journal of Crashworthiness, 21(3), 198–210

[37] Britan, a., Karpov, a. V., Vasilev, E. I., Igra, O., Ben-Dor, G., & Shapiro, E. (2004). Experimental and Numerical Study of Shock Wave Interaction with Perforated Plates. Journal of Fluids Engineering, 126(3), 399

[38] Britan, A., Igra, O., Ben-Dor, G., & Shapiro, H. (2006). Shock wave attenuation by grids and orifice plates. Shock Waves, 16(1), 1–15

[39] Ram, O., & Sadot, O. (2013). A simple constitutive model for predicting the pressure histories developed behind rigid porous media impinged by shock waves. Journal of Fluid Mechanics, 718, 507–523

[40] Ram, O., & Sadot, O. (2015). Analysis of the pressure buildup behind rigid porous media impinged by shock waves in time and frequency domains. Journal of Fluid Mechanics, 779, 842–858

[41] Langdon, G. S., Rossiter, I. B., Balden, V. H., & Nurick, G. N. (2010). Performance of mild steel perforated plates as a blast wave mitigation technique: Experimental and numerical investigation. International Journal of Impact Engineering, 37(10), 1021–1036

[42] Langdon, G. S., Nurick, G. N., & du Plessis, N. J. (2011). The influence of separation distance on the performance of perforated plates as a blast wave shielding technique. Engineering Structures, 33(12), 3537–3545

[43] Al-qananwah, A. K., Koplik, J., Andreopoulos, Y., Al-qananwah, A. K., Koplik, J., & Andreopoulos, Y. (2013). Attenuation of shock waves propagating through nano-structured porous materials. Physics of Fluids, 76102(7)

[44] Wilgeroth, J. M., Nguyen, T.-T. N., & Proud, W. G. (2014). Interaction between blast wave and reticulated foam: assessing the potential for auditory protection systems. Journal of Physics: Conference Series, 500(10), 102005

[45] Arun Kumar R, H.D Kim. (2013). Wall Roughness Effects on Shock Boundary Layer Interaction Flows, International Journal of Innovative Research in Science, Engineering and Technology, 2(1), 387–394

[46] J. Mendonca & M.A.R. Sharif (2010) Effects of Surface Roughness on Turbulent Transonic Flow Over Circular Arc Bumps in a Channel, Engineering Applications of Computational Fluid Mechanics, 4:2, 164-180

[47] Peng, W. (2009). Modeling And Simulation Of Interactions Between Blast Waves And Structures For Blast Wave Mitigation. Mechanical (and Materials) Engineering--Dissertations and Student Research

.

CHAPTER 2: RESPONSE OF COATED LAMINATED GLASS PANELS SUBJECTED TO COMBINED BLAST AND TEMPERATURE LOADINGS

by

Emad A. Makki, Prathmesh Naik Parrikar and Arun Shukla

Corresponding Author: Emad A. Makki

      Dynamic Photo Mechanics Laboratory

      Department of Mechanical, Industrial and Systems

      Engineering

      University of Rhode Island

      94 Upper College Road

      131 Kirk Applied Engineering Laboratory

      Kingston, RI, 02881, USA

      Phone: +1-401-874-2283

      Email Address: emakki@my.uri.edu

Abstract

An experimental study was conducted to investigate the performance of coated laminated safety glass panels under extreme temperatures and blast loading. Using a shock tube apparatus, specimens were evaluated under room temperature (25 °C), low temperatures (-10 and 0 °C), and high temperatures (50, 80, 110 °C). Special environmental chambers were designed to heat up and cool down the panels to the required temperatures prior to blast loading. To mimic real applications for glass windows, specimens were clamped fully along the boundaries during experimentation. For each experiment, the incident and reflected shock wave pressure profiles were recorded using pressure transducers located on the muzzle of the shock tube. The real-time deformation of the sandwich specimens was recorded using two high-speed cameras. Three-dimensional Digital Image Correlation was used to analyze the high-speed images and compute the full-field deformation, in-plane strains, and velocities during the blast-loading event. A post-mortem study of the sandwich specimen was performed to investigate the effectiveness of such materials under different temperatures to withstand these shock loads. Experiments were conducted to characterize the tensile behavior of the coating material as a function of temperature. The mechanisms of failure of the panel are in agreement with the failure mechanisms outlined for laminated safety glass (LSG) in previous studies. The results indicated that polymeric thin sheet coating on both outer faces of the LSG panel had major influence on mitigating the blast loading and containing the glass fragments. The composite panel showed great endurance during the blast loading for temperatures from 0 to 80 °C. The failure of panel at -10 °C is attributed to the glass transition of

15

the coating material and the failure at 110 °C is likely due to the tearing of the coating by the glass fragments.

1. Introduction

Most post-investigations of incidents involving explosions have cited that the majority of human casualties were not caused by the air blast wave or bomb fragments them-selves. Rather, it was fragments of objects coming from glass windows, walls, and other unsecured bodies that were responsible for the majority of human injury [1-3]. Monolithic glass panes, necessary as they are, are often the culprit in these sorts of injuries due to the fact that they offer little resistance to air blast loads. Thus, the development of blast-resistant windows has been a topic of interest among many researchers all over the world.

There are many different types of blast-resistant panels, including clear, wired, tempered, and laminated safety glass (LSG) panels [4]. In comparison to most of the commercial glass panels, LSG panels have been proven to have better blast and impact resistance and hence have been the central focus of research on blast resistant windows [5-7]. Typical LSG panel consists of two glass plates bounded together by a polyvinyl butyral (PVB) polymer interlayer. This interlayer holds the glass splinters and continues to deform significantly after the glass fractures, in which case, the composite structure exhibits large deformations and dissipates the blast energy. In accordance with popular blast-proof window designs specified by the Department of Defense UFC standard [8] and the ASTM standard [9], 3 mm thick glass panes are

16

used in the LSG panel. It was proven by Wei et al. that the most effective PVB thickness for blast mitigation is any number between 0.76 mm and 1.52 mm [10], resulting in a configuration with minimal thickness of 6.76 mm for the LSG panel.

Experimental studies have been conducted to understand the response of laminated glass panes and its performance under blast loading. Larcher et al. [11] described the general behavior and failure modes of LSG under blast loading. Initially, glass panes deform elastically and absorb some of the blast energy where the outer glass ply cracks and the inner one breaks. The PVB interlayer deforms elastically and then plastically. The failure of the interlayer occurs at ultimate strain or is cut by the glass fragments. Hooper et al. [12, 13] performed open-air blast experiments to provide full field deflection measurements at all points across the LSG panel using high-speed 3D digital image correlation (DIC) along with load measurements at the joints. The authors reported that the strain is concentrated near the edges and corners leading to tearing of the PVB around the edges. Wei et al. [14] studied the significant influence of the negative phase of the blast loading on the dynamic response of the glazing panel. They concluded that the mid-span deflection and stress caused by the negative phase could be as much as twice those caused by the positive phase. Zhang et al. [15] studied the boundary effects on the performance of LSG windows. They found that the sliding boundary, which allows longitudinal and in-plane movement of the panel, can effectively reduce the LSG response against the blast loading and also reduce the joint failure possibility as compared to fully fixed boundary.

Numerical studies of firmly clamped LSG panels by Zhang et al. [16] show three failure modes. Shear failure occurs on the interlayer along the boundary when it

17

is subjected to impulsive load with significant reflected pressure in short duration; flexural bending failure is expected when it is under relatively long duration loading; and a combined shear and flexural failure will be formed on the PVB interlayer if it is under intermediate dynamic loading. H.D. Hidallana-Gamage et al. [17] performed an analytical procedure using the maximum principle stress as the failure criterion for glass and the von mises stress as the failure criterion for interlayer and sealant materials to predict failure of LSG panel under blast loading. They reported that the glass panes absorb most of the blast energy. As a percentage of total energy absorption, glass panes showed 80% energy absorption, PVB interlayer had energy absorption of 12%, and the sealant joints showed 8% energy absorption most of the time. The authors concluded that LSG panels should be designed to fail by the tearing of the interlayer rather than failure at the supports to achieve a desired level of protection. Many researchers have studied the dynamic properties of glass [18, 19] and PVB materials [20, 21] to help design better glass resistant panels.

A recent investigation by P. Kumar and Shukla reported that a sandwich configuration consisting of a PVB interlayer, two glass panels, with outer protective films was the most effective at mitigating blast-loadings compared to other glass systems, such as tempered glass, wired glass, and LSG [5]. This promising sandwich structure needs more research to investigate the bounds of its utility. Thus, in this study we aim to evaluate the blast performance of this sandwich structure in a variety of temperature environments. A shock tube facility generated the dynamic shock loading imparted to the glass composites while a series of pressure sensors and high-speed cameras were used to obtain pressure profiles and images of the specimen

during loading at the different temperatures. Three-dimensional Digital Image Correlation (3D DIC) was used to analyze the high-speed images and compute the full-field deformation, in-plane strains, and velocities during the blast-loading event. The composite panel showed superior blast mitigating property for temperatures ranging from 0 to 80 °C. The polymeric thin sheet coating and PVB both contribute in containment of the glass fragments and withstand the blast load. The failure of the sandwich panel at -10 °C is attributed to the glass transition of coating material and the failure at 110 °C is likely due to the tearing of the coating by the glass fragments.

2. Experimental Procedures

In the present study, the performance and dynamic behavior of sandwich specimen under shock loading was evaluated. To verify consistency and repeatability in the experimental results, at least three blast-loading experiments were performed at each temperature environment. Experiments were carried out at temperatures of -10, 0, 25, 50, 80 and 110 °C.

2.1 Sandwich Specimen Geometry and Materials

The sandwich specimens used for shock loading experiments were prepared by adhering a protective film (provided by XO ARMOR® with a thickness of 0.279 mm) on both of the outer faces of the laminated safety glass (LSG) panel using a special chemical adhesive XO® bond. Figure 1a shows a detailed schematic for the sandwich specimen configuration. The LSG panel used in this study consists of two clear glass plates (each ply had thickness of 3.14 mm) made out of Soda–Lime–Silica Glass, which were bonded with 0.76 mm-thick transparent PVB interlayer as shown in Fig. 1a, b. The overall dimensions for the sandwich specimens were 305 mm long, 305 mm

wide and 7.6 mm thick. According to the laminated safety glass manufacturers, the PVB interlayer was first cut to the correct size and sandwiched between two clear glass plates. The sandwiched glass assembly was then passed along the production line where it moved through an oven while the air was being pressed out. After that, it was heated and pressurized in a computer-controlled autoclave for 24 hours. This treatment process yields good bonding strength and gives the glass plies clear optical properties. The XO® bond penetrates the glass and forms a permanent, nano-level molecular bond between the glass and the XO® film.
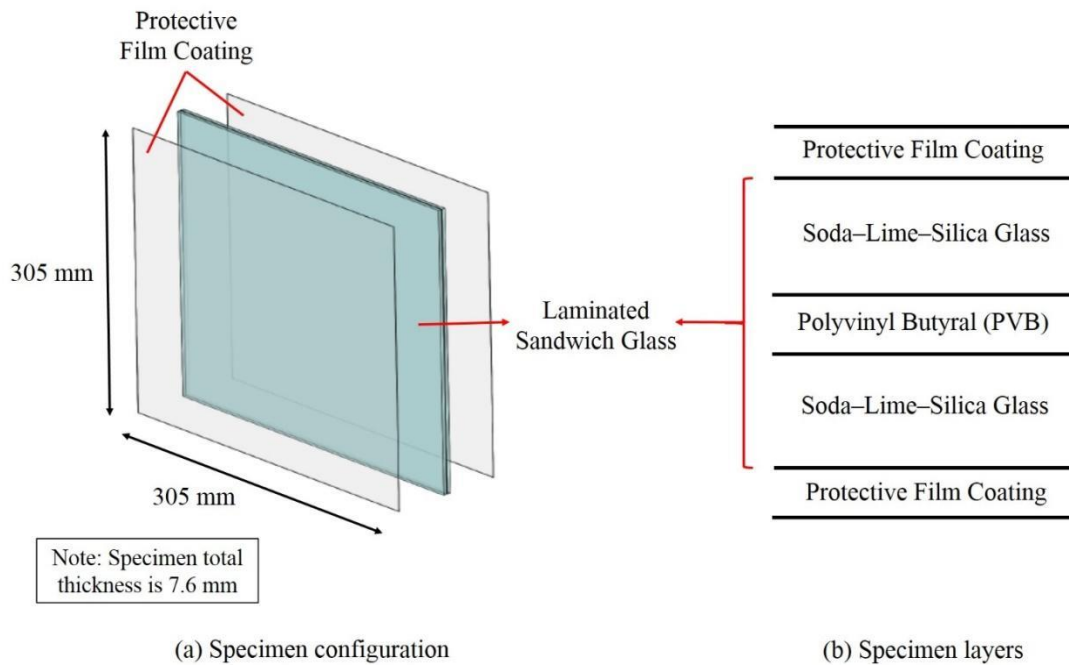
Fig. 1 Detailed schematic of sandwich specimen

2.2 Blast Loading Under Different Temperatures

The experiments were conducted using the shock tube apparatus, which can produce transient blast loading. The shock tube facility at the *University of Rhode Island,* shown in Fig.2, had already been developed and has the capability to generate a controllable shock wave loading on the target specimen up to a 2.2 MPa overpressure [22, 23]. In the present study, the shock tube had an overall length of 8m. It consists of three main sections: high pressurized (driver) section, low pressure (driven) section, and muzzle section. Both driver and driven sections had diameter of 0.15 m and they were separated by a diaphragm. The muzzle end was the final section of the shock tube facility and had diameter of 0.07 m.

Fig. 2 Shock tube facility

During the experiments, the driver section was pressurized with compressed Helium gas, creating a pressure difference across the diaphragm that is composed of a variable number of Mylar sheets. Thus the pressure needed to rupture the diaphragm is controlled by the quantity and thickness of the Mylar sheets. When the pressure reaches its critical value as determined by the Mylar, the diaphragm ruptures, forming a supersonic shock wave that travels towards the target specimen. The theoretical assumptions that were used to describe the gas flow in the shock tube and the detailed

compressible gas flow equations have been previously established in the literature [24, 25].

In order to investigate the actual loading conditions in windows, sandwich specimens were held under fully clamped boundary conditions during blast loading. A detailed fixture support design is shown in Fig. 3a. The inner dimensions of the clamping fixture (window frame) were 267 mm x 267 mm. Rubber supports were placed between the steel metal clamping supports and the sandwich specimen to avoid breaking any glass during the clamping process. The sandwich specimen was placed in the robust supports and positioned 0.1 mm away from the end of the muzzle section. The shock tube end muzzle was aligned so that its axis coincided with the center of the front face of the sandwich specimen. The blast loading was applied over a central circular area 76.2 mm in diameter. The pressure pulses were recorded by two pressure transducers (PCB CA102B) mounted at the muzzle exit, located with respect to the front face of the specimen as shown in Fig. 3b. These pressure sensors were kept separated by a distance of 160.0 mm and the closest pressure transducer to the specimen was located 20.0 mm away from the muzzle end. These sensors were installed to keep the front face of the sensor flush to the inner wall surface of the muzzle section. The incident and reflected shock wave velocities in the tube were obtained by using the distance between the transducers and the shock wave travel time.
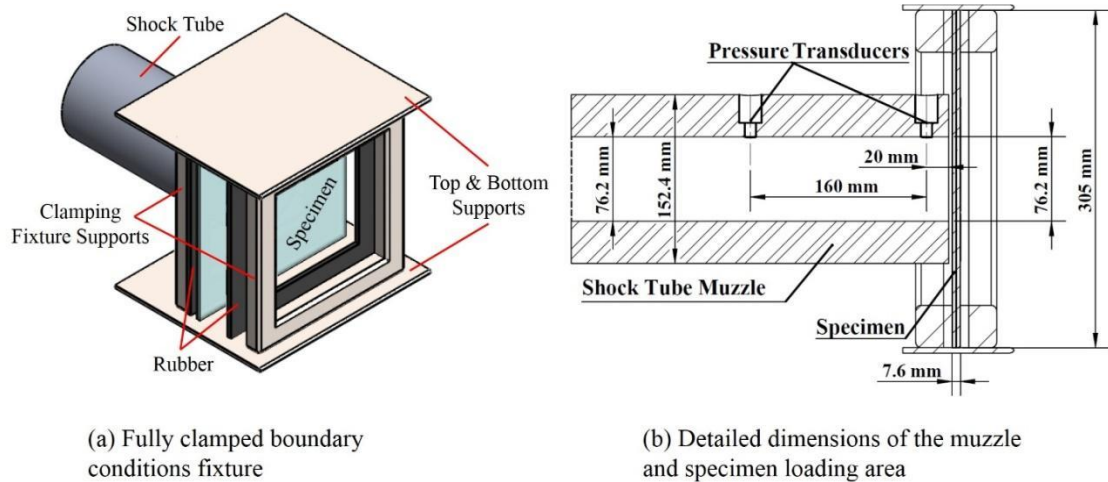
Fig. 3 Schematics of the muzzle of the shock tube and fixture

The pressure applied on the sandwich specimen was recorded by the sensor closest to the sandwich specimen. A digital oscilloscope (TDS3014C) was used to record the pressure history during each dynamic event at 1.0 MegaSamples/s. A diaphragm configuration of 2 stacked plies of Mylar sheets (total thickness of 0.356 mm) was used to generate the shock loading. The incident and reflected peak pressures were all the same at the different temperature environments. This observation agrees with previous work [26] which indicates that the reflected peak pressure for different materials only relies on the incident peak pressure. A typical pressure loading history is shown in Fig. 4a. The incoming shock waves had an average incident peak pressure of 0.6 MPa and reflected peak pressures of 2.5 MPa. According to the sensor's readings, the peak overpressure value of the incident pressure profile was six times the value of ambient air. The reflected pressure showed the loading value experienced at the front face of the specimen. The generated shock wave had a short rise time of about 80 μs and showed an exponential decay period of

23

approximately 2000 μs. The shock wave traveled out of the muzzle with an average velocity of 800 m/s and was reflected with an average velocity of 350 m/s. In this case, the blast shock had an approximate Mach number of 2.40. Figure 4b shows the typical impulse imparted to the specimen. This was obtained by integrating the force-time data of the reflected pressure history. The sandwich specimen at different temperatures obtained a maximum impulse of 18 Ns from the shock loading.

(a) Incident and reflected pressure profiles

(b) True duration of imparted impulse on specimen
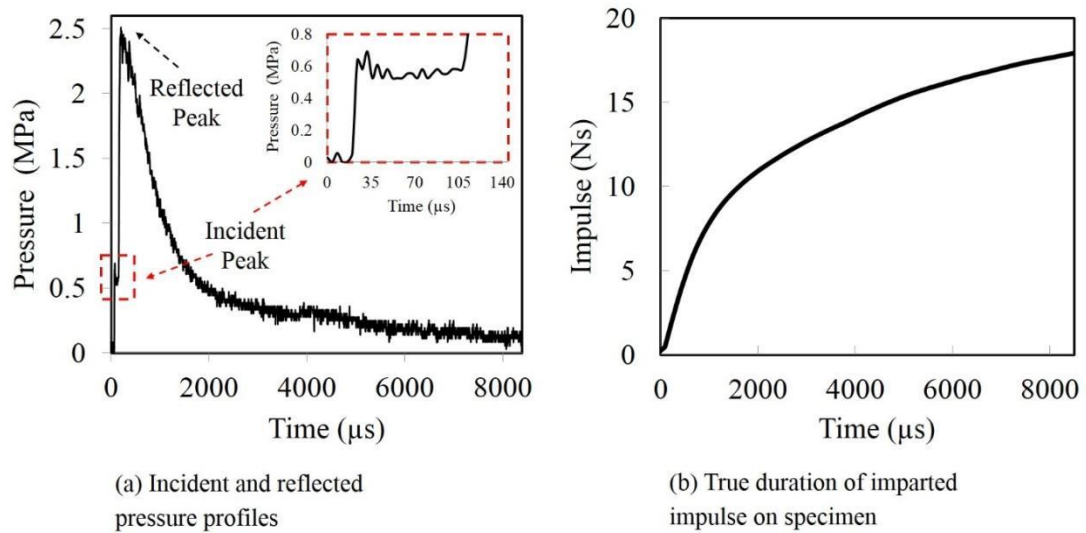
Fig. 4 Typical pressure pulses and the true impinging impulse on specimen

For testing the sandwich specimen under high temperatures, a heating element was used to heat the internal environment of a thermally insulated chamber (shown in Fig. 5a). By supplying different voltages (0-100 V) to the chamber, various steady-state temperature values were achieved. Lab-View software was used for recording and plotting the temperature-time calibration curves by using a thermocouple adaptor which converts the voltage signals measured to temperature. To perform high temperature experiments, the sandwich specimens were heated for approximately 200

minutes until the desired temperature was reached. The temperature inside the chamber was maintained at the designed level for at least 15 minutes before the blast experiment. A typical 80 °C calibrated temperature-time plot is shown in Fig. 5b. For low temperature testing, the sandwich specimen was cooled down in a freezer for about an hour up to a minimum temperature of (-20 °C). The sandwich specimens were sealed from the freezer's environment so no humidity was accumulated during the cooling process. Once desired temperature was achieved, the sandwich specimen was placed in the support fixture (inside the shock-tube facility) and tested after a certain calibrated waiting time. It is important to note that the sandwich specimen began to warm up after it is removed from the freezer and thus, a series of calibration tests were conducted to ascertain how long the specimen would take to reach the temperatures desired for testing (-10, 0 °C). In order to perform blast loading experiments at −10 and 0 °C, the sandwich specimen was held in room temperature for approximately 2 min. and 5 min., respectively as shown in Fig. 6.

(a) Experimental setup showing the thermally insulated heating enclosure

(b) Steady state heating calibration plot for 80 °C
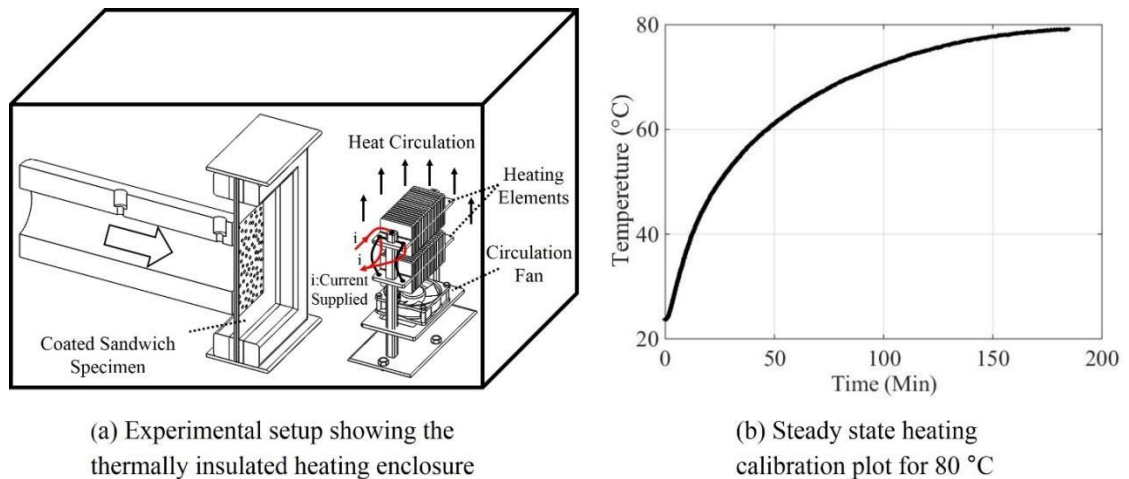
Fig. 5 Heating setup for shock loading experiments
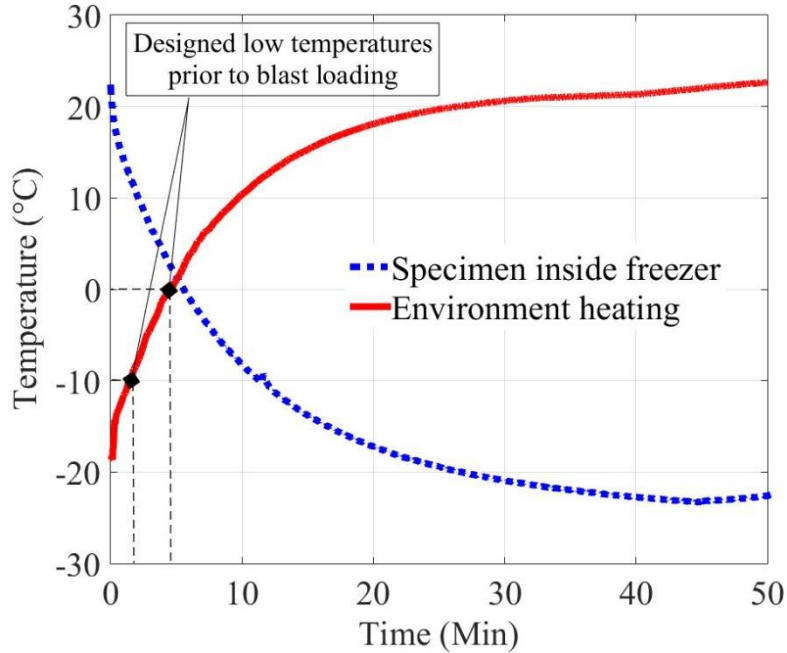
Fig. 6 Cooling calibration plot for -10 and 0 °C experiments

A high-speed photography system was used to record the loading event at 20,000 fps with an image resolution of 512×512 pixels for one second time duration. The inter frame time between the recorded images was 50 micro-seconds. This photography system consists of two [Photron SA1] high-speed digital cameras, which were located behind the sandwich specimen (the detailed experimental setup is shown in Fig. 7). The resolution of these cameras was selected to correspond with the exposed blast area (152.4 mm x 152.4 mm) of the sandwich specimen. Two high intensity light sources were used to illuminate the sandwich specimens due to the short exposure times during the experiments. The high-speed photography system first was calibrated to ensure accurate measured results throughout the blast loading event. This was done by using the calibration grid plate and procedures provided by Correlated Solutions. A non-contact 3-D Digital Image Correlation (DIC) technique used images

26

with a speckle pattern from the high speed cameras to obtain the full field deformation, velocities, and strains of each sandwich specimen during loading. Flat paint was used to create a random, high contrast speckle pattern on the surface of each sandwich specimen in order for the DIC technique to work. Figure 7 shows a real captured image of the speckle pattern. The DIC analysis was then performed using VIC-3D software from Correlated Solutions.
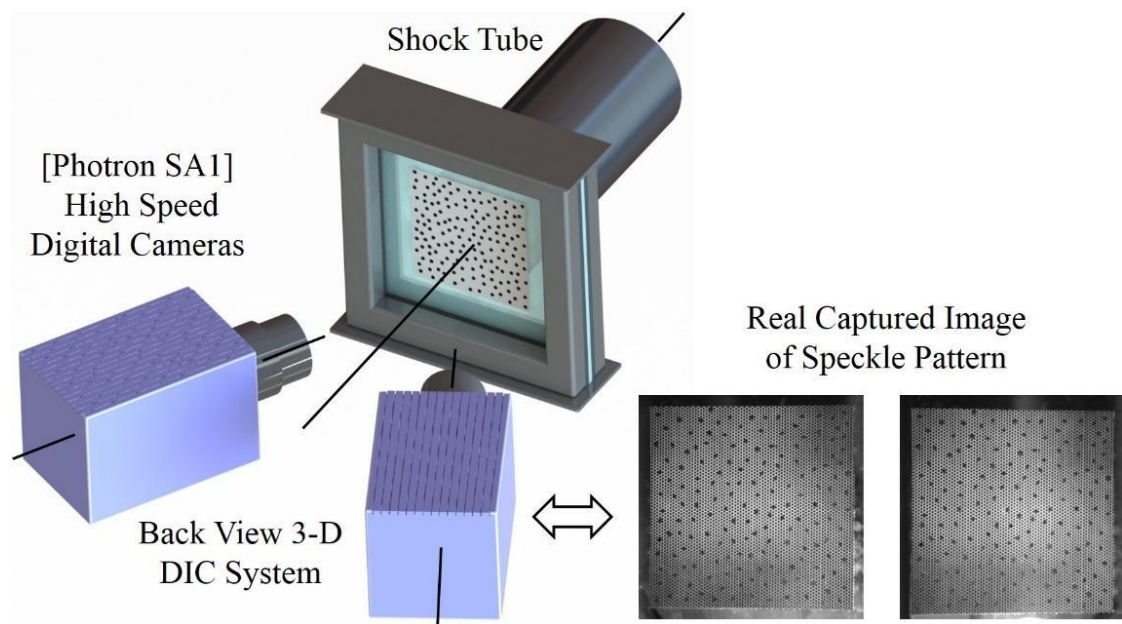
Fig. 7 Experimental highspeed photography setup showing the back-view 3D-DIC system

2.3 Tensile Testing of Coating Material under Different Temperatures

In order to characterize and correlate the response of the thermoplastic material used for coating the LSG panels, quasi-static tensile tests on XO ARMOR® protective films were performed at the same desired temperature environments as the shock loading experiments. To achieve the desired range of testing temperatures around the film specimens prior to and during testing, an environmental chamber (330 mm long ×

381 mm wide × 762 mm high) made of thermal insulation foam was designed and fitted to the tensile testing machine. A schematic of the experimental setup is shown in Fig. 8. For testing the protective film under high temperatures (50, 80, 110 °C), a heating element with variable DC power supply (0–60 V) was utilized to control the amount of heat generated. A circulation fan was used to ensure proper air-circulation. By controlling the voltage supplied to the chamber, different steady state high temperatures were achieved. Film specimens were heated as shown in Fig. 8a for approximately 40-50 minutes until the desired temperature was reached. For low temperature tensile testing, dry ice (CO_2) was placed in small containers to create a large surface area as well as achieve high sublimation rates inside the chamber. Different steady state low temperatures were achieved by controlling the amount of dry ice and air flow rate of circulation fan. Film specimens were cooled down as shown in Fig. 8c for approximately 12 and 20 min until the desired temperature was reached. In the present study, the temperature was measured (using a K-type thermocouple) directly on samples until their temperature stabilized at the desired level. Typical temperature-time plots for tensile specimens at high and low temperatures are shown in Fig. 8b, d respectively.
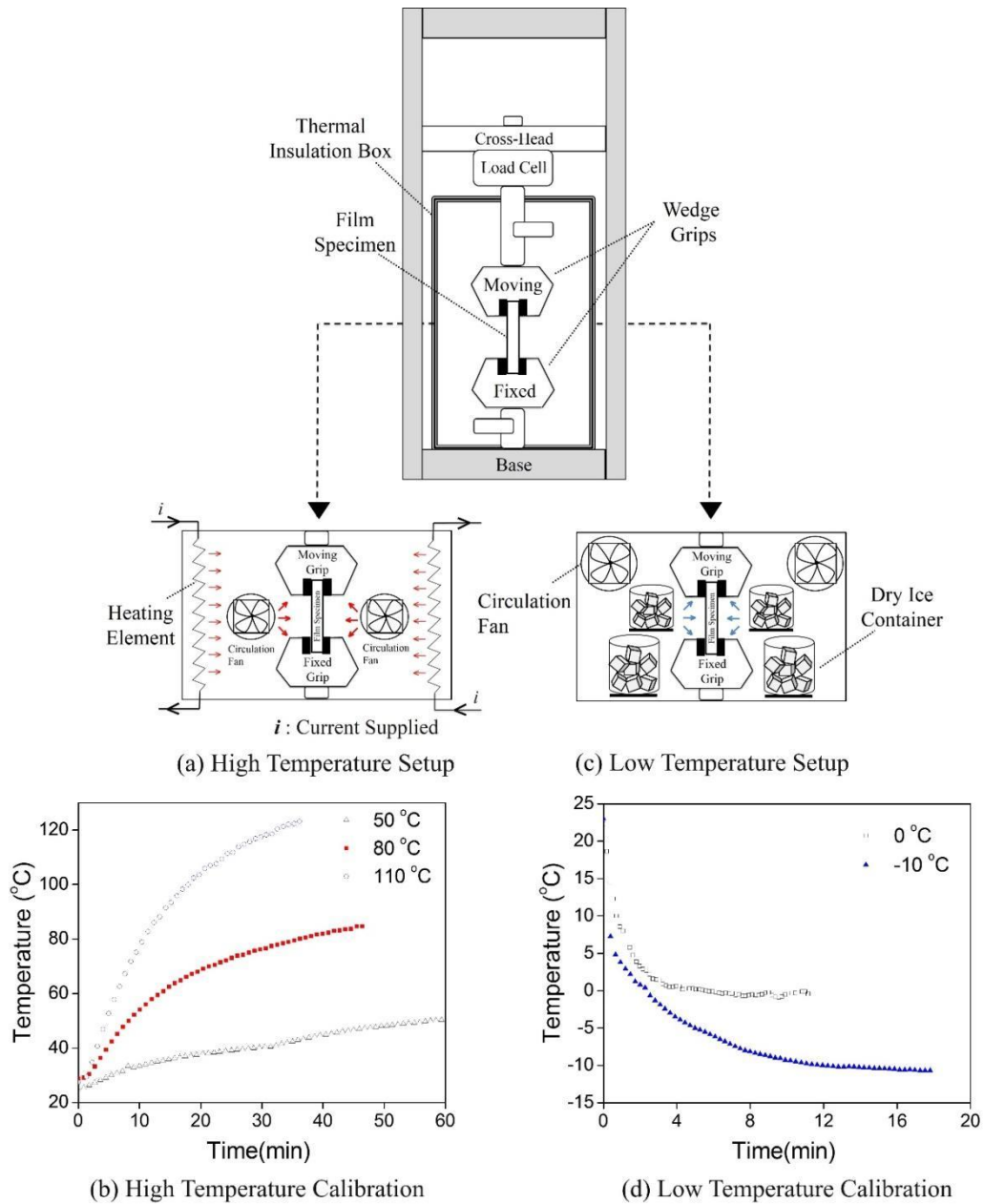
Fig. 8 Modified Instron machine setup for tensile experiments at high and low temperature environment

The film cutting procedures were followed by ASTM (D-6287) standard [27] using a dual blade shear cutter technique. The sample preparation and cutting direction have a direct influence on the test results "since it alters the material properties." In general, the molecular orientation in the transverse (perpendicular) cutting direction is

relatively weak and requires less energy to fracture as compared to the sheet rolling direction which is stronger. Therefore, in order to account for a worst-case scenario failure, tests were carried out for samples cut perpendicular to the sheet rolling direction. Uniform strips measuring 0.279 mm thick, 215.9 mm long, and with a nominal width of 20.0 mm were used. These strips were ensured to have straight, clean, parallel edges with no visible imperfections. The film materials underwent tensile testing in accordance with the ASTM (D-882) standard [28]. Prior to each test, film specimens with gage length of 107.7 mm were fitted between wedge grips of the Instron 3366 testing machine equipped with a 10 KN load cell and data acquisition software, then pulled until complete failure. The tensile tests were conducted with a loading speed of 50 mm/min in order to accomplish a constant sample deformation (strain) rate of 0.0083 (ε/s). For each temperature, a minimum of five repetitions were performed to verify consistency in the test results.

3. Experimental Results and Discussion

3.1 XO-ARMOR Response

The effect of temperature on the stress-strain curve for the film coating is shown in Fig. 9. This figure denotes that the XO-ARMOR materials showed both possibilities of ductile and brittle failure like most thermoplastic polymers. The temperature increase leads to a decrease in elastic modulus, reduction in tensile strength, and an increase in ductility. Conversely, brittle fracture was favored at lower temperatures.

30

At room temperature, the coating material showed a 95 MPa yield stress and a Young's modulus of 3.5 ± 0.01 GPa. As the temperature decreased to -10 °C, the coating film showed maximum yield stress of 128 MPa and exhibited maximum Young's modulus of 4.2 ± 0.01 GPa. Thermal softening occurs as the temperature is increased to 110 °C in which case the yield stress dropped to about 26 MPa and the elastic modulus achieved a minimum value of 1.3 ± 0.01 GPa. The yield strength at -10 °C was about 35% higher than that at a temperature of 25 °C, while it was lower by approximately 73% at 110 °C. The Young's modulus at a low temperature (-10 °C) was about 3.2 times higher than that at a high temperature (110 °C).
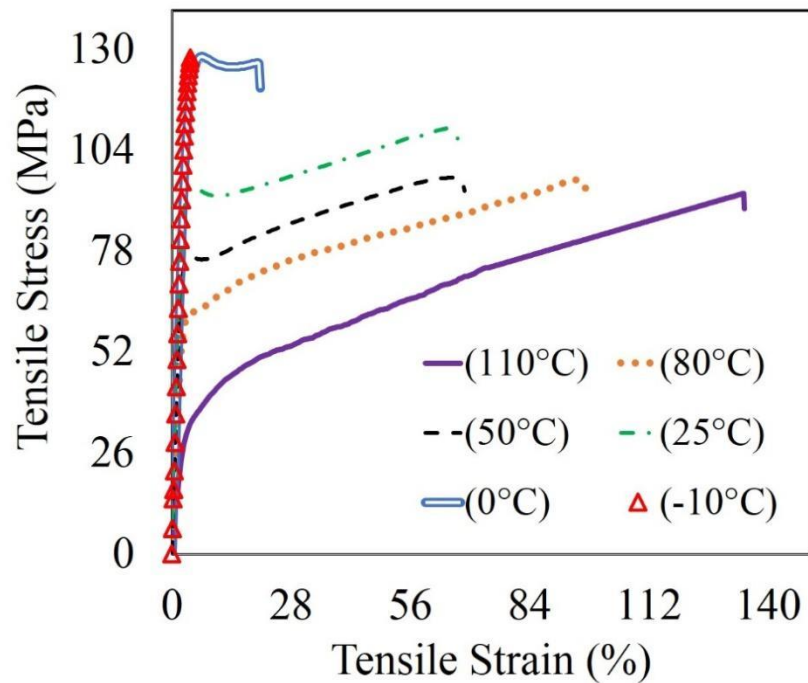
Fig. 9 Tensile stress–strain curves of XO ARMOR_ protective film under quasi-static loading at different temperatures

The qualitative nature of the failure strain at different temperatures is shown in Fig. 10. The elongation at break increased with increasing temperature from -10 to 110 °C. The coating material showed a failure strain of 53% at room temperature. A minimum failure strain of 5% was exhibited by the coating material at a temperature of -10 °C whereas the material showed a maximum failure strain of 135% at 110 °C. The average values of tensile energy to break (TEB) depending on the temperature are also shown by Fig. 10. The TEB is defined in the present study as the total energy absorbed per unit volume of the film specimen up to the point of rupture and is calculated by integrating the area under the stress-strain curves. The maximum TEB of 81.2 MJ/m^3 was observed for 110 °C. When the coating material had temperatures of -10, 0, 25, 50 and 80 °C, it showed maximum TEB of 3.1, 20.4, 50.5, 62.2, and 74.6 MJ/m^3, respectively. The magnitude of tensile energy to failure at 110 °C was 78 times higher than that at -10 °C. The mechanical behavior of XO-ARMOR materials signifies their excellent ability to absorb more energy under high temperatures. The glass transition temperature of the film coating is between −10 and 0 °C below, which it exhibits brittle failure. The trend changes in yield stress and elongation as a function of temperature observed were expected to be qualitatively similar even at higher strain-rates. Brown et al. [29] have shown that the trend changes in yield stress as a function of temperature and strain-rate in polymers can be expressed by linear and logarithmic fits respectively. Furmanski et al. [30] showed that the quasi-static data at depressed temperatures can be used to predict high strain rate response after correcting for adiabatic heating.
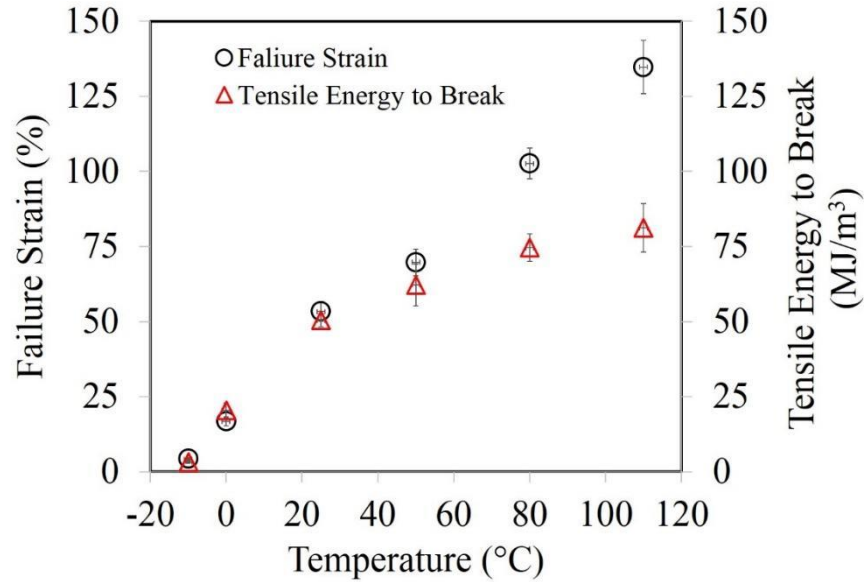
Fig. 10 Failure strain and energy absorption of the coating material as a function of temperature

3.2 Room Temperature Response

In the current work, the applied shock load was experienced by the sandwich specimen during fluid-structure-interaction (FSI) time, the early stage of blast loading. Figure 11 shows that the shock wave impinged on the sandwich specimen at t = 0 μs. Circular deflection contours on the back face began to appear at t = 50 μs showing that the stress wave had propagated through the front face of the sandwich specimen. After that, these deflection contours evolved with time. During the (FSI) time, the boundary conditions had no influence on the structural dynamic response of the sandwich specimen. In which, there were not any glass fractures (cracks) observed in any of the glass plies of the sandwich specimen for the first 200 μs of the blast event and a relatively minimal out-of-plane deflection of approximately 1.9 mm with in-plane strain of 0.4%, as shown in Fig. 11a, b respectively. After the (FSI) time, the whole sandwich specimen started experiencing significant outward deflection and the

deformation from here on was affected by the boundary conditions and the dynamic material properties of both the interlayer and film coating.
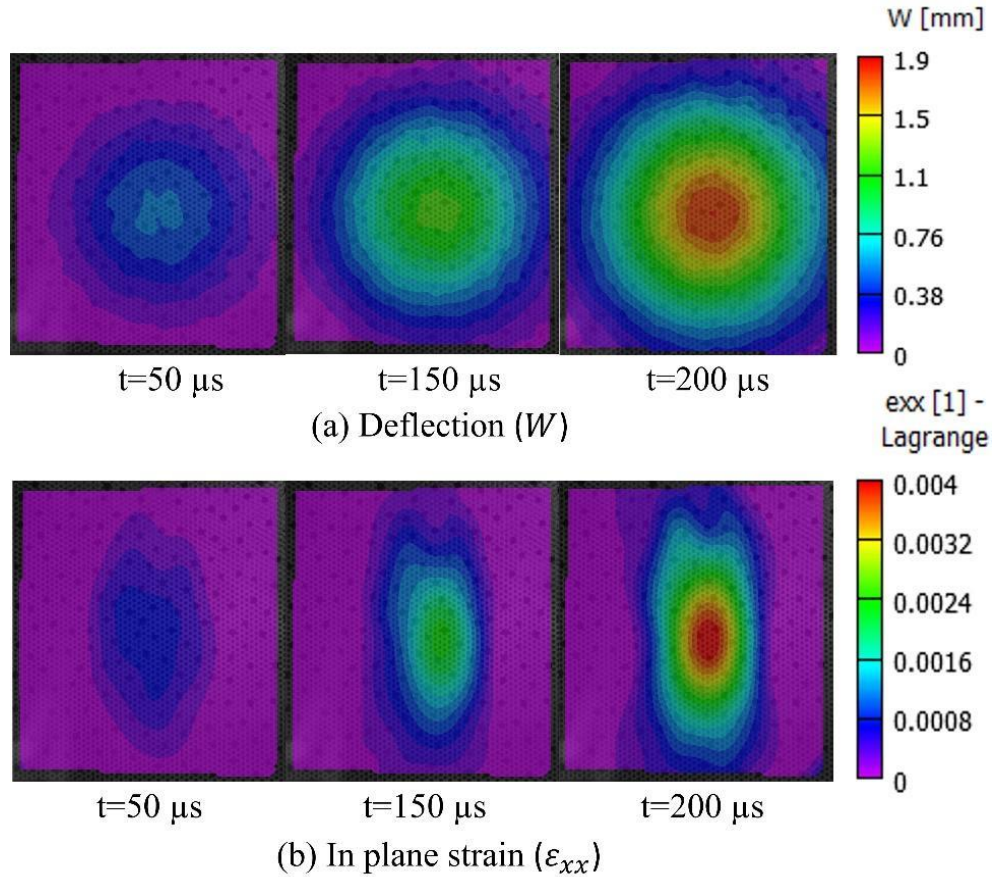
Fig. 11 Back-face (a) deflection and (b) strain contours of sandwich specimen during fluid–structure interaction time for room temperature experiment

As a result of the damage (cracks) that began close to the boundaries, the sandwich specimen at room temperature underwent internal damage (glass plies started to break) at t = 250 μs as shown by the real time images (Fig. 12). The shear force at the boundary causes the glass to crack, similar to observations reported by Zhang et al. [16]. At t = 300 μs, circular crack patterns formed from the central area of the blast loading. After glass had fragmented, only the PVB and the coating materials resisted the blast loading and, thus the structural stiffness reduces. The glass plies

continued to break into smaller fragments up to the point of maximum deflection at t = 2000 μs. This fragmentation process of glass up to the point of peak deformation is a unique energy dissipation mechanism offered by this particular construction of sandwich panel.

The deformation mechanisms of the sandwich specimen under blast loading are described as follows. The panel started with elastic behavior until the first glass ply was broken, while the other layer of glass was still intact, and the PVB interlayer along with the film coating were both undamaged. After the second glass ply failed, both the interlayer and film coating materials behaved elastically. Then as the entire panel remained under loading, both the interlayer and film coating were behaved plastically. The glass fragmentations were kept together by film coating and the PVB materials for further deformations until failure occurred. Both the interlayer and film coating failed by reaching their failure strain or by cutting from the splinters. Larcher et al. [11] reported similar failure of laminated glass sheets where the PVB interlayer alone was resisting the air blast waves while keeping the splinters together.

t=250 μs	t=300 μs	t=700 μs	t=2000 μs
Crack initiation at the boundaries	Circular crack pattern initiating from center	Continuation of glass breaking to boundaries	Small glass fragmentations at point of maximum deflection
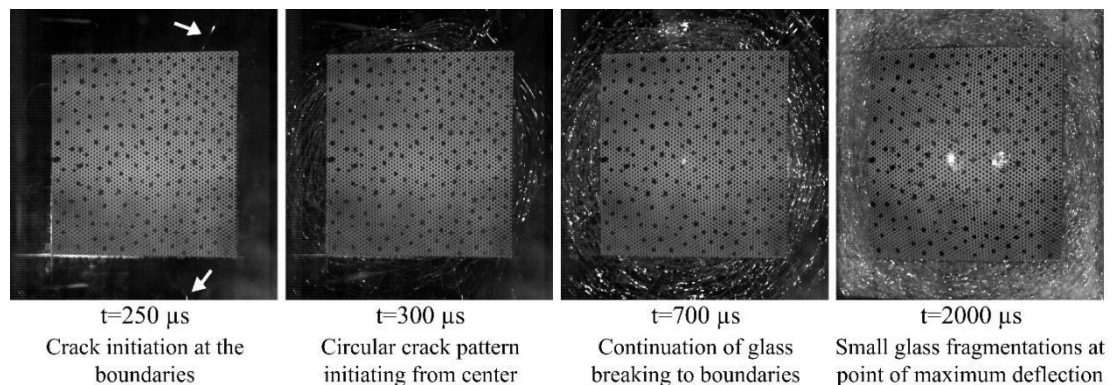
Fig. 12 Real time images of glass breaking plies of the sandwich specimen at 25 °C

For better understanding of the film coating effects on blast mitigation properties of LSG panels close to room temperature, full field out-of-plane deflection and in-plane strain history over an extended time (t = 4000 μs) were investigated as shown in Fig. 13. At t = 700 μs, the sandwich specimen deflected 15.5 mm with 6 % strain. At (t = 2000 μs), the specimen reached its maximum deflection of 35.3 mm with 12.8% strain and then began to rebound. At t = 4000 μs, the sandwich specimen settled to a final out-of-plane deflection of 24.7 mm and in-plane strain of 8.4%. The deflection and strain were concentric about the mid-point and that the central portion of the film coating is subjected to large tensile strains. The protective film was able to keep the shattered glass pieces from flying away and controlled the damage propagation.
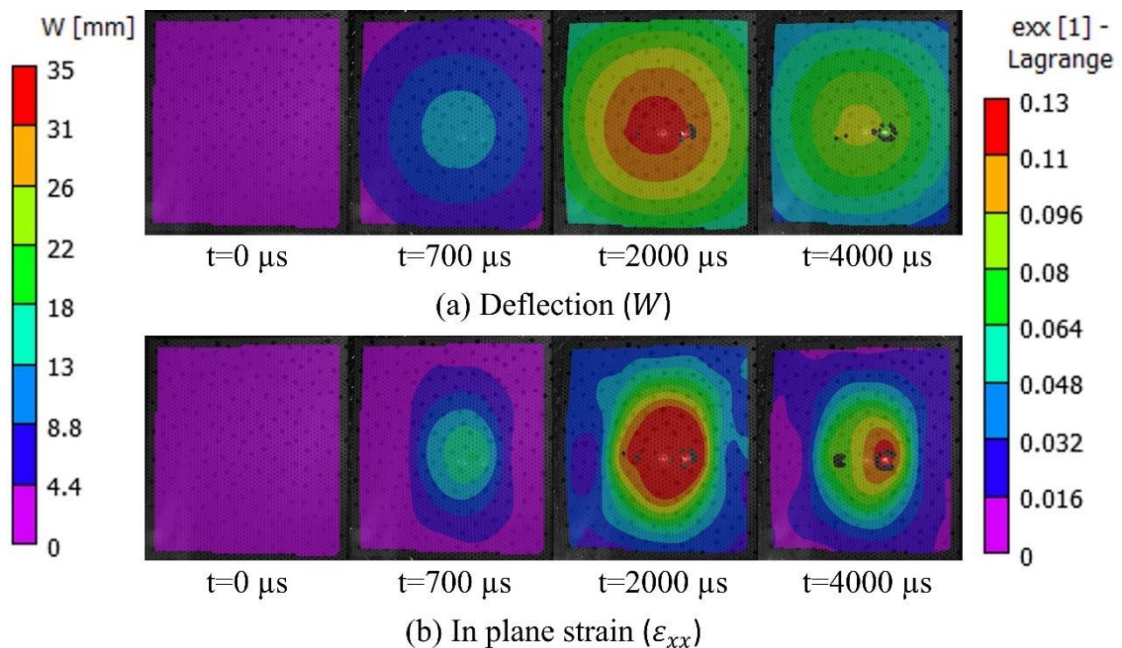
Fig. 13 Typical full field DIC results of the sandwich specimen back face from a blast experiment at 25 °C for both (a) out-of-plane deflection with a scale of 0 mm (purple) to 35 mm (red) and (b) in-plane strain with a scale of 0 (purple) to 0.13 (red)

3.3 Effect of Temperature on Sandwich Specimen Response

The temperature effect on stress wave propagation through the sandwich specimen during FSI time (up to t = 200 μs) was investigated in the present study. The stress wave propagates with lower wave speeds at higher temperature environments as compared to room and low temperature environments as shown by Fig. 14a-c respectively. In the latter cases, the stress waves took longer to propagate and stabilize. A similar phenomenon of FSI time for marine foam core sandwich composites was reported in previous studies by Gupta and Shukla [31].
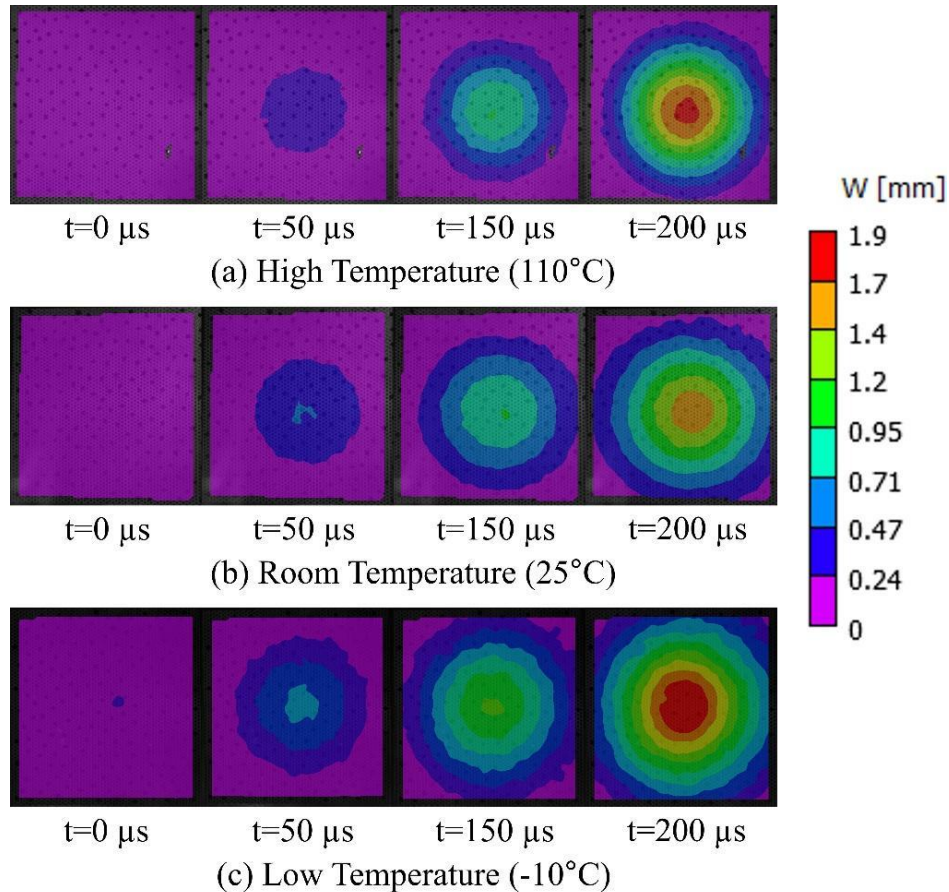
Fig. 14 Circular deflection contours with a scale of 0 mm (purple) to 1.9 mm (red) of the specimen back face during FSI time

The data at the center point of the back face for each experiment was evaluated and plotted using the point-inspection tool from the digital image correlation software. The temperature effect on the mean back-face deflection history is shown in Fig. 15. As discussed earlier in Fig. 13a, the room temperature specimen showed a maximum deflection of 35.3 mm at t = 2000 μs and then began to rebound. For the 0 °C experiment, the composite structure showed a maximum back-face deflection of 29.7 mm at t = 1800 μs and began to rebound. As the temperature decreased to -10 °C, the sandwich panel reached deflection of 14.2 mm and then began to fail at t = 700 μs. The expectation was that the specimen at lower temperatures responded quicker due to its higher stiffness and began to rebound ahead of time, 200 μs (for 0 °C case), as compared to room temperature. At t = 4000 μs, the sandwich specimen at 0 °C experiment settled with 12% less out-of-plane deflection as compared to the 25 °C experiment.

Under the same air blast load, the panel at higher temperatures deformed faster and with larger maximum deflections, due to the flexible material. The PVB interlayer and coating materials had significant contribution to the ductility of the composite structure. In comparison to the room temperature experiment, the sandwich specimen at 50 °C and 80 °C deformed for additional 600 μs and 1000 μs respectively, before reaching maximum deflection. For high temperatures of 50 °C and 80 °C, the sandwich specimens deflected in a similar manner prior to reaching their maximum deflection of 50.7 mm and 61.0 mm at t = 2600 μs and 3000 μs respectively and then began to rebound. However, as the temperature increased to 110 °C, the specimen reached deflection of 42.3 mm and began to fail at t = 1000 μs. At t = 4000 μs,

experiments of 50 °C and 80 °C respectively, showed 69% and 135% more out-of-plane deflection on the back face of the sandwich specimen as compared to the 25 °C experiment.
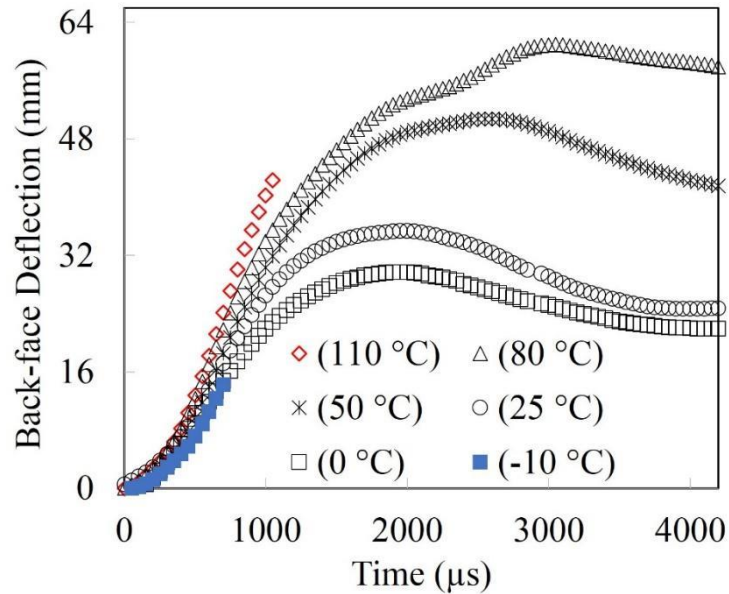
Fig. 15 Mean center-point back-face deflections histories of specimens at different environment temperatures using DIC analysis

Figure 16 shows the out-of-plane particle velocity (dW/dt) on the back face of the sandwich panel at different temperatures. A steep increase in velocity was seen at around t = 300 μs. This time corresponded to the occurrence of glass fragmentation which reduced the stiffness and caused the outward acceleration of the composite. For 0 to 80 °C, the sandwich specimens reached their maximum velocities between t = 700 and 800 μs. The room temperature specimen had a maximum velocity of 36.0 m/s at t = 750 μs and it started to decelerate after that. The velocity continued to be reduced to approximately 0 m/s as the specimen reached its maximum deflection (at t = 2000 μs) and began to rebound. When the specimen temperature dropped to 0 °C, the maximum

velocity was 27.4 m/s, and this lower velocity can be attributed to higher stiffness of coating and PVB materials. Prior to failure at -10 °C, the sandwich specimen had a velocity of 26.5 m/s. Under high temperature experiments at 50 °C and 80 °C, the sandwich specimen reached higher peak velocities of 45.5 and 48.2 m/s respectively due to decreasing coating stiffness. At 110 °C, the sandwich specimen reached peak velocity of 60.0 m/s and the film coating was intact. The film coating was able to decelerate the center of the back face velocity from 60.0 to 45.4 m/s as shown in Fig. 16. In this deceleration process, the coating material was stretched (strained) further and it ruptured. Even though the coating material failed, the load bearing capacity of the film and its contribution in reducing the speed of the glass fragments are notable.
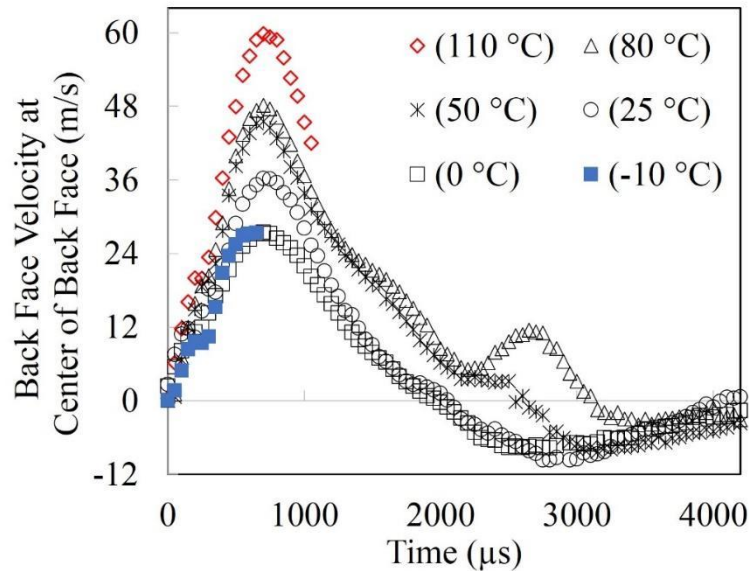
Fig. 16 Back face out-of-plane velocity profiles of specimen at different environment temperatures calculated from DIC

The full-field of in-plane strains (ε_{xx}) on the back-face of the sandwich specimen at maximum deflection or at failure for temperatures ranging from -10 to 110 °C are shown in Fig. 17. For -10 °C (Fig. 17a), the sandwich specimen was

reached 6% in-plane strain and then failed. This is in-line with the results of tensile experiments on the coated film which showed brittle failure at -10 °C when strained to 5%. Figure 17 shows that the in-plane strain of the sandwich specimen increased with increasing temperature. The composite panel showed great endurance during the blast loading for temperatures ranging from 0 to 80 °C (Fig. 17b-e). In-plane strains of 9, 12.8, 16, and 19.3% were experienced by the coating at temperatures of 0, 25, 50, and 80 °C respectively. At 110 °C (Fig. 17f), the panel showed 23% in-plane strain at the time of failure. This strain is much lower than the failure strain observed in the 110 °C tensile experiment on coating film. Thus it can be inferred that this failure in the coating material was due to the tearing of the film by the glass fragments, which is due to the failure of PVB section at higher temperatures.
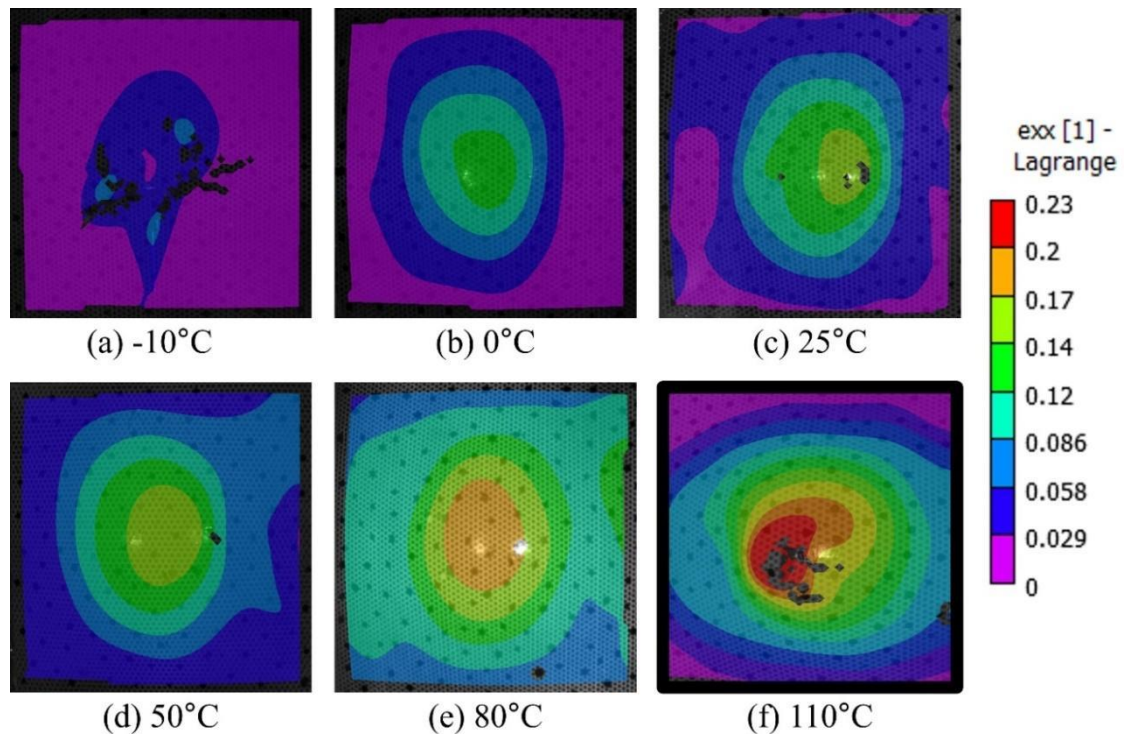
Fig. 17 Full field in-plane strain (e_{xx}) at maximum deflection or at failure of sandwich specimen at different environment temperatures

The real time images captured during the experiment were studied to further investigate the failure process at 110 °C and -10 °C. From the images (Fig. 18a) we can observe that many small glass fragments were flying out of the sandwich specimen, showing that the PVB interlayer was not able to contain them (PVB material loses strength at high temperatures). The de-bonding of glass fragments from PVB interlayer might have facilitated the rupture of the coating film by the glass fragments. However, as seen in (Fig. 18b) the PVB interlayer at −10 °C was able to hold a substantial amount of the small glass fragments together even after catastrophic failure of the coating material. Figure 19 shows how these glass fragments were contained by the PVB interlayer. This signifies the critical role of PVB interlayer in the performance of the sandwiched structure.

(a) High Temperature (110 °C)

(b) Low Temperature (-10 °C)
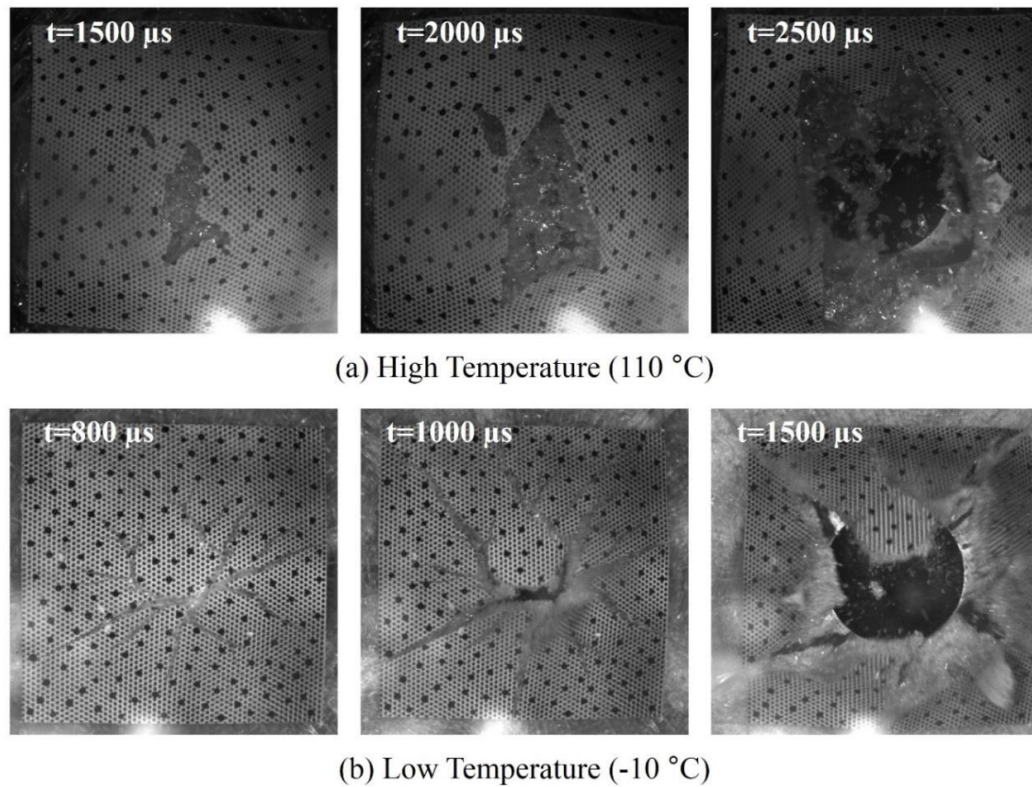
Fig. 18 Real time images of sandwich specimen showing the failure process at low (-10 °C) and high (110 °C) temperature
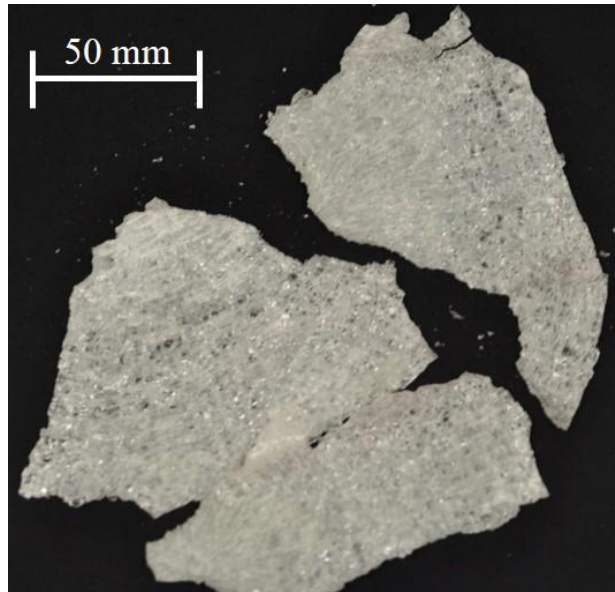
Fig. 19 PVB interlayer at -10 °C holding glass fragments

4. Conclusions

This study focused on the dynamic response of laminated glass composite, which is coated with XO-Film, under combined shock loading and extreme temperatures. The major findings of this study are as follows:

- There was substantial glass fragmentation at all temperatures. However, the coating material and PVB interlayer enabled structural integrity, controlled the damage propagation, and prevented glass pieces from flying away at temperatures ranging from ~0 to ~80 °C. In which case both interlayer and coating materials survived the shock loading with no catastrophic failure.

- PVB interlayer at −10 °C was able to hold a substantial amount of the small glass fragments together even after catastrophic failure of the coating material.

- The failure at 110 °C is likely due tearing of the coating by the glass fragments.

- Due to the temperature-dependent material properties of the protective film coating and PVB interlayer, the sandwich specimen showed an increasing trend in back-face deflection and in-plane strain with increasing temperature.

- The fragmentation process of glass continues to the point of peak deformation. This is a unique energy dissipation mechanism offered by this construction of sandwich panel.

- For good performance of this type of sandwich structure geometry, both the interlayer and the coating film should have good ductility and strength at the target temperatures.

References

1. H. Scott Norville, GRTL (1987) Misty picture data: window glass experiment, final data report, Glass Research and Testing Laboratory, Texas Tech University, Lubbock, TX

2. Norville HS, Harvill N, Conrath EJ, et al. (1999) Glass-Related Injuries in Oklahoma City Bombing. Journal of Performance of Constructed Facilities 13:50–56

3. Smith D (Tampere, Finland, 2001) Glazing for injury alleviation under blast loading, United Kingdom practice. In Glass Processing Days Conference Proceedings, 335–340

4. Stephens RAC (2008) Determination of the resistance of laminated glass subjected to blast loading using high speed video [M.Sc. thesis]. Cranfield University.

5. Puneet Kumar, Arun Shukla (2011) Dynamic response of glass panels subjected to shock loading. Journal of Non-crystalline Solids - J NON-CRYST SOLIDS 357:3917–3923

6. Shetty MS, Wei J, Dharani LR, Stutts DS (2013) Analysis of Damage in Laminated Architectural Glazing Subjected to Wind Loading and Windborne Debris Impact. Buildings 3:422–441

7. Zhang X, Hao H, Wang Z (2015) Experimental study of laminated glass window responses under impulsive and blast loading. International Journal of Impact Engineering 78:1–19

8. UFC 4-010-01 (2003) Minimum Antiterrorism Standards for Buildings, Unified Facilities Criteria, Department of Defense, Washington D.C., USA

9. ASTM F2248 (2009) Standard Practice for Specifying an Equivalent 3-second Duration Design Loading for Blast Resistant Glazing Fabricated with Laminated Glass, West Conshohocken, PA, USA

10. Wei J, Shetty MS, Dharani LR (2006) Failure analysis of architectural glazing subjected to blast loading. Engineering Failure Analysis 13:1029–1043

11. Larcher M, Solomos G, Casadei F, Gebbeken N (2012) Experimental and numerical investigations of laminated glass subjected to blast loading. International Journal of Impact Engineering 39:42–50

12. P. Hooper, H. Arora, J.P. Dear (October 12–14 2010) Blast and impact resistance of laminated glass structures, Proceedings of the IMPLAST 2010 conference, Providence, RI, USA

13. Hooper PA, Sukhram RAM, Blackman BRK, Dear JP (2012) On the blast resistance of laminated glass. International Journal of Solids and Structures 49:899–918

14. Wei J, Dharani LR (2006) Response of laminated architectural glazing subjected to blast loading. International Journal of Impact Engineering 32:2032–2047

15. Zhang X, Hao H (2015) Experimental and numerical study of boundary and anchorage effect on laminated glass windows under blast loading. Engineering Structures 90:96–116

16. Zhang X, Hao H, Ma G (2013) Parametric study of laminated glass window response to blast loads. Engineering Structures 56:1707–1717

17. Hidallana-Gamage HD, Thambiratnam DP, Perera NJ (2014) Numerical modelling and analysis of the blast performance of laminated glass panels and the influence of material parameters. Engineering Failure Analysis 45:65–84

18. Peroni M, Solomos G, Pizzinato V, Larcher M (2011) Experimental Investigation of High Strain-Rate Behaviour of Glass. Applied Mechanics and Materials 82:63–68

19. Zhang X, Zou Y, Hao H, et al. (2012) Laboratory test on dynamic material properties of annealed float glass. International Journal of Protective Structures 3:407–430.

20. Hooper PA, Blackman BRK, Dear JP (2011) The mechanical behaviour of poly (vinyl butyral) at different strain magnitudes and strain rates. J Mater Sci 47:3564–3576

21. Zhang X, Hao H, Shi Y, Cui J (2015) The mechanical properties of Polyvinyl Butyral (PVB) at high strain rates. Construction and Building Materials 93:404–415

22. Wang E, Gardner N, Shukla A (2009) The blast resistance of sandwich composites with stepwise graded cores. International Journal of Solids and Structures 46:3492–3502

23. Gardner N, Wang E, Kumar P, Shukla A (2011) Blast Mitigation in a Sandwich Composite Using Graded Core and Polyurea Interlayer. Exp Mech 52:119–133

24. Courant R, Friedrichs KO (1948) Supersonic Flow and Shock Waves. Interscience Publishers, New York

25. Wang E, Shukla A (2010) Analytical and experimental evaluation of energies during shock wave loading. International Journal of Impact Engineering 37:1188–1196

26. Wang E, Wright J, Shukla A (2011) Analytical and experimental study on the fluid structure interaction during air blast loading. Journal of Applied Physics 110:114901–114912

27. ASTM D6287 (2009), Standard Practice for Cutting Film and Sheeting Test Specimens, ASTM International, West Conshohocken, PA

28. ASTM D882 (2012), Standard Test Method for Tensile Properties of Thin Plastic Sheeting, ASTM International, West Conshohocken, PA

29. Brown EN, Willms RB, Iii GTG, et al. (2007) Influence of Molecular Conformation on the Constitutive Response of Polyethylene: A Comparison of HDPE, UHMWPE, and PEX. Experimental Mechanics 47:381–393

30. Furmanski J, Cady CM, Brown EN (2013) Time–temperature equivalence and adiabatic heating at large strains in high density polyethylene and ultrahigh molecular weight polyethylene. Polymer 54:381–390

31. Gupta S, Shukla A (2012) Blast performance of marine foam core sandwich composites at extreme temperatures. Exp Mech 52(9):1521–1534

CHAPTER 3: NOVEL IMPACT MITIGATION TECHNIQUE USING SHOCK LOADING

by

Emad A. Makki, Murat Yazici, Idris Karen and Arun Shukla

under preparation for submission to the Journal of Experimental Techniques

Corresponding Author: Emad A. Makki

Dynamic Photo Mechanics Laboratory

Department of Mechanical, Industrial and Systems

Engineering

University of Rhode Island

94 Upper College Road

131 Kirk Applied Engineering Laboratory

Kingston, RI, 02881, USA

Phone: +1-401-874-2283

Email Address: emakki@my.uri.edu

Abstract

This study presents the design and experimental testing of a device intended to mitigate the peak impact load, velocity, impulse, and total impact energy of an impactor using shock loading. The device consists of a cylindrical composite bladder sealed on one end by an inflation valve and on the other by an aluminum sheet of variable thickness. The bladder is pressurized and as an impactor nears the device, it strikes a striker-needle, which ruptures the aluminum sheet, thus producing a shockwave just prior to impact. This produced shock wave decelerates the impactor and creates momentum (impulse) opposing that impulse transmitted from the impactor. Drop weight experiments were performed to show the applicability of this anti-shock device in reducing the momentum of the incoming body. A range of variables including needle length, bladder pressure, impact velocity, and drop mass were tested to better understand the processes involved. Time lapse photography coupled with 2D Digital Image Correlation (DIC) was used to obtain the striker full field motion data during the drop-weight experiments. It was found that the device effectively mitigates impact for higher impact velocities and for higher bladder pressures, decreasing peak loads during impact by up to 58% and energy imparted on the structure by 40%.

Keywords: Anti-shock device • Dynamic impact loading • Energy mitigation • High speed photography • Digital image correlation

1. Introduction

Every year in the United States, the physical trauma caused by impacts between pedestrians and high velocity bodies such as trains and cars has led to the

deaths of a large number of civilians [1]. It was reported by Lee et al, A. Mallory et al, Y. Matsui et al, and T. Niebuhr et al that the legs and head are the most frequently injured body regions in fatal pedestrian accidents in various countries [2-5]. According to Lv et al, lower extremity injuries from bumper contact occurred in 43% of injured pedestrian cases in the US, 35% in Germany and 43% in Japan [6]. Thus, a wide variety of active and passive vehicular technologies have been proposed to protect pedestrians in the event of impact with an automobile. Active safety technologies, such as vision-based technologies [7] or communication-based technologies [8], provide alerts that are intended to assist drivers in avoiding or mitigating a crash. Such systems can reduce the injury and fatal accidents by 36% and 59% respectively [9]. Passive safety systems that are installed in a vehicle, such as the pedestrian airbag system and the active hood lift system, protect a pedestrian's head during contact with a vehicle [10, 11]. Choi et al developed a methodology for estimating the safety benefits of integrated pedestrian protection system based on simulations and showed it is capable of reducing pedestrian fatalities by approximately 90% [12].

It is, therefore, the purpose of the work detailed in this chapter to investigate a new method of impact mitigation, the results of which may not only be applied to some future form of civilian protection similar to those mentioned above, but provide insight into the physical phenomena present in the mitigation of impact using opposing shock waves. This paper presents a novel device designed to release a shock wave just moments before an impactor collides with it, and details the experiments conducted in order to understand the device's impact mitigation performance. The device consists of a cylindrical composite bladder sealed on one end by an inflation

valve and on the other by an aluminum sheet of variable thickness. The bladder is pressurized and as an impactor nears the device, it strikes a striker-needle which ruptures the aluminum sheet, thus producing a shockwave just prior to impact. This produced shockwave decelerates the impactor and creates momentum (impulse) opposing that transmitted from the impactor. To test the effectiveness of the device, dynamic loading is replicated using an Instron 9210 drop-weight impact tower, with various drop tests using a range of weights and impact velocities were conducted. Other variables tested were the length of the striker-needle, that is, response time, and bladder pressure. Impact velocity was easily determined for all tests using the Instron´s data acquisition software, and time lapse photography coupled with 2D Digital Image Correlation (DIC) was used to obtain the striker's full field motion data during the drop-weight experiments. The DIC technique is a recent noncontact optical method for analyzing full-field shape, motion and deformation [13]. This technique uses images with a speckle pattern from the high speed camera. The Photron Fastcam Viewer (PFV) software was employed to synchronize the camera and record the images during the experiments. A speckle pattern was placed directly on the striker surface in order for the DIC technique to work. The DIC analysis was then performed using VIC-2D software from Correlated Solutions.

Through experimentation and subsequent analysis, it was determined that the device is indeed effective at mitigating impact. It was found that as the striker-needle length increased, impactor impulse decreased, for example, as the needle length was increased from 6 mm to 18 mm; impactor impulse was reduced by 37%. It was also found that the anti-shock device caused a greater load reduction for higher impact

velocities. Furthermore, the device is more effective when the bladder pressure is increased. Finally, the device was able to decrease peak load by 58%, and energy imparted to the structure by 40%.

2. Experimental Setup and Procedures

A series of low impact velocity experiments were conducted using a drop weight testing machine to understand the influence of the produced shock load on mitigating the impact loading of the striker.

2.1 Anti-Shock Production Set-up

The proposed system design consists of a special cylindrical thin-walled rubber tube that has a 76.2 mm outer diameter (OD) and 254 mm length as shown in Fig 1. The rubber tube composite material used in the present study was provided by PEGA Air Springs Company. The system device preparation and the main parts are shown in Fig. 1. On the top side of the device (see Fig. 1a), aluminum foil sheets were sandwiched between two hollowed flanges. The hollow disks are 15 mm thick and had outer and inner diameters of 137 mm and 59 mm respectively. Two concentric O-rings of different radii were used to avoid any leakage of compressed air during and after the filling process. An air valve was mounted on the bottom side of the device as shown in Fig. 1c.

This device can sustain different levels of initial pressures and pressure calibrations were performed with different number of foil sheets to obtain the critical bursting pressures. The estimated amount of potential energy stored in the anti-shock device (P.E) was controlled by considering the starting volume of the cylindrical thin-walled rubber tube and the magnitude of the internal pressure (P_o).

$$(P.E)_{device} = (\pi r^2 L) * P_O \tag{1}$$

where, r is the radius of the circular end of the cylinder and L is the length of the cylinder. The calibrated pressure values and the potential energy stored in the device are listed in Table 1.

The striker-needle design shown in Fig. 2 was applied to penetrate the aluminum foils as the impactor nears the pressurized device, thus initiating the opposing shock, which resists the impact load. The needle was designed to have an adjustable length of penetration and the impactor had a flat surface with circular cross section of 76.2 mm diameter.

Aluminum foil sheets

Rubber tube

(a) Proposed device

(b) System's top side

(c) System's bottom side
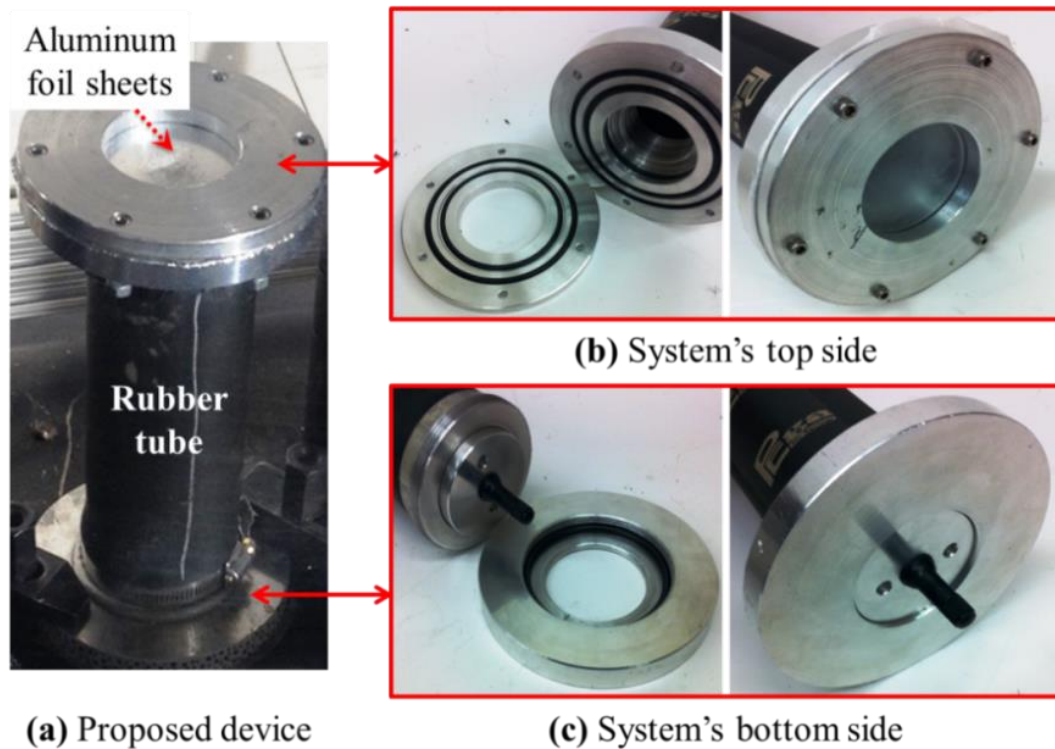
Fig. 1: Anti-shock pressurized system device and details of preparation

Table 1: Internal pressure calibration and the stored potential energy of the device

Number of Aluminum foil sheets	Critical bursting pressure (KPa)	Desired pressure (KPa)	Device potential energy (J)
3	172±7	170	197
4	241±7	240	278
6	347±7	345	400
8	519±6	517	600
10	692±8	690	800

2.2 Experimental Approach

The first series of drop weight experiments was conducted to understand the influence of the needle penetration length on the anti-shock wave production. In these experiments, the impactor was given the same initial height and the bladder's pressure was held constant. After the determination of the onset of the shock release of the device, the second set of experiments was performed to investigate the effectiveness of this device in mitigating different impact energies. In all these experiments, the internal pressure in the anti-shock device was kept constant. Lastly, the third set of experiments was loaded with the same impact energies, but the bladder's pressure differed in order to produce different levels of anti-shock. The experimental details are listed in Table 2.

Table 2: Details of series of experiments

Series of experiments		Device potential energy (P.E) [J]	Needle length (ℓ) [mm]	Drop mass (m) [Kg]	Drop height (h) [m]
	a_1	400	6	8.58	0.3
I	b_1	400	12	8.58	0.3
	c_1	400	18	8.58	0.3
	a_2	400	18	8.58	0.3
II	b_2	400	18	8.58	0.2
	c_2	400	18	8.58	0.1
	a_3	400	18	7.1	0.08
III	b_3	600	18	7.1	0.08
	c_3	800	18	7.1	0.08

2.3 Drop Weight Impact Experiments

The dynamic loading was implemented by a drop weight impact tower apparatus (Instron 9210), as shown in Fig. 2. The Dynatup 9210 used is outfitted with a low weight crosshead and is capable of producing 2.6-180 Joules of energy. The maximum impact velocity that can be achieved is 5 m/s. The drop tower is equipped with a data acquisition system that includes a velocity detector, a piezoelectric tup for measuring loads, a signal conditioning amplifier, and a computer with an A/D board. The velocity detector is capable of measuring impact velocity as well as rebound velocity. The recorded data histories of the impactor were processed using impulse data acquisition software. Time lapse photography coupled with 2D Digital Image Correlation (DIC) was used as a validation technique to obtain the striker full field motion data during the drop-weight experiments. The camera was set to record the loading event at 20,000 fps, (inter-frame time of about 50 μs), with an image resolution of 512 x 192 pixels for one second time duration.
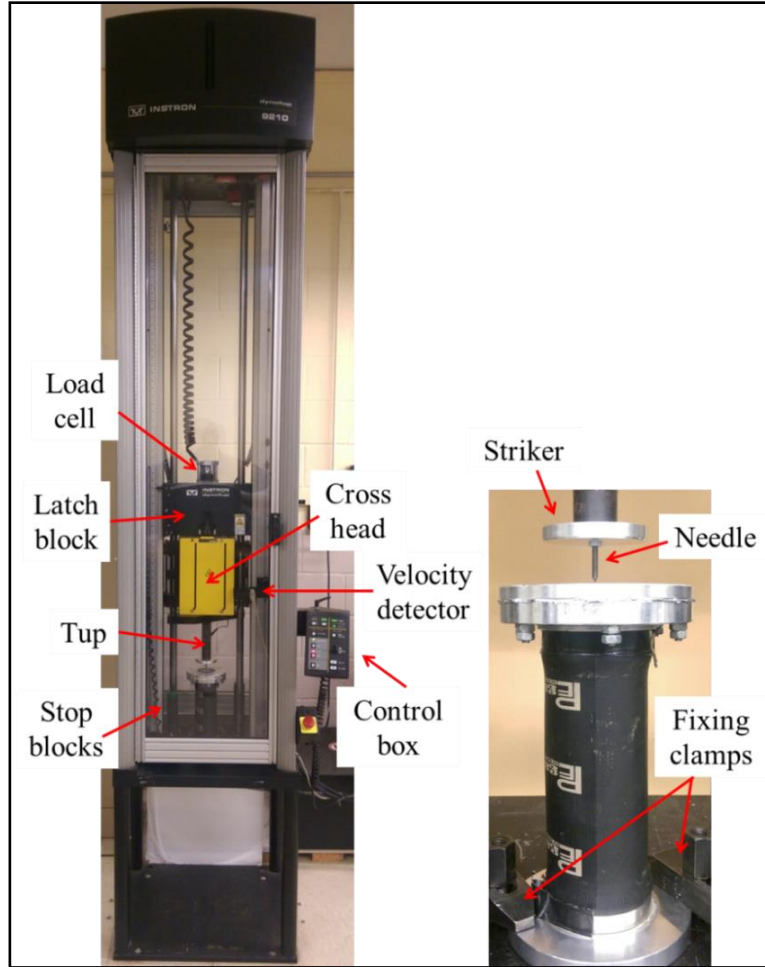
Fig. 2: *Left*: Instron Dynatup 9210 drop tower. *Right*: Striker-needle assembly and clamps for fixing the system device

The mitigation device was held inside the testing machine enclosure and was fully clamped during experimentation as shown in Fig. 2. The positioning of the device inside the enclosure allowed it to be oriented in such a way that a high speed photography system could be employed during testing.

During the experiments the total mass of the impacting system has to be taken into account. Table 3 shows the mass of all components contributing to the impact. The needle lengths negligibly contributed to the impactor mass.

Table 3: Total mass of the drop weight

Components	Reaction plate and bolts	Tup and Bolt	3" (76.2 mm) flat striker	Cross Head	Weights	Total Mass
Mass (Kg)	1.39	0.85	0.07	4.79	0.0	7.1

The system device was subjected to approximately 5.0 to 30.0 J of low velocity impact with a 76.2 mm (3 in) diameter flat surface circular cross section striker installed on the tup. Given the impact energy and known mass of the drop weight, the drop height, h, was determined by

$$h = \frac{E}{mg} \tag{2}$$

where E is the desired potential energy, m is the mass of the drop weight, and g is the acceleration due to gravity.

After the drop height was determined, the drop tower velocity was determined. The device was placed in the testing machine enclosure and the cross head was lowered until it came into contact with the device. Figure 2 shows the device placed in the supports with the striker/needle assembly in contact with the device. The velocity sensor must be adjusted so that the velocity flag attached to the crosshead is in line with the bottom of the sensor. With the sensor adjusted, the number indicated on the scale was taken as a datum point and the calculated drop height was set from the datum. The crosshead was raised to the appropriate height and the device was removed. A velocity test was then completed to ensure that the proper velocity was reached. Impact velocities were checked against a calculated velocity determined by

$$v = \sqrt{2gh} \tag{3}$$

Before experiments were performed, the data acquisition system was configured. Each tup has a calibration factor that must be inputted into the software. The system was configured using the correct calibration factor for the 10,000 lb tup. After the calibration factor was entered, the sampling rate was properly chosen. The sampling rate determines if the entire event is captured. The data acquisition system records 8192 data points regardless of the sampling rate, therefore, it is important to know the duration of the impact event. For the given study, the event duration was approximately 50 ms. A sampling rate of 81.92 KHz was chosen as this corresponds to 100 ms allowing for a proper margin of safety. For more information on the test machine description, parts functions, running preparations, and the operational specifications, see reference manual [14].

3. Experimental Results and Discussion

3.1 Effectiveness of the Produced Mitigating Shock

In an effort to better understand the various factors that affect this device's ability to mitigate impact loading, a range of factors were independently tested.

3.1.1 Influence of the Time of Emission of Shock on Mitigating the Impact Loading

The first series of drop weight experiments investigates the optimal release time of the shock (needle penetration length) on the mitigation of impactor energy. Three needle lengths were utilized ($\ell_1 = 6$ mm, $\ell_2 = 12$ mm, and $\ell_3 = 18$ mm) as shown in Fig. 3a in order to control the onset of the shock release. The smallest needle was designed to release the shock late in the impact history after the impactor has already

59

made contact with the bladder; the second longest needle was designed to release the shock quickly after the impactor had contacted the bladder and lastly the longest needle was designed to release the shock prior to the impactor contact. The drop tower was outfitted with a mass (m_1) of 8.58 kg and drop height (h_1) of 0.3 m (see Fig. 3a). Initially, the impactors were given the same potential energy (E_o) of 25.3 J. The bladder's pressure (P_o) was kept constant at 345 KPa.
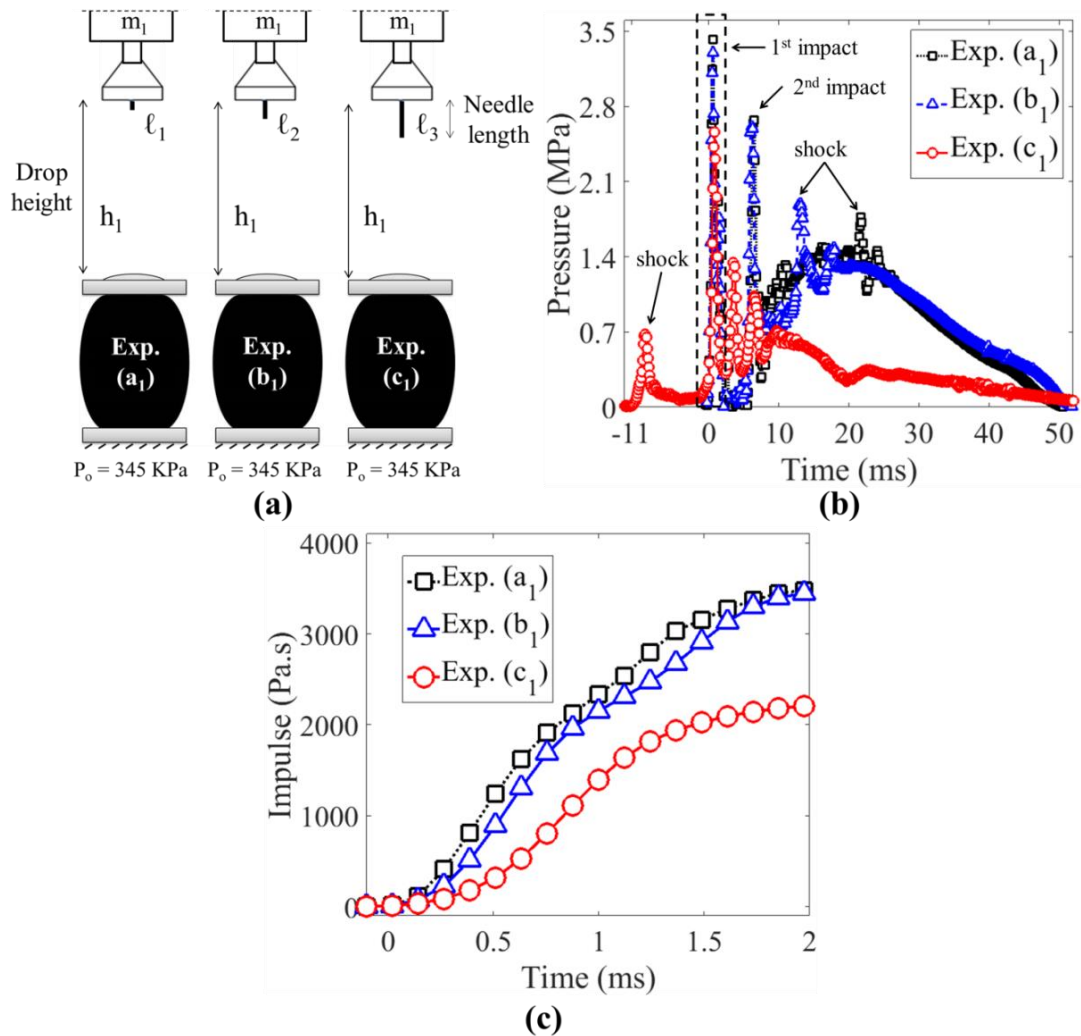
Fig. 3: (a) Series (I) of drop weight experiments, (b) the resulted pressure-time history showing the influence of using varying needle lengths on the mitigation of impactor load, and (c) the impulse reduction from the anti-shock mechanism

60

The pressure-time history of each impactor is shown by Fig. 3b. At t = 0 ms, the impact initiates (1st impact) between the striker assembly and the mitigation device, observed by the sharp spike in load and the sudden drop in the impact velocity. At this time, experiments (a_1, b_1) showed pressure peaks of 3.5 MPa, whereas, experiment (c_1) showed a maximum peak pressure of 2.5 MPa. This peak load reduction corresponds to the presence of the shock load, which decelerates the impactor before contact (at t = -10 ms). This time corresponds to the emission of the shock for the case of longer needle length of ℓ_3 = 18 mm (see Exp. (c_1)). This shock had a peak pressure of 0.72 MPa, a rise time of about 0.85 ms, and showed an exponential decay period of approximately 2.0 ms. For shorter needle lengths of ℓ_1 = 6 mm and ℓ_2 = 12 mm, the anti-shock load was produced later in time at t = 22 ms and t = 12 ms (with first contact being prescribed as t = 0) respectively with pressure peak of about 1.7 MPa. For these two cases, it was noticed that the anti-shock load was produced after a second impact (the impactor initially bounced). This second impact had a peak pressure of 2.7 MPa at t = 6.4 ms. During (6.4 ms $\leq$ t $\leq$ 22 ms) and (6.4 ms $\leq$ t$\leq$ 11 ms), increase in pressure was observed in the pressure profiles for experiments (a_1, b_1). This increase is an artifact of the rubber tube material rebounding.

The impulse reduction from the anti-shock mechanism is shown in Fig. 3c. This was simply obtained by integrating the pressure-time data of the first impact pressure (see the dashed box in Fig. 3b). As discussed above, when the needle length was increased from 6 mm to 18 mm, the maximum impulse resulting from the first impact decreased from 3500 Pa.s to 2200 Pa.s. Therefore, the anti-shock device under

these conditions reduces or mitigates the impactor impulse on the bladder by approximately 37%.

3.1.2 Influence of Impact Velocity

After determining the optimal needle length such that the anti-shock is released prior to impact, the second set of experiments was performed to investigate the influence of impactor velocity on the effectiveness of the mitigating shock device. A constant needle length (ℓ_3 = 18 mm) was used for each of the following set of experiments. The systems inner pressure was kept constant at 345 KPa and impactor velocity was changed by differing starting height. For this specific case, three drop heights were selected (h_1 = 0.3 m, h_2 = 0.2 m, and h_3 = 0.1 m) as shown by Fig. 4a. The impactor's mass was kept constant at 8.58 kg, thus experiments a_2, b_2, and c_2 were given potential energies of 25.3, 16.8, and 8.4 J respectively.

The produced shock load was applied over a central circular area of 59 mm in diameter. The pressure profiles of each experiment are shown by Fig. 4b. These pressures represent the pressure applied onto the impactor by the produced shock. The time t = 0 ms corresponds to the emission of the shock. It should be noted that this time (t = 0 ms) no longer corresponds to the first contact as described in Series I. The produced shock in experiment (a_2) showed a peak pressure of 0.72 MPa and experiments (b_2, c_2) showed peak pressure of 0.3 MPa and 0.2 MPa, respectively. It should be noted that the peak pressure applied by shock is higher in experiment (a_2) as compared to peak pressures in experiments (b_2, c_2). This is because it is being hit by the shock closer to the bladder. The pressure profiles had a rise time of about 0.85 ms and showed an exponential decay period of approximately 2.0 ms, 1.5 ms, and 1.1 ms

for experiments a_2, b_2, and c_2. As the impactor velocity decreases, both the period of the produced pressure profile and peak pressure decreased, which results in a lower impulse imparted to the impactor as shown by Fig 4c. When the impactor velocity was increased from 1.4 m/s to 2.4 m/s, the impulse imparted onto the impactor increased by approximately 209% (385 Pa.s to 1190 Pa.s). It is to be noted that the impulse imparted onto the impactor decreased by 37% when the impactor velocity was decreased from 2.0 m/s to 1.4 m/s.
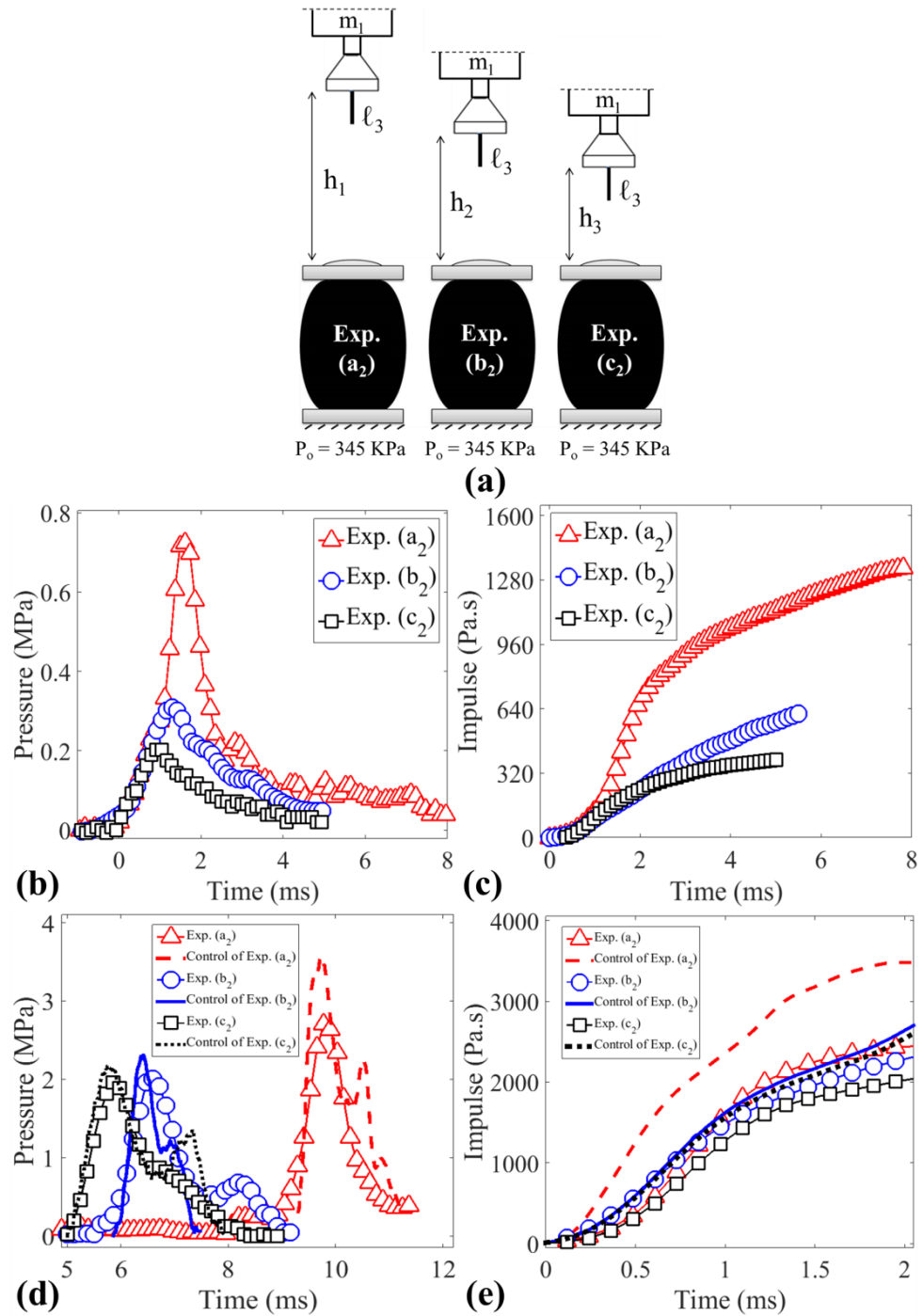
Fig. 4: (a) Series (II) of drop weight experiments, (b) the produced pressure profiles at different impact velocities, (c) true duration of the imparted impulse on the impactor, (d) the pressure exerted onto the bladder by the impactor, and (e) the calculated impulse exerted onto the bladder by the impactor

The pressure exerted onto the bladder by the impactor for experiments (a_2, b_2, and c_2) is shown by Fig. 4d. The time between the impactor-shock and impactor-bladder interactions were 8.0, 5.5, 5.0 ms and had corresponding peak impact pressures of 2.7, 2.2, and 2.0 MPa, respectively.

Control experiments were performed under the same conditions, but without the anti-shock being released at any point, as in the experiments in series II. These control experiments were conducted to evaluate the impact pressure reduction from the anti-shock mechanism. These experiments were added as a reference (as seen in Fig. 4d) for each of the data sets of experiments (a_2, b_2, and c_2). The control of experiment a_2 had an impact peak pressure of 3.6 MPa and the control of experiments (b_2, c_2) showed impact pressure peaks of 2.3 MPa. It is noticeable that the pressure exerted onto the bladder by the impactor increases as the impact velocity (energy) increased under a constant inner system's pressure condition.

With higher impact velocities, the anti-shock mechanism has a greater load reduction. This is due to the impactor approaching the pressure release at higher velocities. Thus, getting closer to the pressure release sooner and experiencing higher emitted shock pressures. This load reduction can be better seen represented by the impulse as shown in Fig. 4e. In experiment (a_2), the impactor impulse on the bladder was reduced by approximately 37%, whereas, experiments (b_2, and c_2) showed load reduction of about 12%.

3.1.3 Influence of Inner System's Pressure

As discussed earlier, the mitigating pressure release property of the device at lower impact velocities had little effect in mitigating the incoming body (see

experiment c_2) as compared to shocks generated at higher impact velocities, which showed greater load reduction. One way to increase the effectiveness of the produced mitigating shock at low impact velocities is to increase the internal pressure of the device. To test this, experiments were carried out at different inner system pressures in comparison to previous experiments to produce higher levels of anti-shock.

Three inner system's pressures (P_o) were selected to be 345, 517, and 690 KPa (50, 75, and 100 Psi) for experiments a_3, b_3, and c_3. The drop tower was outfitted with a mass (m_2) of 7.1 kg and drop height (h_4) of 0.08 m (see Fig. 5a) thus having a potential energy (E_o) of 5.6 J. The needle length ($\ell 3 = 18$ mm) was kept constant for each of the following experiments.

The pressure profile of each experiment is shown by Fig. 5b. These pressures represent the pressure applied onto the impactor by the produced shock. The time at t $= 0$ ms corresponds to the emission of the shock. The produced shock in experiment (a_3) had a peak pressure of 0.18 MPa and experiments (b_3, c_3) showed peak pressure of 0.37 MPa and 0.53 MPa, respectively. The pressure profiles had a rise time of about 0.85 ms and showed an exponential decay period of approximately 1.0 ms, 1.3 ms, and 1.5 ms for experiments a_3, b_3, and c_3.
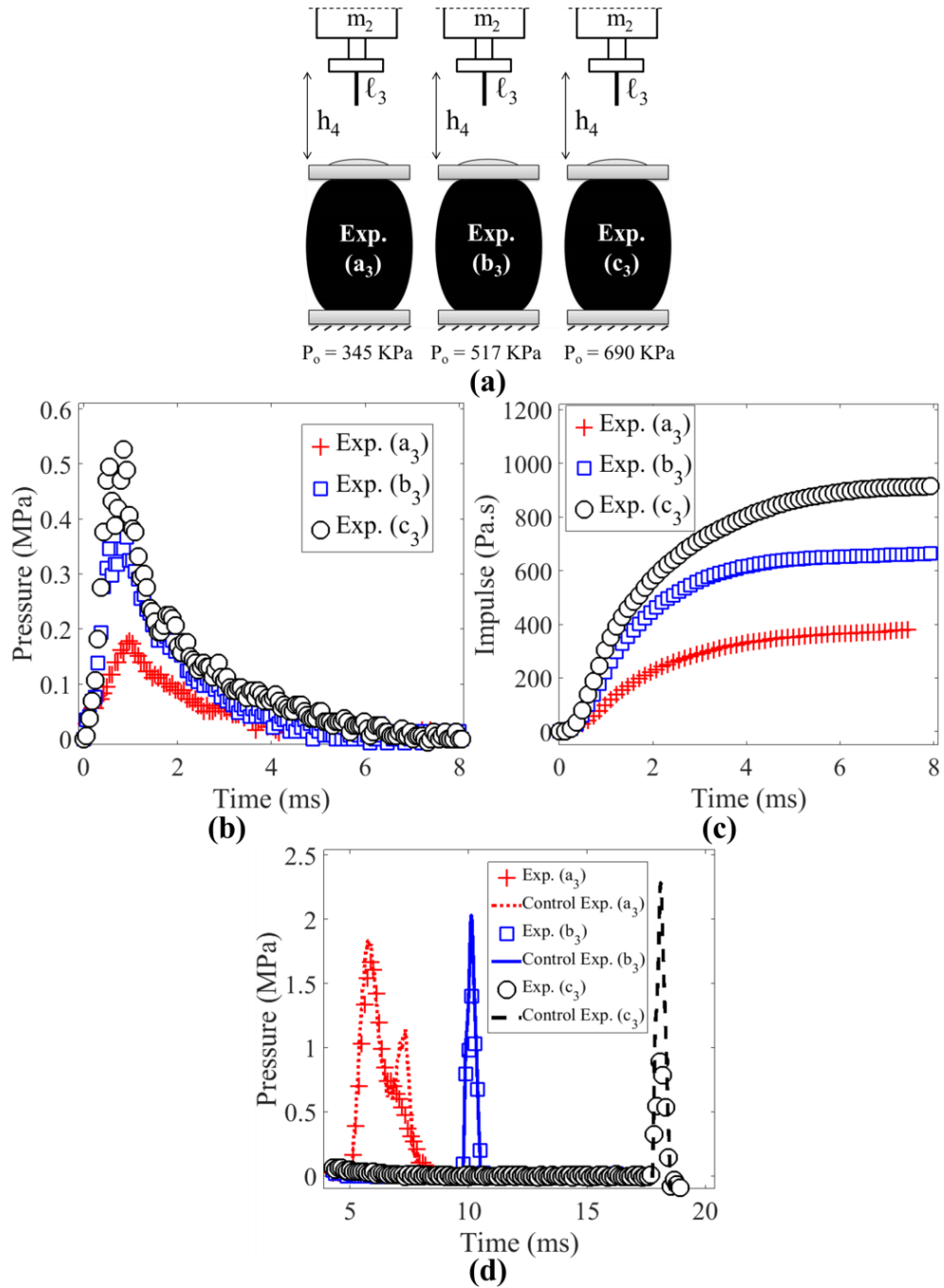
Fig. 5: (a) Series (III) of drop weight experiments, (b) the resulted pressure profiles show the effect of changing the inner system's pressures, (c) true duration impulse of the produced shock, and (d) the pressure exerted onto the bladder by the impactor

As the internal pressure of the anti-shock device increased, both the period of the pressure profile and peak pressure increased, which resulted in a higher impulse imparted to the impactor as shown by Fig 5c. When the inner system's pressure was increased from 345 to 690 KPa, the maximum impulse imparted to the impactor increased by approximately 160% (380 Pa.s to 1000 Pa.s). It is noticeable that the impulse imparted to the impactor increased by approximately 68% when the inner system's pressure was increased from 345 to 517 KPa.

The pressure exerted onto the bladder by the impactor for experiments (a_3, b_3, and c_3) is shown by Fig. 5d. The time of impacts, after the initiation of the shock, on the bladder were 5.0, 10.0, and 18.0 ms and had corresponding peak impact pressures of 1.8, 1.5, and 1.0 MPa, respectively. This indicated that the anti-shock delayed the time of impact loading and decreased the peak impact load as the internal pressure increased. A decrease of 45% peak impact load is observed as the inner pressure of the anti-shock device increased by 100%.

Control experiments were performed under the same conditions, but without the anti-shock being released at any point, as in the experiments in series III. These control experiments were conducted to evaluate the impact pressure reduction from the anti-shock mechanism. These experiments were added as a reference (as seen in Fig. 5d) for each corresponding experiment (a_3, b_3, and c_3) and showed impact peak pressures of 1.9, 2.2, and 2.4 MPa, respectively. It is noticeable that the pressure exerted onto the bladder by the impactor increased as the internal pressure of the device increased under constant impact energy. As the inner pressure of the anti-shock

device increased by 100%, there was a corresponding increase of about 27% in the peak impact pressure.

The load reduction from the anti-shock mechanism is shown in Fig. 5d. Experiments (a_3, b_3, and c_3) showed a load reduction of 5%, 32%, and 58%, respectively. In other words, when the internal pressure of the device was increased by 100% (experiments c_3), the anti-shock mechanism showed a greater load reduction of 58%. Therefore, mitigating the effect of normal impact loadings under lower impact velocities was achieved by producing higher levels of anti-shock.

3.2 Impactor Energy Mitigation

The applicability of the anti-shock device in mitigating the velocity and kinetic energy of the incoming body (impactor) is discussed in this section. Experiment c_3 is given as an example to explain the mitigation process. The velocity and kinetic energy of the impactor as a function of displacement are plotted in Fig. 6. A 2D-DIC technique was used as validation during the dynamic event and the data is presented as solid circles in Fig. 6a, b. For purposes of comparison with experimental values, the velocity and corresponding kinetic energy of the impactor unhindered by the anti-shock is presented as a solid black line in Fig. 6a, b. The real time images of the incoming impactor are shown by Fig. 6c.

Recall that in experiment c_3 the anti-shock device had a stored potential energy of 800 J (see Table 2). The impactor impacted with a velocity of $v_e = 1.5$ m/s and kinetic energy of $E_e = 8.0$ J prior to the emission of the anti-shock (while in contact) at distance of $x_e = 0$ mm. Then, the impactor decelerated during the anti-shock load and reached a temporal minimum velocity (v_{tm}) of 1.2 m/s and a corresponding minimum

kinetic energy (E_{tm}) of 5.0 J at distance of x_{tm} = 6.84 mm at a time t_{tm} = 5.7 ms. After

this time, the anti-shock had a lower influence on the impactor as it again accelerated

downwards with a net acceleration less than gravity up to the point prior to contact

with the air flask at x_f = 18 mm. At this point ($t_f \approx$ 20 ms), the impactor reached a final

velocity (v_f) of 1.27 m/s and a corresponding kinetic energy (E_f) of 5.7 J.
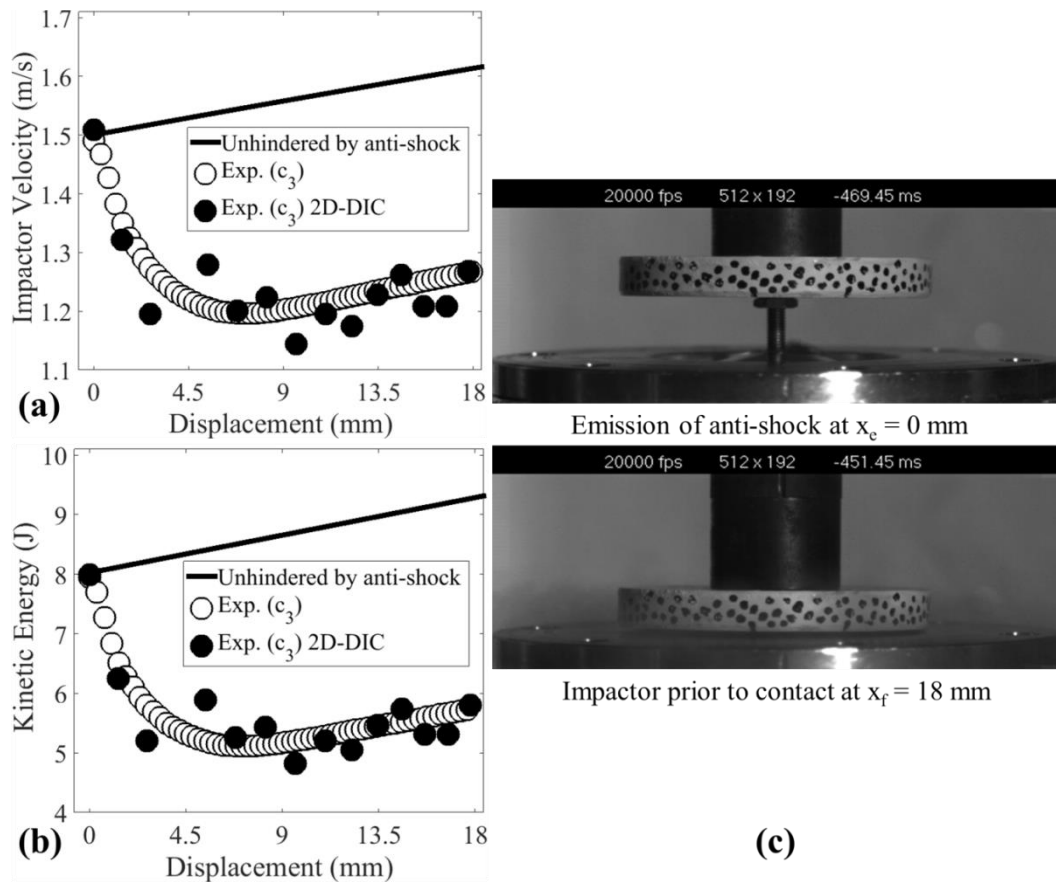
Fig. 6: Impactor (a) velocity, (b) kinetic energy, and (c) real time images during the
anti-shock loading

In comparison to the impactor unhindered by the anti-shock load (see the solid

black line in Fig. 6a, b), the impactor had a velocity (v_u) of 1.55 m/s and a

corresponding kinetic energy (E_u) of 8.5 J at the distance of x_{tm} = 6.84 mm. Prior to

contact with the air flask at x_f = 18 mm, the impactor had a velocity (v'_f) of 1.63 m/s

and a corresponding kinetic energy (E'_f) of 9.5 J. Under these experimental conditions, the anti-shock mechanism mitigated the kinetic energy of the incoming impactor by approximately 40%. A summary of the mitigated kinetic energies for all the experiments is listed in Table 4.

Table 4: Summary of experimental results

Series of experiments		$(E'_f)^*$ [J]	$(E_f)^*$ [J]	$(E_r)^*$ [%]
	$\mathbf{a_1}$	29	29	0
I	$\mathbf{b_1}$	29	29	0
	$\mathbf{c_1}$	29	19	34
	$\mathbf{a_2}$	29	19	34
II	$\mathbf{b_2}$	20	14	30
	$\mathbf{c_2}$	10	8.4	16
	$\mathbf{a_3}$	9.3	7.8	16
III	$\mathbf{b_3}$	9.3	6.6	29
	$\mathbf{c_3}$	9.3	5.6	40
Notes		$(E'_f)^*$: Impactor kinetic energy unhindered by the anti-shock load at $x_f = 18$ mm $(E_f)^*$: Impactor kinetic energy influenced by the anti-shock load at $x_f = 18$ mm $(E_r)^*$: Percentage of energy reduction (Mitigated Energy)		

The influence of varying the impactor kinetic energy on the mitigation effects as the potential energy of the device is held constant at 400 J is shown by Fig 7a. It is seen that an increase in the kinetic energy of the impactor led to a higher mitigation effect as shown by series II. However, this mitigation effect does not scale linearly with incoming kinetic energy. In other words, when the kinetic energy of the incoming impactor initially increased by 100% (from 10 to 20 J), there was an extremely rapid increase in the mitigation percentage of about 88%. Whereas, this mitigation effect continually becomes shallower of about 13% when the kinetic energy of the impactor increased to 30 J.

Moreover, an increase in the potential energy of the device also increases the energy mitigation as shown by series III. This mitigation effect increases linearly with increasing the potential energy of the device at a constant kinetic energy of the impactor as shown in Fig. 7b. This means that as the potential energy of the device increases, the mitigation effect also increases by the same percentage.
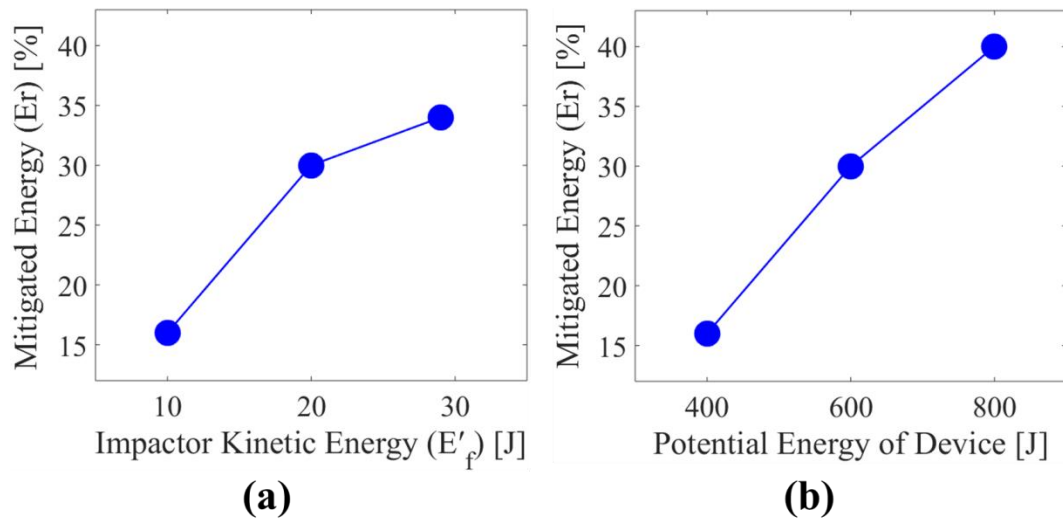
Fig. 7: Mitigation effects given by (a) series II and (b) series III

Overall, there are two factors affecting the percentage mitigation of the device. The first is the impactor velocity. With a higher impactor velocity, the percentage of mitigation increases nonlinearly. The second is the potential energy of the device. With a higher potential energy of the device, the increase in the percentage of mitigation is proportional. Therefore, this device is ideal for situations where the impact velocity is high and/or the potential energy of the device is high.

4. Conclusions

A new system was designed to mitigate the impact forces during a collision using shock loading. Drop-weight impact experiments were performed to determine the efficacy of this new mitigation technique. This technique has been found effective in mitigating the kinetic energy imparted on to the structure and in reducing the impactor peak load during collision. The following is the summary of the investigation:

- The first series of drop weight experiments investigated the optimal needle length (such that the anti-shock is released prior to collision) on the mitigation of impactor load/energy. For the experiments conducted, the device mitigates impact more effectively as needle length increases indefinitely.

- For the second series of experiments, which investigated the effect of impact velocity on the effectiveness of the device, it was found that with higher impactor velocities the anti-shock mechanism produced a greater load reduction.

- Mitigating the effect of normal impact loadings under lower impact velocities was achieved by producing higher levels of anti-shock. The results indicated that when the stored potential energy of the device was increased from 400 J to 800 J, the maximum impulse imparted to the impactor by the produced shock increased by approximately 160%. In addition, the results indicated that the anti-shock device with 800 J of stored energy delays the time of impact loading three times more as compared to anti-shock device with 400 J.

- Overall, the device effectively mitigates impact for higher impact velocities

and for higher bladder pressures, decreasing peak loads during impact by up to 58% and energy imparted on the structure by 40%.

Acknowledgment

References

[1] Paden, B. E., Kelly, P. M., Hines, J. A., Bothman, D., & Simms, C. (2016). On the feasibility of life-saving locomotive bumpers. Accident Analysis and Prevention, 89, 103–110

[2] Lee, Y. H., Joo, Y. J., Park, J. S., Kim, Y. S., & Yim, H. J. (2014). Robust design optimization of frontal structures for minimizing injury risks of Flex Pedestrian Legform Impactor. International Journal of Automotive Technology, 15(5), 757–764

[3] Mallory, A., Fredriksson, R., Rosén, E., & Donnelly, B. (2012). Pedestrian Injuries By Source: Serious and Disabling Injuries in US and European Cases. Association for the Advancement of Automotive Medicine. Association for the Advancement of Automotive Medicine. Scientific Conference, 56, 13–24.

[4] Matsui, Y. (2014). Possibility of installing a data acquisition system in a pedestrian headform impactor. International Journal of Crashworthiness, 19(2), pp 115-125

[5] Niebuhr, T., Junge, M., & Achmus, S. (2015). Expanding pedestrian injury risk to the body region level: how to model passive safety systems in pedestrian injury risk functions. Traffic Injury Prevention, 16(5), 519–31

[6] Lv, X., Huang, X., Gu, X., Liu, W., & Li, G. (2016). Reliability-based multiobjective optimisation of vehicle bumper structure holes for the pedestrian flexible legform impact. International Journal of Crashworthiness, 21(3), 198–210

[7] Zhang, G., Cao, L., Hu, J. and Yang, K. H. (2008). A field data analysis of risk factors affecting the injury risks in vehicle-to-pedestrian crashes. Annual Proceedings / Association for the Advancement of Automotive Medicine. Association for the Advancement of Automotive Medicine, 52, 199−214

[8] Broggi, A., Cerri, P., Ghidoni, S., Grisleri, P., & Jung, H. G. (2009). A new approach to urban pedestrian detection for automatic braking. IEEE Transactions on Intelligent Transportation Systems, 10(4), 594–605

[9] Carsten, O. M. J., & Tate, F. N. (2005). Intelligent speed adaptation: Accident savings and cost-benefit analysis. Accident Analysis and Prevention, 37(3), 407–416

[10] Lim, J. H., Park, J. S., Yun, Y. W., Jeong, S. B., & Park, G. J. (2015). Design of an airbag system of a mid-sized automobile for pedestrian protection. Proceedings of the Institution of Mechanical Engineers Part D-Journal of Automobile Engineering, 229(5), 656–669

[11] Yang, H.-I., Yun, Y.-W., & Park, G.-J. (2015). Design of a pedestrian protection airbag system using experiments. Proceedings of the Institution of Mechanical Engineers, Part D: Journal of Automobile Engineering

[12] Choi, S., Jang, J., Oh, C., & Park, G.-J. (2016). Safety benefits of integrated pedestrian protection systems. International Journal Of Automotive Technology, vol 17, Springer Nature, pp 473–482

[13] Sutton, M. A., Orteu, J.-J., & Schreier, H. W. (2009). Image correlation for shape, motion and deformation measurements: Basic concepts, theory and applications. Image Correlation for Shape, Motion and Deformation Measurements: Basic Concepts,Theory and Applications.

[14] Corporation, I. (1999). Instron Dynatup 8250 Drop Weight Impact Tester User Manual.

CHAPTER 4: BLAST PERFORMANCE OF PERFORATED STRUCTURES

by

Emad A. Makki, Murat Yazici and Arun Shukla

under preparation for submission to the Journal of Engineering Structures

Corresponding Author: Emad A. Makki

    Dynamic Photo Mechanics Laboratory

    Department of Mechanical, Industrial and Systems

    Engineering

    University of Rhode Island

    94 Upper College Road

    131 Kirk Applied Engineering Laboratory

    Kingston, RI, 02881, USA

    Phone: +1-401-874-2283

    Email Address: emakki@my.uri.edu

Abstract

An experimental study was conducted to examine the induced pressure from the interaction of a planar shock front and perforated plates under different boundary conditions using the shock-tube facility. Two series of experiments with variations in the blockage ratio, net hydraulic diameter, shapes, and sizes of the orifices, were conducted. In the first part of this study, shock wave loading experiments on freestanding perforated plates were conducted to evaluate the reflected pressure pulses and the motion response for all the targets with and without perforations. The second part of this study conducted on clamping all of the targets inside the shock-tube to evaluate the reflected and transmitted pressure pulses. During each experiment, pressure histories caused by the interaction of the incident shock wave with the plates were recorded. During the fluid structure interaction time, the side-view images of the targets were recorded using a single high-speed camera to identify the motion response of each plate configuration. The influence of varying the incident shock wave Mach number on the pressure profile was examined under clamped boundary conditions. The experimental results show that as the blockage ratio of the freestanding perforated plate decreased from 100% to 65%, the reflected peak pressure decreased by 26%, the maximum impulse imparted to the perforated plate decreased by 33%. During the fluid-structure interaction process, as the blockage ratio of the freestanding perforated plate decreased from 100% to 65%, the plate's momentum, velocity, and kinetic energy decreased by approximately 60%, 61%, and 84% respectively. At constant plate's blockage ratio, the results indicate that the hydraulic diameter or the net perforation perimeter had no influence on the plate's velocity and

kinetic energy profiles during the fluid-structure interaction process. Furthermore, it was determined that the hydraulic diameter of the perforated plates had an effective influence on the reflected and transmitted shock waves at close by regions upstream and downstream. For larger distances upstream and downstream, the specific shape and size of the perforations on the plate had practically no influence on the recorded pressures as long as the porosity is kept at a constant value. An increase in the incident shock wave Mach number led to a higher impulse of the reflected and transmitted shock waves. However, this effect does not scale linearly with the incident shock wave Mach number. When the boundary condition changed from free to fixed, the maximum areal impulse imparted to the perforated plate was increased by approximately 194%.

Keywords: Perforated plates • Free standing boundary conditions • Clamped boundary conditions • Blast mitigation

1. Introduction

Blast mitigation techniques such as perforated structures are the focus of numerous studies because of their relevance in attenuating blast waves and reducing its pressure and damaging effects. Britan et al. [1, 2] showed that the shock wave attenuation can be attained by orifice plates and grids, the inclination angle of the barrier, its width, opening ratio, and the incident shock wave Mach number determine the shock wave attenuation. Ram and Sadot conducted numerical studies to develop constitutive relations and validate experimental results [3, 4]. Zhou and Hao carried out numerical simulations to study the effectiveness of blast barriers for blast load reduction. The results showed that a blast barrier not only reduces the peak reflected

pressure and impulse on a building behind the blast barrier, but also delay the arrival time of the blast wave. An approximate formula was derived to estimate the reflected pressure-time history on a building behind a blast barrier [5].

The use of mild steel perforated plates as a passive mitigation system has been widely studied. Langdon et al. [6] observed that the effect of the blast loading on a structure is reduced when a perforated plate is placed on the path of the blast wave traveling down a tube, especially when the plate is well spaced apart from the target. The number of perforated plates inserted determines the degree of deflection of the deformed target plate. With one perforated plate, the deflection is reduced by 65 to 75 percent while it is reduced to 90 to 95 percent with two perforated plates. Furthermore, Langdon et al. [7] studied the effects of perforated plate blockage ratio (BR) on blast mitigation. They showed that the damage imparted to the target plates is effectively reduced only with perforated plates with the smallest hole size (BR= 96 %). Moreover, blockage ratios of 25% and 50% may not affect the target plate's mid-point deflection, however, with blockage ratio above 50%, the target plate mid-point deflection for a given impulse as well as the threshold impulse of the target plates are reduced. In addition, the separation distance has been found to influence the performance of perforated plates in blast wave shielding. Langdon et al. [8] reported that the mid-point deflection is reduced with an increase in separation distance. They also found that when the blockage ratio is increased to 75% above, a significant decrease in the target plate mid-point deflection is obtained for a given impulse and irrespective of the separation distance. Similar pressure-mitigating behaviors have been observed in Nano-structured porous materials [9] and reticulated foam [10].

Furthermore, it has been demonstrated that fixed barriers can reduce both static pressure and stagnation or reflected the pressure of the shock wave, but free obstacles such as dust reduces static pressure, however increases the reflected pressure [11].

The purpose of the study detailed in this chapter was to expand on previous research in this field by examining perforated plate response to shock loading under different boundary conditions. Furthermore, the aim of this work was to provide a more comprehensive understanding of the fluid-structure interaction of such plates with blast loading. The interaction of shock waves with perforated plates of different blockage ratios and different perforation geometries and sizes was examined. Using the state-of-the-art facilities at the University of Rhode Island's Dynamic Photomechanics Laboratory, circular specimens with varying perforation properties were subject to blast loading initiated by the facility's shock tube. Important variables were independently tested, which include blockage ratio, hydraulic diameter, and perforation perimeter. In every experiment, pressure transducers placed at varying distances from the specimen in order to obtain a complete pressure profile of the event, and a single high-speed camera was positioned to view the in-plane movement of the specimen in order to capture its complete velocity profile. Similar experiments were carried out for both fixed and freestanding perforated specimens.

Upon analysis of experiments on freestanding, it was seen that as the blockage ratio of the fixed perforated specimen decreased from 100% to 65%, the reflected peak pressure decreased by 26%, and the maximum impulse imparted to the specimen decreased by 33%. Similar results were observed in freestanding specimens. This represents the data obtained from the pressure transducer located 15 mm from the

specimen. However, pressure transducers located further away (55 mm and 175 mm) observed similar trends. Furthermore, tests were conducted on specimens with hydraulic diameters (D_h) ranging from 4 mm to 7.1 mm. It was determined that the hydraulic diameter did not have any effect on the initial reflected peak pressure. Of the factors tested, only the blockage ratio affects reflected peak pressure. Finally, as the perforation perimeter of the specimens' perforations decreased, it was observed that higher pressures were present in the build-up regions with respect to the level of the initial peak reflected pressure.

2. Experimental Procedures

In the first part of this study, shock wave loading experiments on free standing perforated plates were conducted to evaluate the reflected pressure pulses and the motion response for all the targets with and without perforations. The second part of this study was on clamping all the targets inside the shock-tube to evaluate the reflected and transmitted pressure pulses for all the targets. To verify consistency and repeatability in the experimental results, at least three experiments were performed on each plate configuration.

2.1 Perforated Plate Specimens

In the present study, the blockage ratio (BR) is simply defined as the area ratio of the solid area of the perforated plate to the exposed area. Three different blockage ratios were selected for this study. A laser perforating technique was utilized to create a uniform round, square, and triangular perforations on the plate specimens. The numbers of holes in the plate, the size of these holes, and the distance between them have been used as design variables to obtain a fixed blockage ratio. The hydraulic

diameter (D_h) is defined as ($D_h = 4A/P$) where A is the total open area in the plate and P is the total perimeter of the holes in the plate. The areal density of all the targets was 38 kg/m^2. A schematic of all targets used in this study is shown in Fig.1 and a summary of their perforations geometry and properties is listed in Table 1.

Plate 1   Plate 2   Plate 3

Plate 4   Plate 5   Plate 6

Plate 7   Plate 8
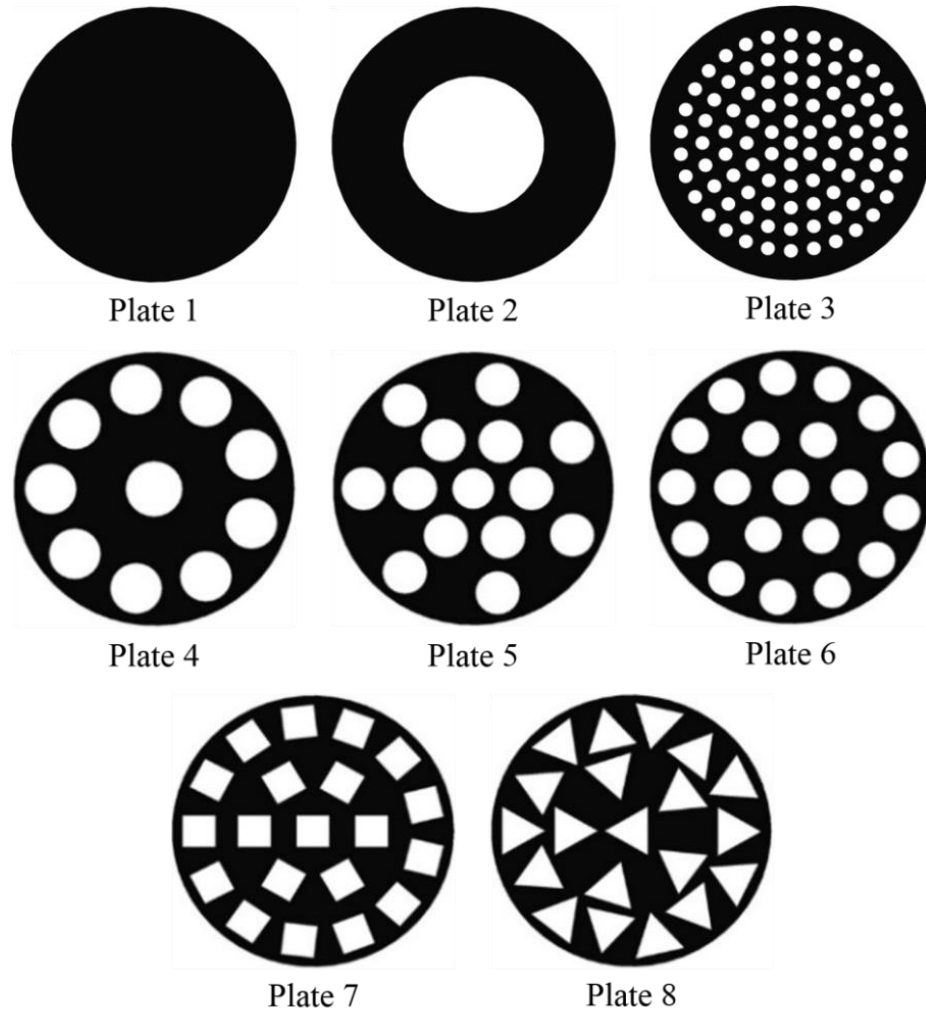
Fig. 1: Geometry of the barriers used in the shock tube experiments

Table 1 Characteristics of the barriers used in experiments

Plate #	Plate Thickness (mm)	Plate Areal Density (kg/m²)	Perforation Geometry	Number of Perforation	Perforation Dimension (mm)	Solid Surface Area (mm²)	Net Opening Area [S] (mm²)	Blockage ratio [BR] (%)	Net Perforation Perimeter [P] (mm)	Hydraulic Diameter [Dₕ] (mm)
1	9.6	37.0	----	----	----	1140.0	----	100	----	----
2	12.8	37.0	Circular	1	d = 19.0	854.0	286.0	75	60.0	19.0
3	12.8	37.0	Circular	91	d = 2.0	854.0	286.0	75	572.0	2.0
4	5.0	38.0	Circular	10	d = 7.12	741.0	399.0	65	223.0	7.1
5	5.0	38.0	Circular	14	d = 6.02	741.0	399.0	65	264.0	6.0
6	5.0	38.0	Circular	20	d = 5.04	741.0	399.0	65	317.0	5.0
7	5.0	38.0	Square	20	a = 4.46	741.0	399.0	65	357.0	4.5
8	5.0	38.0	Triangular	20	a = 6.78	741.0	399.0	65	407.0	4.0

2.2 Application of Shock Load

The shock tube facility at the *University of Rhode Island,* shown in Fig.2 a, has already been developed and has the capability to generate a planar shock wave with a controlled overpressure level on a target plate. The shock tube has an overall length of 8 m. It consists of three main sections: high pressurized (driver) section, low pressure (driven) section, and muzzle section. Both the driver and driven sections had a diameter of 0.15 m and were separated by a diaphragm. The muzzle end is the final section of the shock tube facility and has a diameter of 0.0381m, which is also the diameter of the loading area. During experiments, the driver section was pressurized with compressed Helium gas, which created a pressure difference across the diaphragm. When the pressure reaches a critical value, the diaphragm ruptures, forming a shock wave that travels towards the target plate. In the present study, the diaphragm was made up of 1 ply of Mylar sheet which has various thickness of (5, 7, and 10 mil), depending on the peak shock pressure required. The typical incident peak pressures were 0.3, 0.41, and 0.55 MPa, respectively.

2.2.1 Shock Tube for Free-Standing Conditions

The focus of this study was to evaluate the reflected pressure pulses and the motion response for all the targets with and without perforations. The plate specimen was inserted inside the muzzle end perpendicular to the shock tube axis and positioned flush to the muzzle exit (as shown in Fig.2 b). It should be noted that the diameter of the plates was made exactly same as the inner diameter of the shock tube muzzle.

In order to investigate the pressure characteristics of the incident and reflected shock waves (upstream from the perforated plates), three pressure transducers (PCB CA102B) were flush mounted at the muzzle exit. These sensors are denoted as 1, 2, and 3 in Fig.2 b and located at distances of 15 mm, 55 mm, and 175 mm from the plate, respectively. The incident and reflected shock wave velocities in the tube were obtained by using the distance between the consecutive transducers and the shock wave travel time. A digital oscilloscope (TDS3014C) was used to record the pressure history during each dynamic event at 10.0 MegaSamples/s.

(a)   (b)
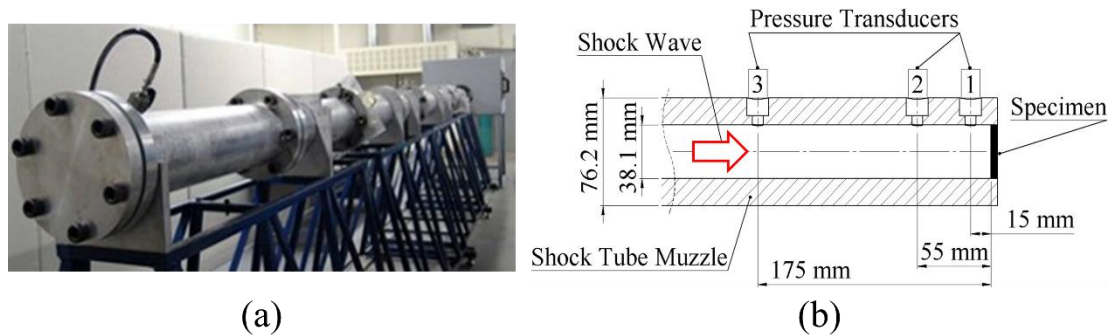
Fig. **2**: (a) The URI shock tube facility (b) detailed dimensions of the muzzle and pressure sensors locations with respect to the plate front face

A (Photron SA1) high speed digital camera was used to capture the real time side-view position of the plate as shown in Fig. 3. Lens was positioned perpendicular

to the motion direction of the specimens and located 2 m away from the shock tube apparatus to avoid image distortion during plate propagation. The camera was set to have a frame rate of 72 000 fps and an image resolution of 384 x 176 pixels. For the illumination of the specimen during the experiments, hydrargyrum medium-arc iodide (HMI) light sources was used, which provided high intensity light required for high speed photography.
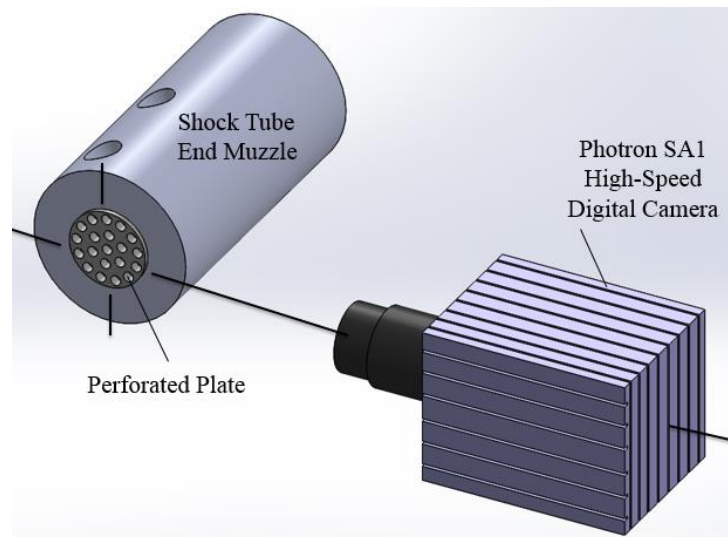
Fig. **3**: Free-standing experimental setup

A typical high-speed side-view image during a shock wave loading process is shown in Fig. 4. Curve fitting methods, such as cubic spline curve fitting, was used to pick up the position of the back face of the specimen. An example of the 7-point cubic spline curve fitting is shown in Fig. 4. Because the specimen did not show any compression during the shock wave loading process, this curve was used to represent the position of the specimen. Then the displacement profile of each point on the specimen was obtained by correlating the position of the specimen in each image to that in the image at time t = 0. The differential of this displacement profile with

respect to the time gives the velocity profile. The momentum of the plate can be evaluated from the velocity profile and the areal density of the plate. The momentum of the plate can be expressed as:

$$I_{Plate} = \oint m_s u_x ds \qquad (1)$$

where, u_x is the x direction velocity and ds is the areal element of the plate.
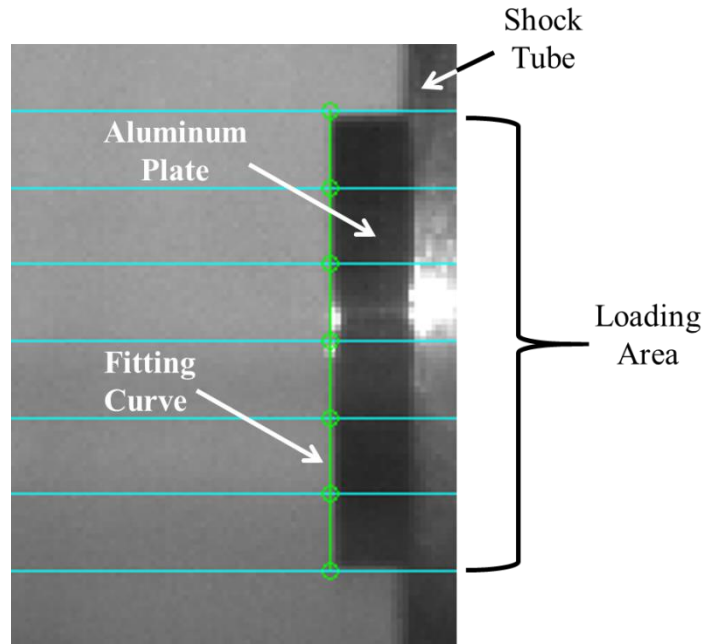
Fig. 4: A typical side-view image and curve fitting of the back face

2.2.2 Shock Tube Modification for Clamped Conditions

The shock tube was modified to measure the pressure history of the incident, reflected, and transmitted waves upstream and downstream from the perforated plates. A detailed fixture design for clamping the perforated plate inside the shock-tube is shown by Fig. 5a. The muzzle end section was aligned and coincided with the fixing element section during experiments using the alignment ring. The inner diameter of both sections had same exact dimensions of 38.1 mm to avoid any wave's reflections

87

that might occur by the fixture itself during the event. For preventing gas leakage through this connection, rubber gaskets were glued between the two sections. The perforated plates were clamped using 8-set screws equally spaced with respect to the radial axis of the fixing element to apply a strong physical contact while the shock wave passing through the perforated plates as shown by Fig. 5b. The modified section was mounted to a rigid wall fixture, open to the air. An image of the back-view of the experimental setup is shown in Fig. 5c.

(a) (b)

(c)
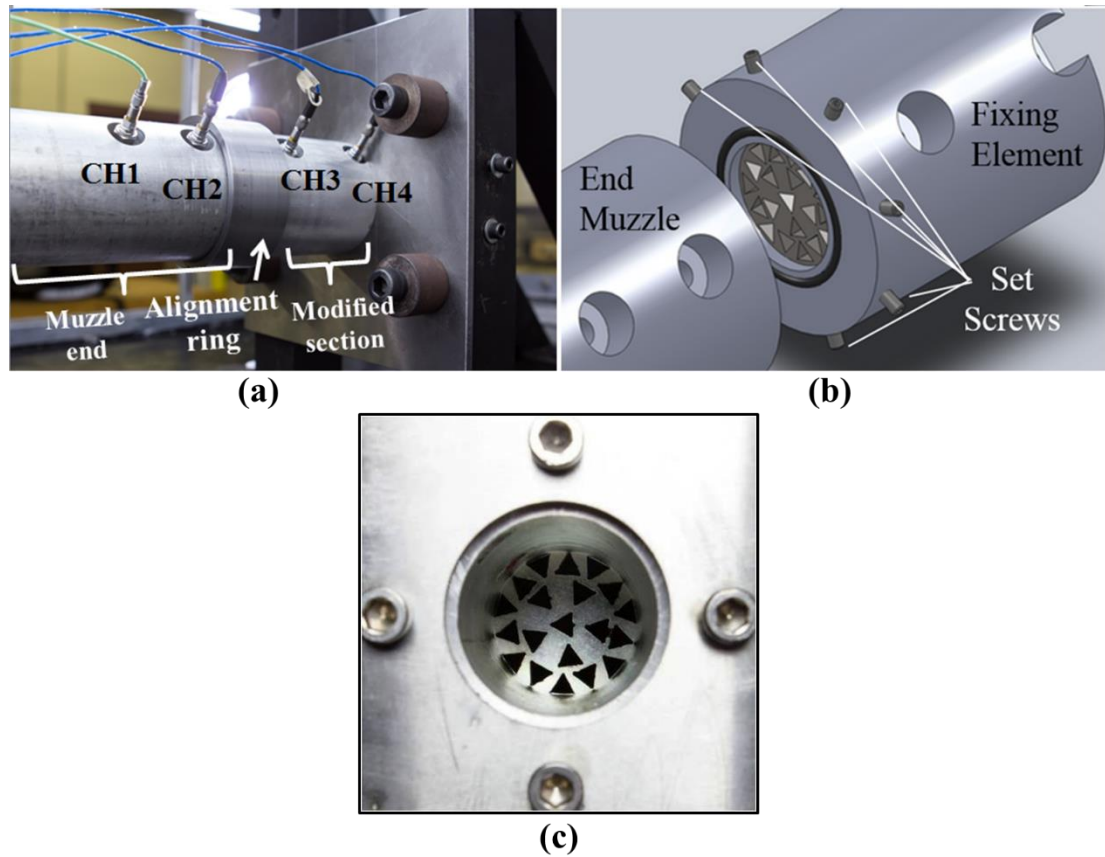
Fig. 5: Modified shock-tube setup for clamping the perforated plates (a) main parts of the fixture design, (b) 8-set screws equally spaced with respect to the radial axis, and (c) open to air duct (back-view image of the experimental setup)

A total of four pressure transducers were used to measure the pressure histories of the incident, reflected, and transmitted shock waves upstream and downstream from the perforated plates. The first two pressure sensors (CH1, CH2) were mounted at the shock tube muzzle end to investigate the "upstream flow" of both incoming and reflected waves, and the other two pressure transducers (CH3, CH4) were mounted on the fixing element part to measure the "downstream flow" of the transmitted waves as they pass through the barrier. A detailed schematic of the pressure sensors locations with respect to the front face and back face of the perforated plate is shown in Fig. 6.
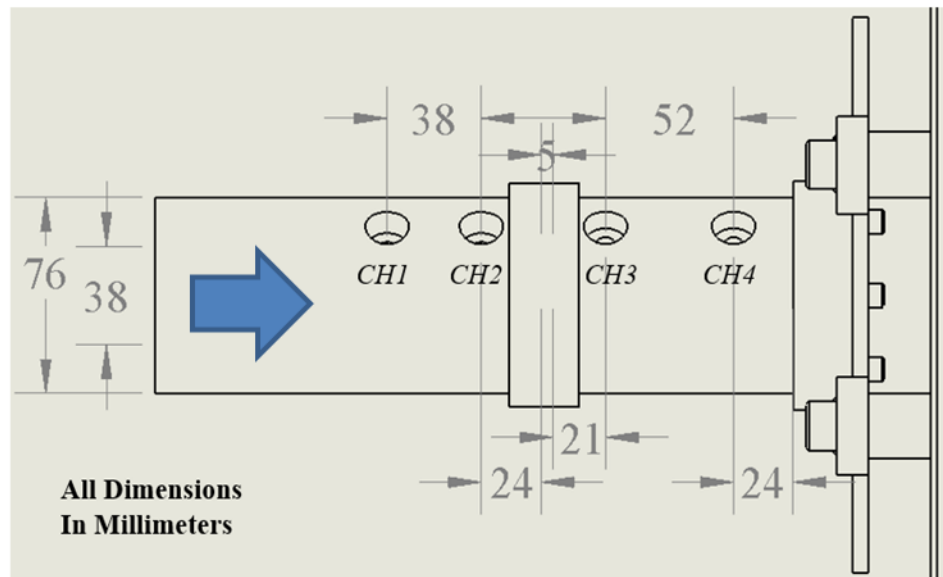
Fig. 6: Pressure sensors locations with respect to the front face and back face of the perforated plate

In order to ensure that no reflection from the shock occurs due to the modified fixture, blank tests were carried out by firing the shock tube and recording the pressure profiles. For this purpose, the apparatus was tested without porous samples. A diaphragm configuration of one stacked ply of Mylar sheet (thickness of 0.178 mm) was used to generate an incident peak pressure of about 0.4 MPa. As the incoming

wave leaves the end muzzle and enters the modified fixture, it is clear that there is no

reflected shock peak as recorded by pressure sensors at CH2 and CH3 (see Fig. 7a).

This can be better represented by the incident pressure profiles and their calculated

areal impulse during the first millisecond as shown in Fig. 7b, c respectively.
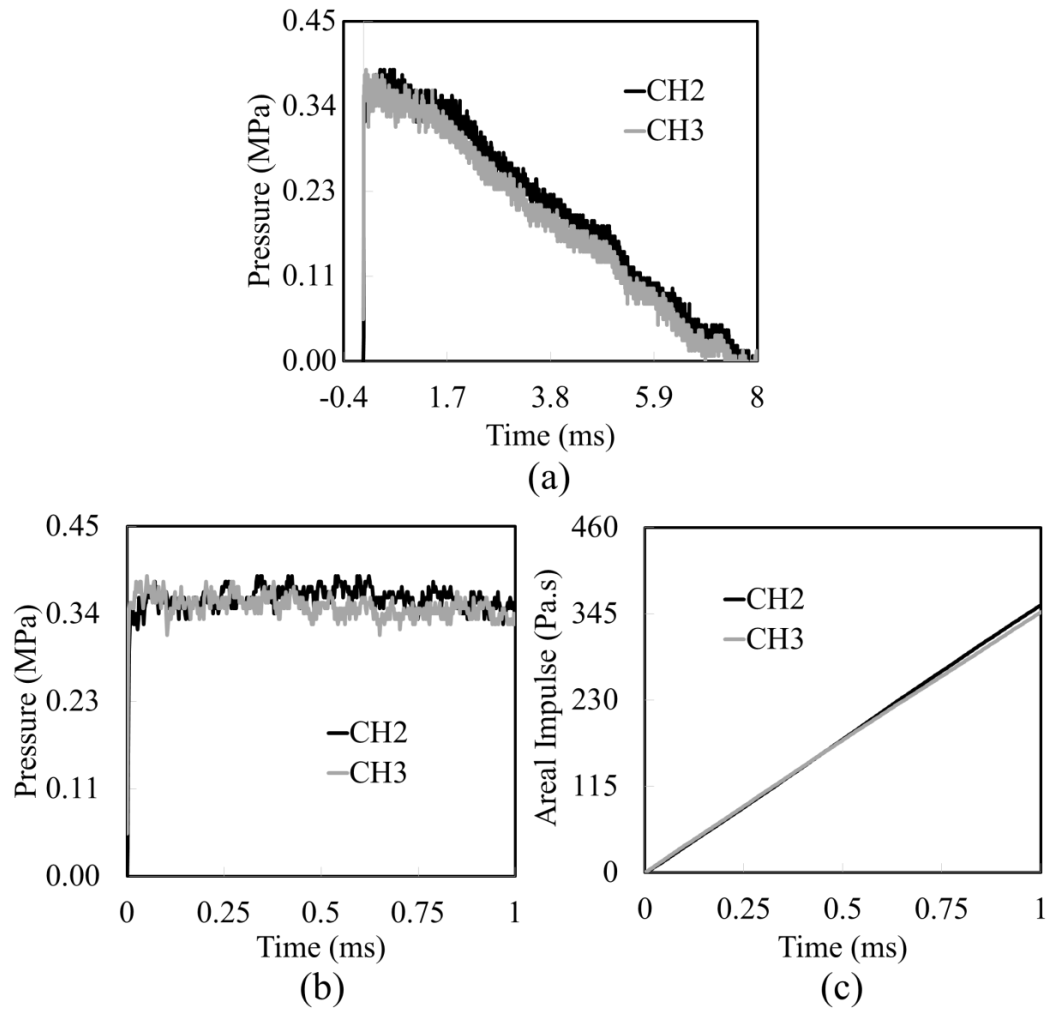
Fig. 7: (a) Recorded incident pressure profiles at (CH2:CH3), (b) validation of not
existing of any reflected shock peak for the first millisecond as the shock wave enters
and exits the modified fixture (c) calculated areal impulses for (CH2:CH3).

3. Experimental Results and Discussion

3.1 Experiments with Free Standing Boundary Conditions

The focus of this study was to evaluate the reflected pressure pulses and the motion response for all the targets with and without perforations. To verify consistency and repeatability in the experimental results, at least three experiments were performed on each plate configuration.

3.1.1 Effect of Plate's Blockage Ratio on the Reflected Pressure Profile

In this study, the effect of the plate's blockage ratio on the reflected pressure signature was examined in a series of experiments conducted with incident shock wave having a peak pressure of 0.27 MPa as shown by Fig. 8a. This figure shows the pressure profiles measured by the pressure transducer closest to the front face of the specimens (15 mm away from specimen front face). Plates 1, 2, and 8 were selected to assess the effect of blockage ratio.
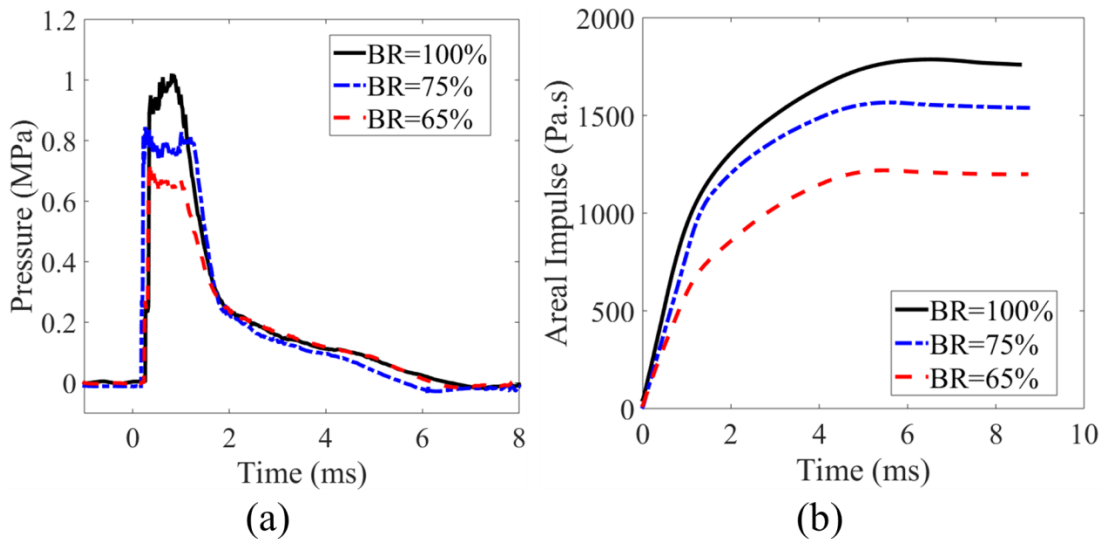
Fig. 8: Recorded reflected pressure profiles (a) 15 mm upstream of the specimens having different blockage ratio of (100%, 75%, 65%), (b) the areal impulse for different plate's blockage ratio. In all cases $M_S = 1.76$

91

The main observations that can be made from these pressure profiles are the following: (i) For different plate's blockage ratio, the incident shock wave traveled inside the muzzle with an average velocity of 600 m/s and was reflected with an average velocity of 300 m/s, translating to approximate Mach numbers of 1.76 and 0.88, respectively. The reflected shock waves had a short rise time of about 0.02 ms and showed an exponential decay period of approximately 1.5 ms. (ii) For the same incident peak pressure, reflected peak pressures are not the same for various plate's blockage ratio. The solid plate with 100% blockage ratio showed a reflected peak pressure of approximately 0.95 MPa, whereas, perforated plates which have 75% and 65% blockage ratio showed reflected peak pressures of about 0.80 MPa and 0.70 MPa respectively. This indicates that when the blockage ratio of the plate was decreased from 100% to 65%, the reflected peak pressure decreased by approximately 26%. In the considered cases, the plate with higher BR% blocks significant part of the duct cross-section, and thus result in a stronger reflected shock wave from the plate. (iii) The overall time period of the load acting on the plates (reflected pressure) was the same for different blockage ratios. The time period is defined as the time at which the pressure becomes equal to the atmospheric pressure. The time period of the reflected pressure was about 6.0 ms. The pressure reduction can be better seen as represented by the areal impulse imparted to the plate as shown by Fig.8 (b). The areal impulse was calculated by integrating the pressure-time data of the reflected pressure profile. The plate with 100% blockage ratio obtained a maximum areal impulse of 1800 Pa.s from the shock loading. When the blockage ratio was decreased from 100% to 65%, the

maximum areal impulse imparted to the plate decreased by approximately 33% (1800 Pa.s to 1199 Pa.s).

For further distances at sensors located 55 mm and 175 mm away from the perforated specimens, the effect of plate's blockage ratio on the reflected peak pressure was still significant as shown by Fig. 9a, b respectively. This indicates that the effect of plate's blockage ratio is highly non-localized, and that effect was not vanished at greater distances upstream. There is no doubt that the net opening area in the plates has an effective influence on the reflected peak pressure.
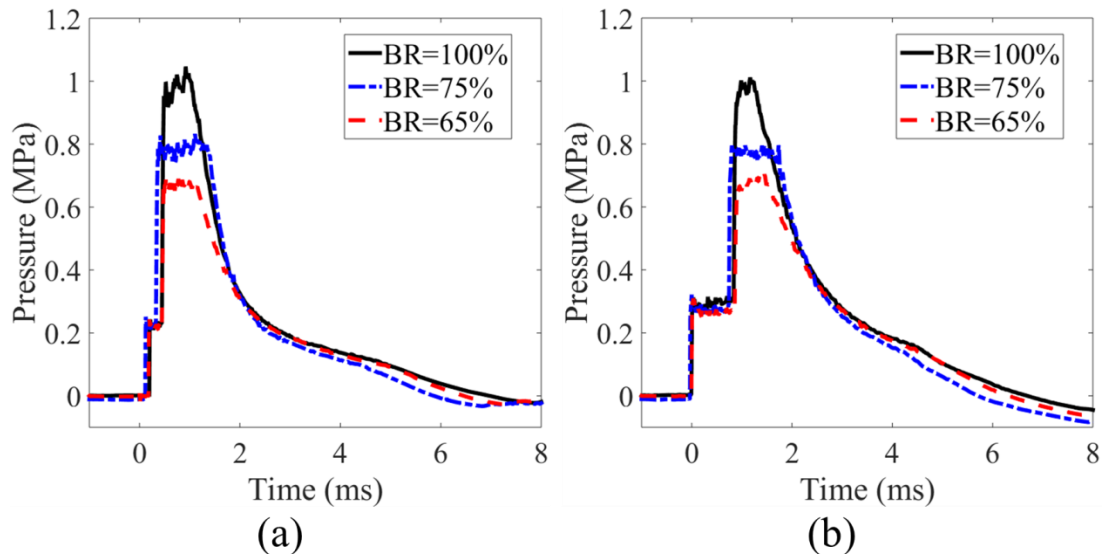
Fig. 9: Recorded reflected pressure profiles (a) 55 mm (b) 175 mm upstream of the specimens having different plate's blockage ratio. In all cases $M_S = 1.76$

3.1.2 Effect of the Properties of the Perforated Plate on the Reflected Pressure Profile

To examine the effects of different perforation sizes and geometries on the reflected pressure history, another set of experiments was conducted using a constant incident shock wave Mach number of $M_S = 1.76$ and perforated plates (4-8) having a

constant blockage ratio of 65%, but having different hydraulic diameter (D_h). In this study, plates 4-6 were tested to assess the perforation sizes, while plates 6-8 were examined to understand the influence of perforation shapes. Recall that plate's (4, 5, and 6) had circular perforations with net opening perimeter of 223 mm (D_h = 7.1 mm), 264 mm (D_h = 6.0 mm), and 317 mm (D_h = 5.0 mm) respectively. Whereas, plate's (7 and 8) had square and triangular perforations with a net opening perimeter of 357 mm (D_h = 4.5 mm) and 407 mm (D_h = 4.0 mm) respectively.

3.1.2.1 Size of Perforations Effects

The upstream pressure histories that were measured by the pressure transducers (1, 2 and 3) are shown in Fig. 10a-c respectively. The main observations that can be made from these pressure profiles are the following: (i) The results showed that perforation sizes on the plate have no influence on the reflected shock wave Mach number. For different perforation sizes on the plate, the shock wave was reflected with an average velocity of 300 m/s, translating to approximate Mach number of 0.88. The reflected shock waves had a short rise time of about 0.02 ms and showed an exponential decay period of approximately 1.5 ms. The time period of the reflected pressure was about of 6.0 ms for different plate's hydraulic diameter. (ii) The initial peak reflected pressures were the same for different plate's hydraulic diameter, and are a function of only the blockage ratio of the plate. (iii) Afterwards, a pressure build-up region on the perforated plates was observed up to t = 0.85 ms due to the high resistance to the fluid flow.

Figure 10a shows the direct comparison of the pressure buildup region for plates (4-6) at sensor #1. The resulted pressure build-up region for plate's 4, 5 and 6

increased to 0.80 MPa, 0.75 MPa, and 0.71 MPa with respect to the level of the initial

peak reflected pressure of 0.70 MPa. This indicates that the perforated plates, which

have a smaller net hole perimeter (or larger plate's hydraulic diameter) resulted in an

increase in the pressure build-up region with respect to the level of the initial peak

reflected pressure (0.70 MPa).

(a)

(b)

(c)

Fig. 10: Recorded pressure profiles for different perforation sizes (a) 15 mm, (b) 55 mm, and (c) 175 mm upstream of the specimens. Samples with a constant blockage ratio of 65%, but having different hydraulic diameter (D_h). In all cases $M_S = 1.76$

For further distance at the sensor located 55 mm away from the perforated specimens, the existence of the pressure buildup region was still significant as shown in Fig. 10b. For large distances upstream of the perforated plates (175 mm away), the specific perforation sizes of the plates had no influence on the build-up region (vanished) as shown in Fig. 10c. This shows that the effect of different perforation sizes is highly localized, and that effect vanishes at greater distances upstream.

Fig. 11: The areal impulse for different perforation sizes (a) 15 mm, (b) 55 mm, and (c) 175 mm upstream of the specimens. Samples with a constant blockage ratio of 65%, but having different hydraulic diameter (D_h). In all cases $M_S = 1.76$

These results can be better seen as represented by the areal impulse imparted to the plates as shown by Fig. 11. For the sensor located 15 mm away from the perforated specimens (see Fig. 11a), perforated plates (4, 5, and 6) obtained a maximum areal impulse of 1500, 1434, and 1373 Pa.s from the shock loading respectively. The results indicated that the plate with smaller circular perforations (plate 6) showed 9% decrease in the maximum areal impulse as compared to plate 4 which had larger circular perforations. Therefore, there was no doubt that, the net hole perimeter (or the hydraulic diameter) of the perforated plates had an effective influence on the reflected pressure build-up region.

3.1.2.2 Shape of Perforations Effects

The perforated plate (6, 7, and 8) which has circular, square, and triangular perforations were examined to understand the influence of perforation shapes on the reflected pressure profiles. Recall that perforated plate's (6, 7, and 8) had net opening perimeters of 317 mm (D_h = 5.0 mm), 357 mm (D_h = 4.5 mm), and 407 mm (D_h = 4.0 mm) respectively.

The upstream pressure histories that were measured by the pressure transducers (1, 2 and 3) are shown in Fig. 12a-c respectively. The main observations that can be made from these pressure profiles are the following: (i) The results indicated that perforation shapes on the plate have no influence on the reflected shock wave Mach number. For different perforation geometries on the plate, the shock wave was reflected with an average velocity of 300 m/s, translating to approximate Mach number of 0.88. The reflected shock waves had a short rise time of about 0.02 ms and showed an exponential decay period of approximately 1.5 ms. The time period of the

97

reflected pressure was that of about 6.0 ms for different perforation shapes on the plate. (ii) The initial peak reflected pressures were the same for different perforation shapes on the plate, and are a function of only the blockage ratio of the plate. (iii) Afterwards, a pressure build-up region on the perforated plates was observed up to $t = 0.85$ ms due to the high resistance to the fluid flow.

Figure 12a shows the direct comparison of the pressure buildup region for plates (6-8) at sensor #1. The resulted pressure build-up region for plate 6 increased to 0.71 MPa with respect to the level of the initial peak reflected pressure of 0.70 MPa. While, plates (7 and 8) showed a decrease in the pressure build-up region to 0.65 MPa and 0.54 MPa with respect to the level of the initial peak reflected pressure of 0.70 MPa. This indicates that the perforated plates, which have a larger net hole perimeter (or smaller plate's hydraulic diameter) results in decreases of pressure build-up region with respect to the level of the initial peak reflected pressure (0.70 MPa). For further distance at sensor located 55 mm away from the perforated specimens, the existence of the pressure buildup region was still significant as shown in Fig. 12b. For large distances upstream of the perforated plates (175 mm away), the specific perforation shapes of the plates had no influence on the build-up region (vanished) as shown in Fig. 12c. This shows that the effect of different perforation shapes was highly localized, and that effect vanishes at greater distances upstream.
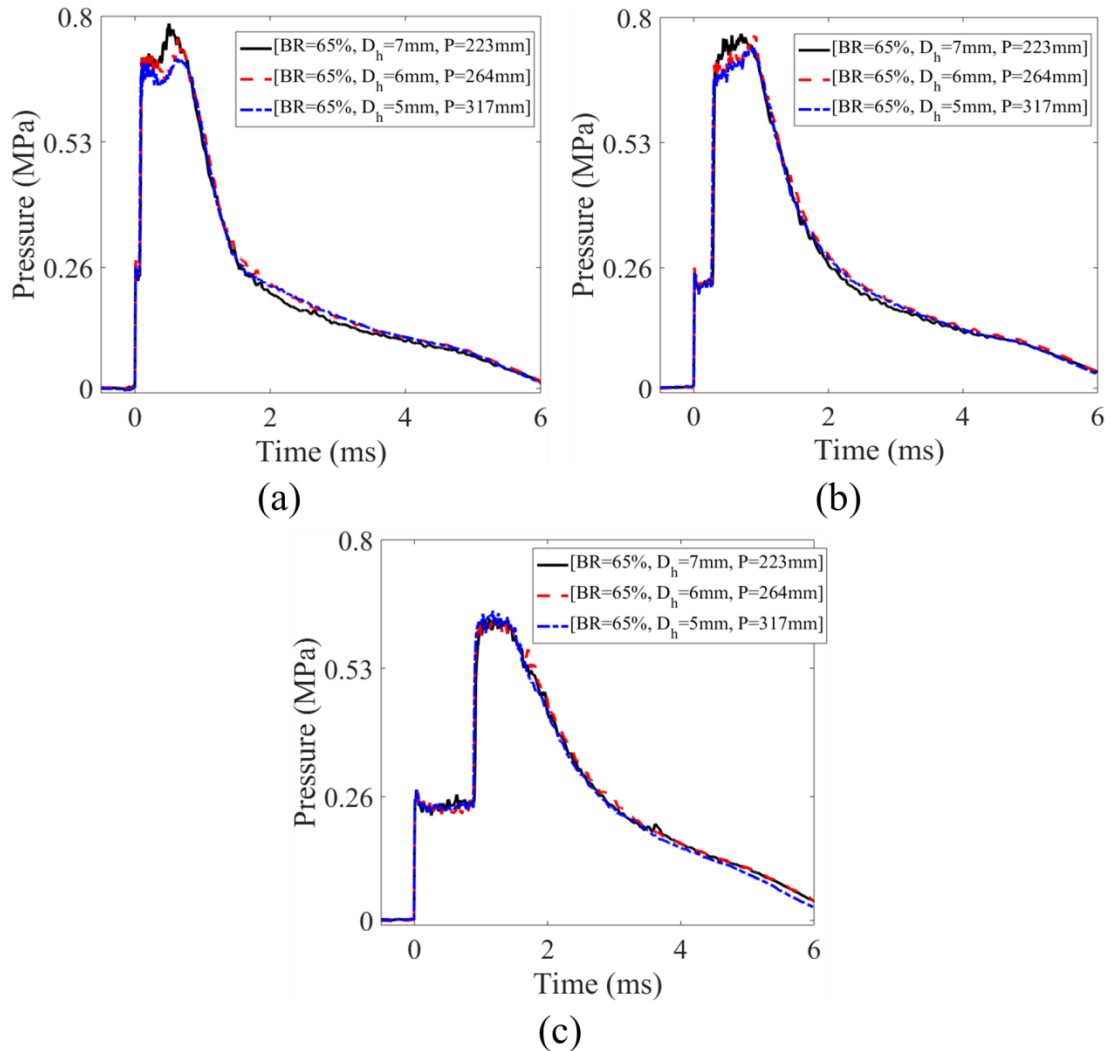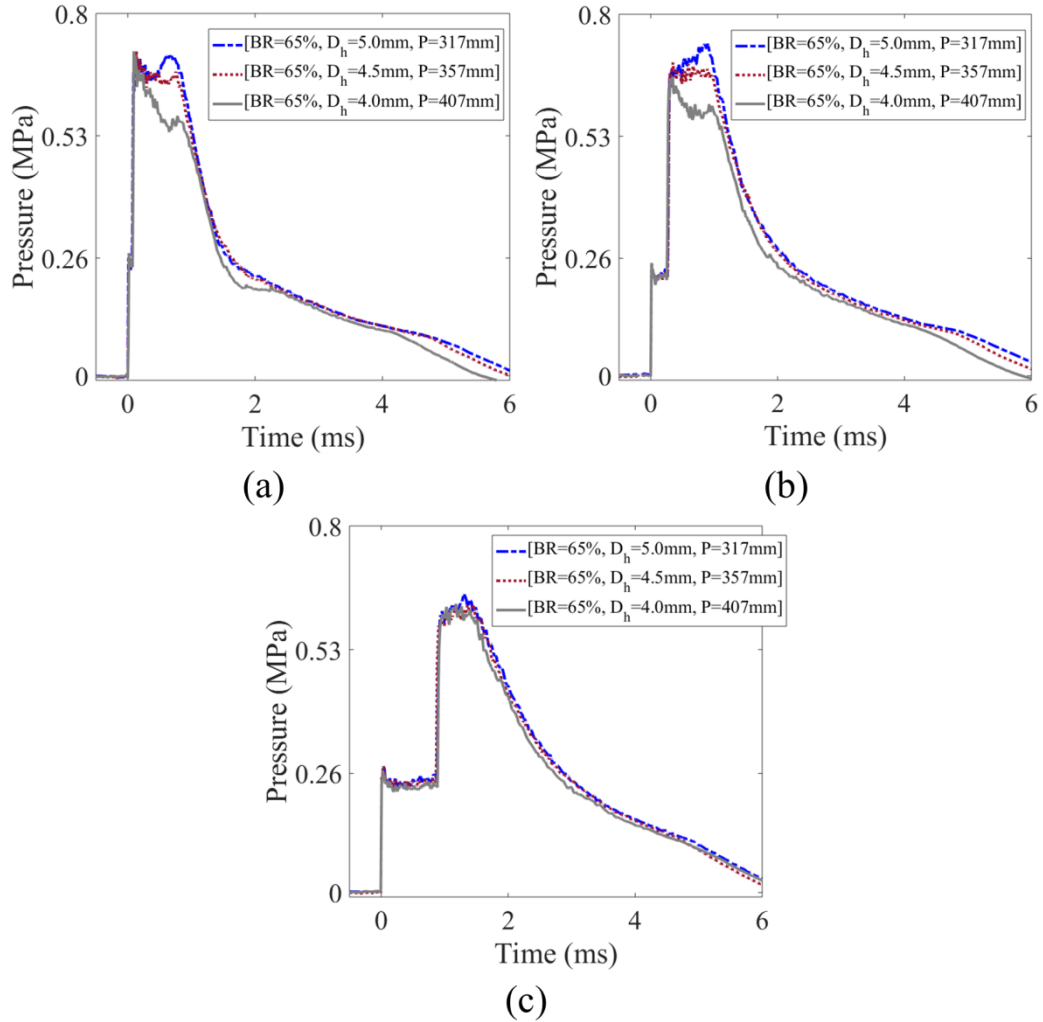
Fig. 12: Recorded pressure profiles for different perforation shapes (a) 15 mm, (b) 55 mm, and (c) 175 mm upstream of the specimens. Samples with a constant blockage ratio of 65%, but having different hydraulic diameter (D_h). In all cases $M_S = 1.76$

These results can be better seen as represented by the areal impulse imparted to the plates as shown by Fig. 13. For the sensor located 15 mm away from the perforated specimens (see Fig. 13a), perforated plate (6, 7, and 8) obtained a maximum areal impulse of 1373, 1289, and 1199 Pa.s from the shock loading respectively. The results indicated that the plate with triangular perforations (plate 8) showed a 13% decrease in the maximum areal impulse as compared to plate 6 which has circular perforations. Therefore, there is no doubt that, the net hole perimeter (or

the hydraulic diameter) of the perforated plates has a strong impact on the pressure build-up region.
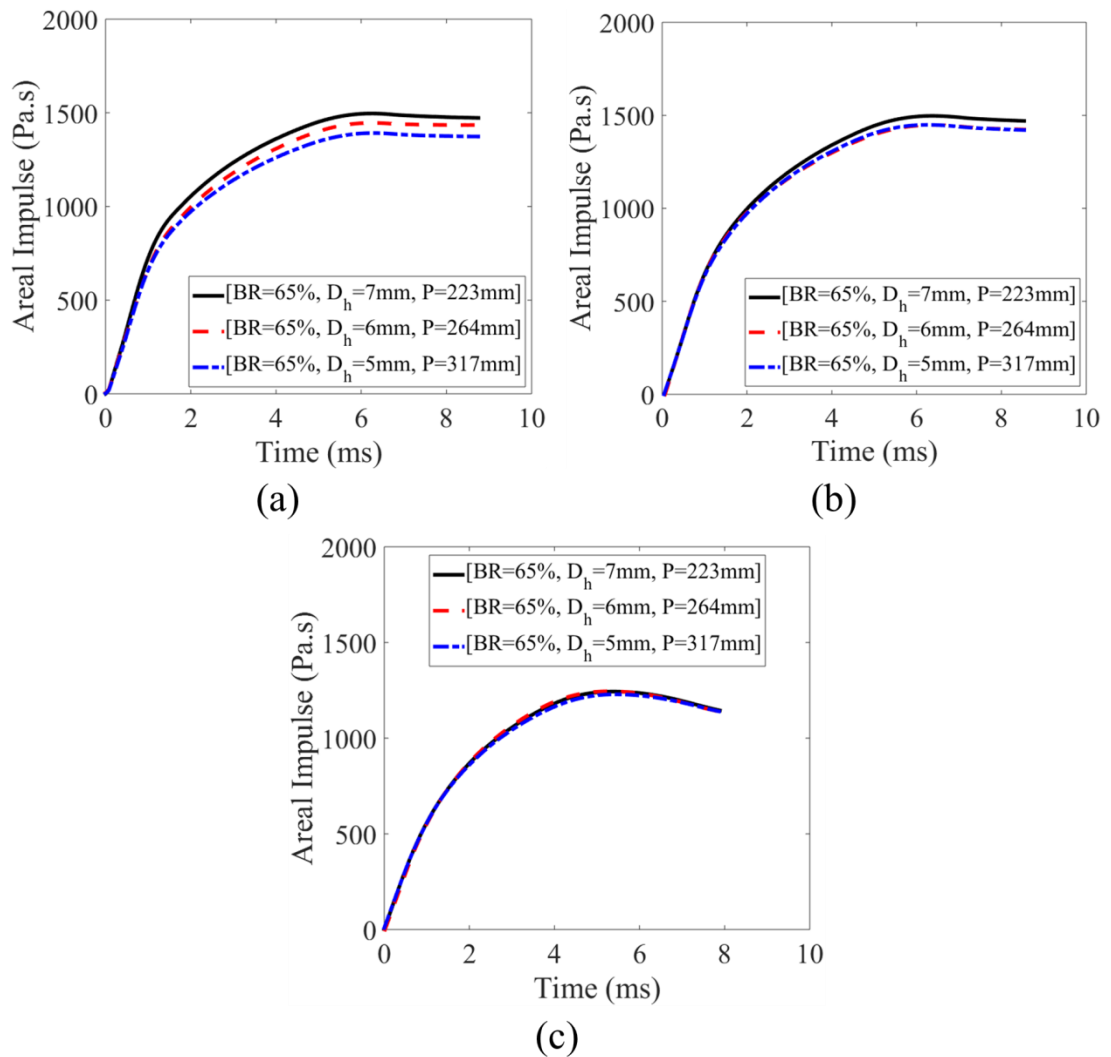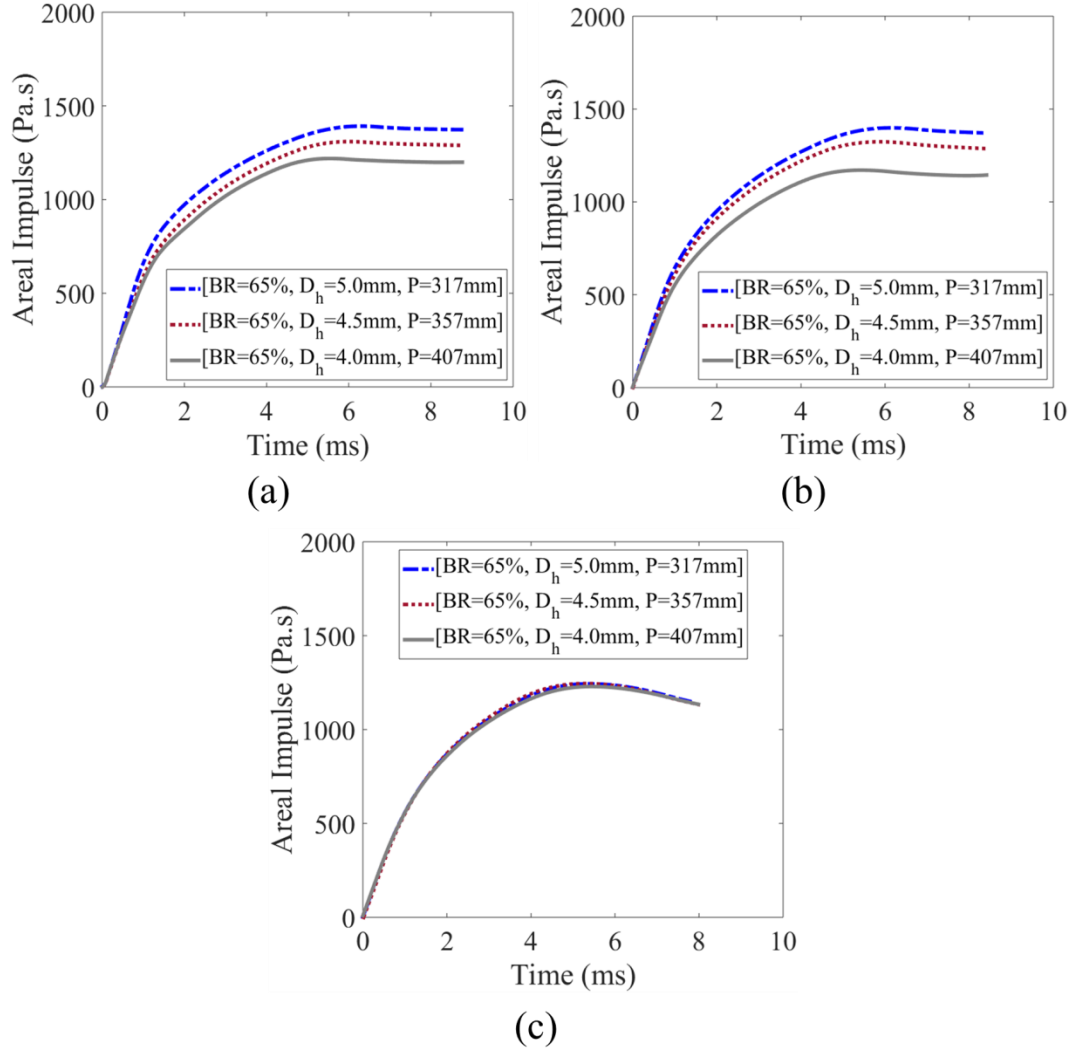

Fig. 13: The areal impulse for different perforation shapes (a) 15 mm, (b) 55 mm, and (c) 175 mm upstream of the specimens. Samples with a constant blockage ratio of 65%, but having different hydraulic diameter (D_h). In all cases $M_S = 1.76$

3.1.3 Motion Response of Perforated Plates

The high speed side-view images during the fluid structure interaction time of plates (1, 2, and 8), which have different blockage ratio are shown in Fig. 14. The shock wave is propagating from the right side of the image to the left side. Time t= 0

ms corresponds to the beginning of the event where the shock wave impinged on the plates and the final image for each experiment represents the plate's motion at t= 0.6 ms. Since the compressibility of the gas only has a significant effect on the pressure profile at the beginning of the shock wave loading process [12]. The fluid-structure interaction process was almost over by the time of (t= 0.6 ms) because the gas pressure has dropped to about 40% of its peak value (see Fig. 8a). After this time, most of the load on the plates comes from the wind (movement of the gas particles) behind the shock wave front.
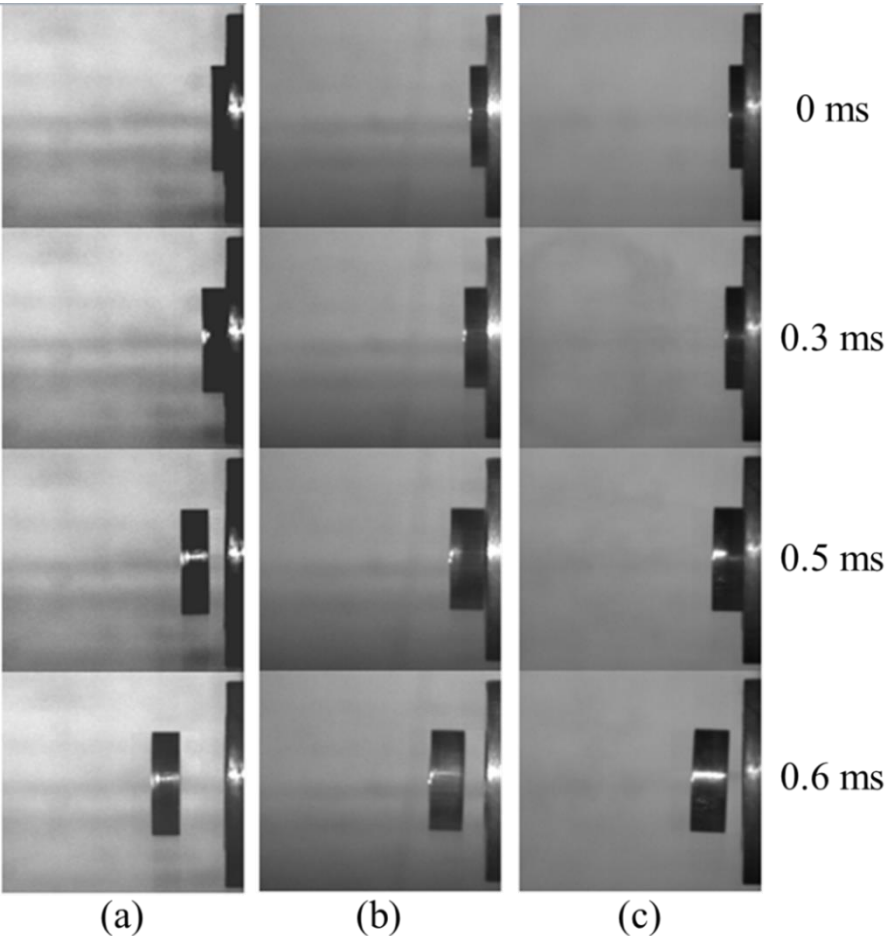
Fig. 14: High-speed side-view images of different plate's blockage ratio (a) BR=100%, (b) BR=75%, and (c) BR=65% during the fluid structure interaction time. In all cases $M_S = 1.76$

The velocity and kinetic energy histories of plates (1, 2, and 8) were determined by the method described in (Section 2.2.1) under a shock wave loading with a peak incident pressure of 0.27 MPa, are plotted in Fig. 15a, b. Recall that the areal density of the targets was 38.0 kg/m^2. At t= 0.6 ms, the solid plate with 100% blockage ratio showed a velocity of approximately 23.0 m/s and a corresponding kinetic energy of 7.5 J. Whereas, perforated plates which had 75% and 65% blockage ratio had velocities of about 13.0 m/s and 9.0 m/s and corresponding kinetic energies of 2.4 J and 1.2 J respectively. It was clear that when the blockage ratio of the plate was decreased from 100% to 65%, the plate's velocity and kinetic energy decreased by approximately 61% and 84% respectively.
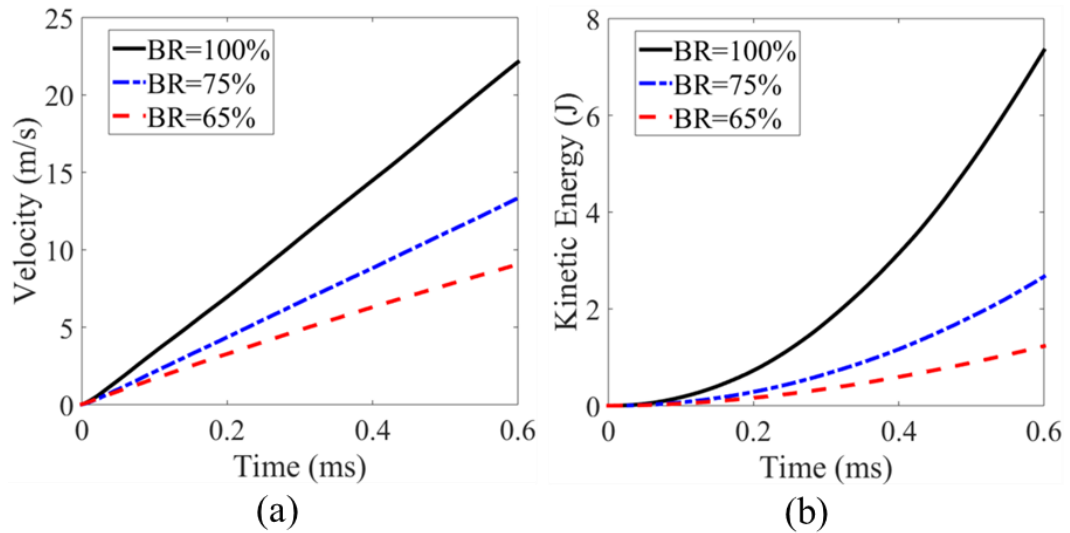
Fig. 15: (a) Velocity and (b) kinetic energy histories of different plate's blockage ratio

Comparison of the momentum of the plates and the impulse applied on the plates for the same peak incident shock pressure are shown in Fig. 16. The momentum of the plates obtained by evaluating the velocity profile and the areal density of the plate (see Eq. 1), and the impulse of the reflected pressure were obtained by

integrating the pressure-time data, which have been shown previously by Fig. 8a. The momentum of the plates agrees with the impulse of the reflected pressure very well for each experiment, verifying that the momentum was conserved during the loading process.
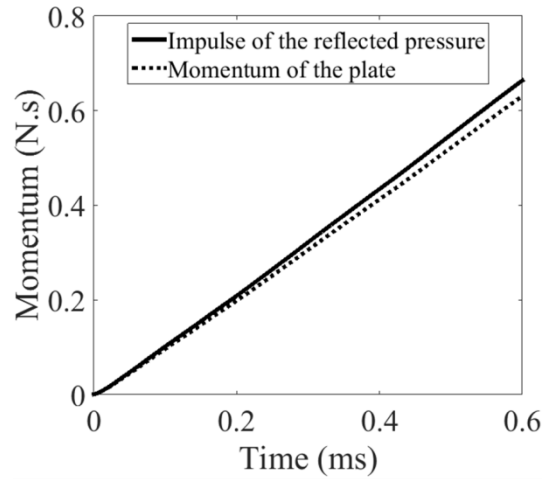
(a) Plate 1 (BR=100 %)
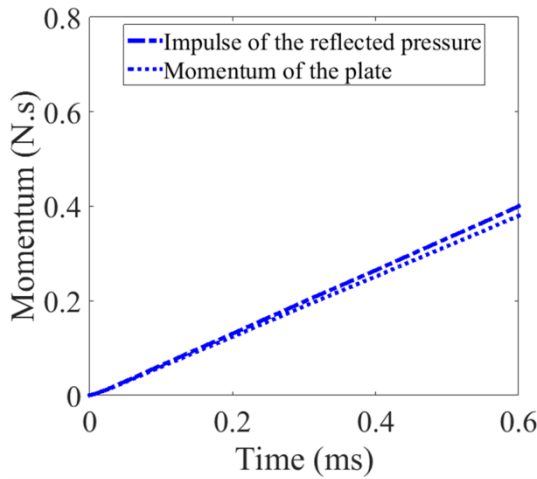
(b) Plate 3 (BR=75 %)
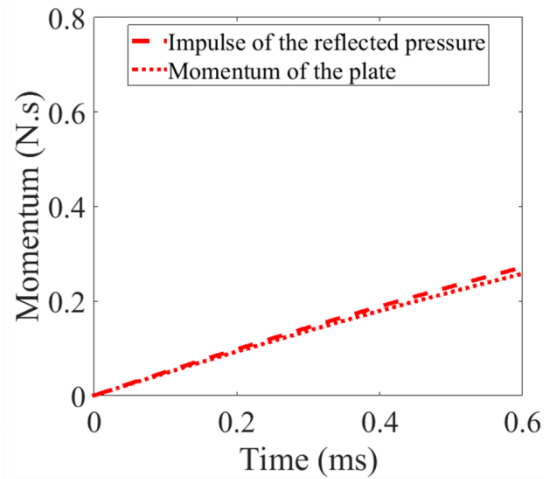
(c) Plate 6 (BR=75 %)

Fig. 16: Comparison of the momentum of different plate's blockage ratio and the impulse of the reflected pressure applied on the plates during the loading process

At t= 0.6 ms, the solid plate with 100% blockage ratio showed a momentum of approximately 0.62 N.s, whereas perforated plates, which had75% and 65% blockage ratio had momentum of about 0.40 N.s and 0.25 N.s respectively. The results showed that when the blockage ratio of the plate decreased from 100% to 65%, the plate's momentum decreased by approximately 60% during the fluid-structure interaction process.

The effect of perforation sizes and geometries on the plate's motion is shown by Fig. 17. The perforated plates (4-8), which have a constant blockage ratio of 65%, but having different hydraulic diameter (changing from 7 mm to 4 mm), showed a velocity of approximately 9.0 m/s and a corresponding kinetic energy of about 1.2 J. The results indicated that the hydraulic diameter or the net perforation perimeter had no influence on the plate's velocity and kinetic energy profiles during the fluid-structure interaction process.
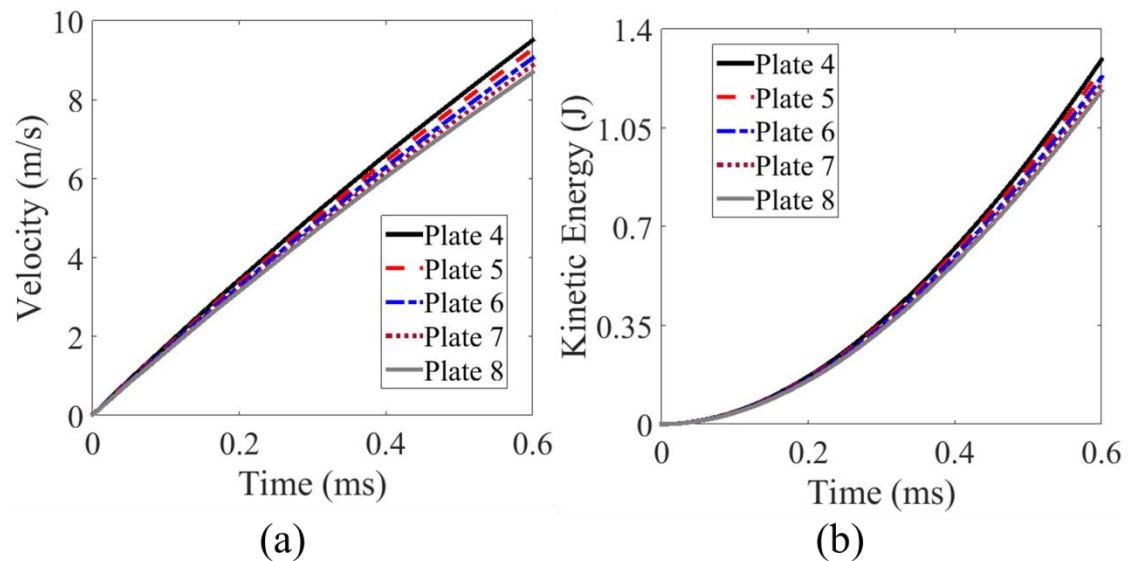
Fig. 17: (a) Velocity and (b) kinetic energy histories of different plate's perforation sizes and geometries

3.2 Experiments with Clamped Boundary Conditions

Inside a straight conduit, it has been known that when a planar shock wave collides with a perforated obstacle two processes take place at once. One part of the shock wave was reflected head-on from the perforated plate and the other part was transmitted through the open area of the plate. The first part referred to shock wave reflection from obstacle and the second part as shock wave diffraction through the perforation generating a non-steady flow behind it [1]. A set of experiments were conducted with clamped boundary conditions to evaluate the reflected and transmitted pressure pulses of the same samples of porous medium (Plates 4-8) using the modified shock tube described in (Section 2.2.2). The effect of the incident shock wave Mach number on the pressure history was also studied. Recall that, a total of four pressure transducers were used to measure the induced pressure histories. The first two pressure sensors (CH1, CH2) were used to investigate the "upstream flow" of both incoming and reflected waves, and the other two pressure transducers (CH3, CH4) were used to measure the "downstream flow" of the transmitted waves as they pass through the barrier.

3.2.1 Effects of Perforation Sizes and shapes

The pressure traces upstream and downstream of the perforated plates (4-8) are shown by Figs. 18 and 19 respectively at a constant incident shock wave Mach number of 1.76. Figure 20 shows the transmitted pressure profiles for further distance downstream from the perforated plates. The main observation from these pressure profiles was drawn in detail in the following sections. For better understanding, the results were also represented by the areal impulse.

3.2.1.1 Reflected pressure Profiles

The generated shock wave had an average incident peak pressure of approximately 0.3 MPa and an average reflected peak pressure of about 0.75 MPa (see Fig. 18). The shock wave traveled inside the muzzle with an incident average velocity of 600 m/s and was reflected with an average velocity of 300 m/s. In this case, the generated shock wave had an incident Mach number $M_S = 1.76$ and was reflected with an approximate Mach number of $M_R = 0.88$. The reflected shock waves had a short rise time of about 0.02 ms and showed an exponential decay period of approximately 8.0 ms.

Fig. 18: Recorded reflected pressure profiles for (a) plates 4-6, (b) plates 6-8, and (c) the calculated areal impulse for plates 4-8. In all cases $M_S = 1.76$

The initial reflected peak pressures were the same (0.75 MPa) for different plate's perforation sizes and shapes, and were a function of only the blockage ratio of the plate. Afterwards, a pressure build-up region on the perforated plates was observed up to t = 1.2 ms due to the high resistance to the fluid flow (see Fig. 18a, b). The resulted pressure build-up region for plates (4, 5, 6, 7, and 8) increased to 0.92 MPa, 0.88 MPa, 0.85 MPa, 0.83 MPa, and 0.80 MPa with respect to the level of the initial peak reflected pressure of 0.75 MPa. This indicated that the perforated plates, which have a smaller net hole perimeter (or larger plate's hydraulic diameter) resulted in increases in the pressure build-up region with respect to the level of the initial peak reflected pressure. These results can be better seen represented by the areal impulse imparted to the plates (4-8) as shown by Fig. 18c. When the plate's hydraulic diameter was decreased from 7.0 mm (plate 4) to 4.0 mm (plate 8), the maximum areal impulse imparted to the plate decreased by approximately 12% (4400 Pa.s to 3900 Pa.s). Therefore, there was no doubt that the net hole perimeter (or the hydraulic diameter) of the perforated plates has an effective influence on the pressure build-up region.

3.2.1.2 Transmitted Pressure Profiles

The transmitted shock wave traveled with an average velocity of 454 m/s, translating to approximate Mach number of 1.3. Recall that the shock wave had an incident Mach number 1.76. This means that when the shock wave passed through the barriers, the Mach number of the generated shock wave was reduced (mitigated) by 26% (from $M_S = 1.76$ to $M_T = 1.3$).

When the shock wave passes through the barriers, a transmitted peak pressure of approximately 0.2 MPa was observed (see Fig.19a, b). Recall that the generated

shock wave had an incident peak pressure of 0.3 MPa. This means that as the transmitted wave exits the perforated plate, its strength reduces compared to the initial incident shock wave. In this case, the shock wave was reduced (mitigated) by 33%. It should be noted that the data of the blank test (no plate or BR=0%) was presented as a dotted black line in Fig. 19a, b for purposes of comparison with experimental values. Figure 19a, b contains information about the dynamics of the transmitted shock wave from the plates (4-6) at CH3. The recorded pressure histories show that there was an initial unsteady spike of 0.2 MPa with a short rise time of about 0.02 ms followed by a relatively small quasi-steady pressure region of about 0.8 ms. This was consistent with previous findings of Ben-Dor et al who reported that such a pressure trace was typical to a jet dominated flow, where the flow in this region was nonhomogeneous, non-isotropic with maximum production of turbulent kinetic energy due to the jets and the wakes produced by the perforated plate [1].

These results can be better seen as represented by the areal impulse transmitted from (4-8) as shown by Fig. 19c. For the sensor located 21 mm downstream from the specimens, plates (4, 5, 6, 7, and 8) obtained a maximum transmitted impulse of 50, 75, 96, 105, and 112 Pa.s from the shock loading respectively. The results indicated that plate 4 with larger circular perforations (D_h=7mm) showed a 48% decrease in the maximum transmitted areal impulse as compared to plate 6, which had smaller circular perforations (D_h=5mm). The results also showed that plate 6 with circular perforations (D_h=5mm) showed a 14% decrease in the maximum transmitted areal impulse as compared to plate 8, which had triangular perforations (D_h=4mm). Therefore, there is

no doubt that the net hole perimeter (or the hydraulic diameter) of the perforated plates had a strong impact on the transmitted shock wave.
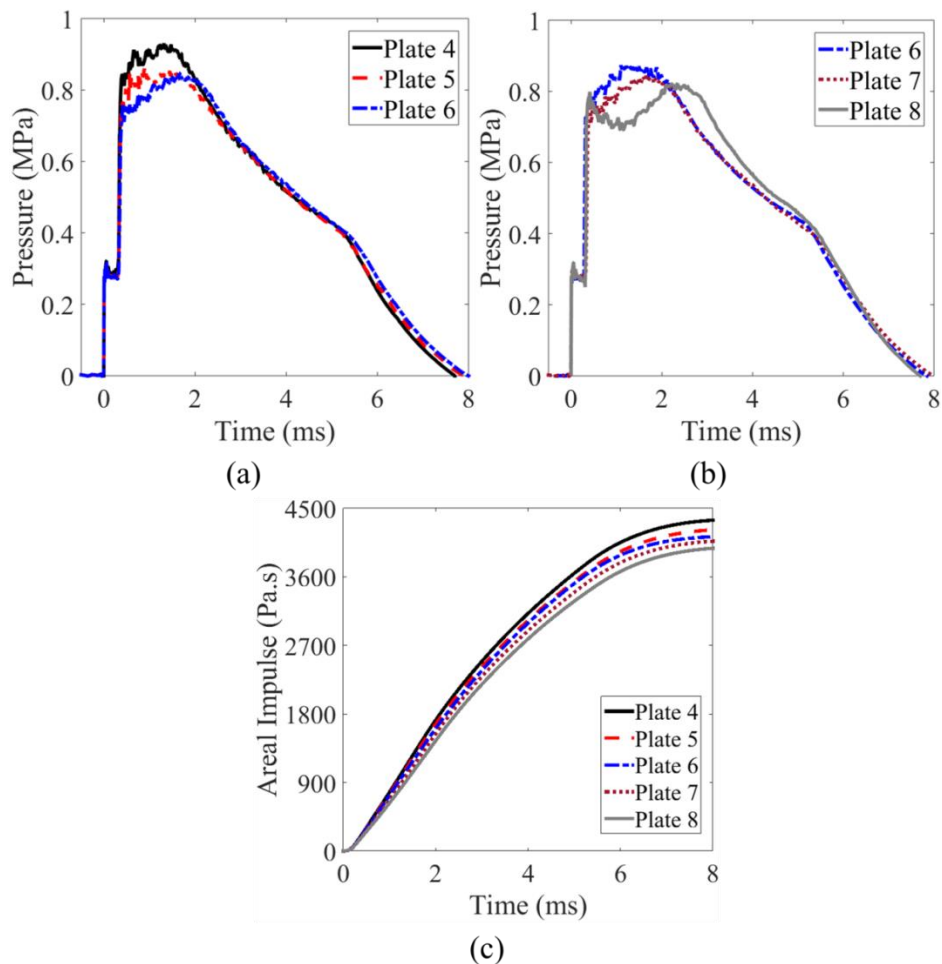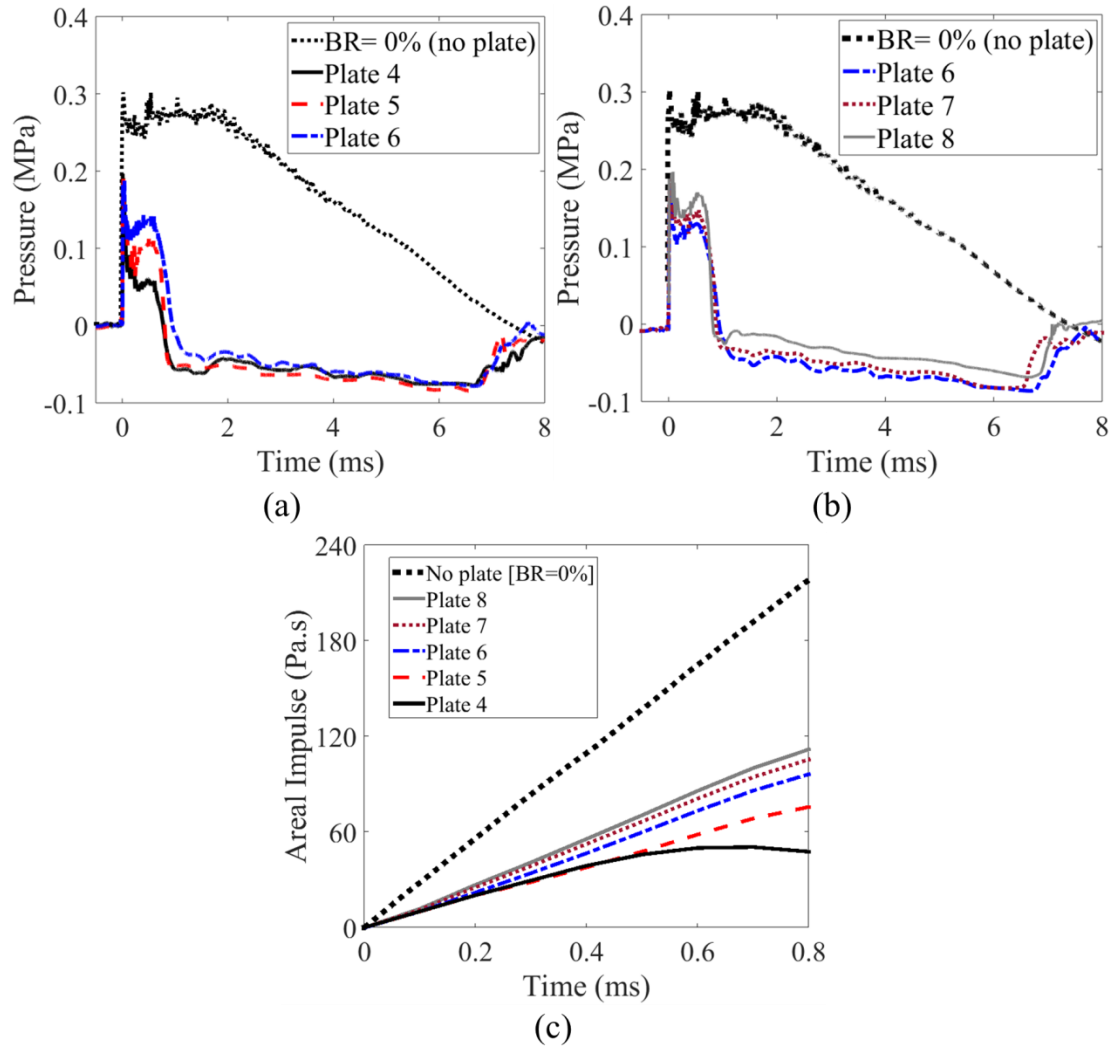

Fig. 19: Recorded transmitted pressure profiles for (a) plates 4-6, (b) plates 6-8, and (c) the calculated transmitted impulse for plates 4-8. In all cases M_S = 1.76. Note: the data of blank test (no plate) is added as a dotted black line for purposes of comparison with experimental values

In comparison with the transmitted shock waves measured at CH4, Fig. 20 indicates that the transmitted shock wave had the same initial peak pressure of 0.2 MPa, but it showed a longer exponential decay period of approximately 1.5 ms. This

means that for further distance at sensor (CH4) located 73 mm downstream from the perforated plates, the transient pressure showed a tendency to approach steady state and to reach equilibrium amplitude. This was consistent with previous findings of Ben-Dor et al who reported that for larger distances downstream the specific shape of the perforated plate had practically no influence on the recorded pressures as long as the porosity is kept at a constant value [1].

(a) Perforation sizes and shapes effect at CH3

(b) Perforation sizes and shapes effect at CH4
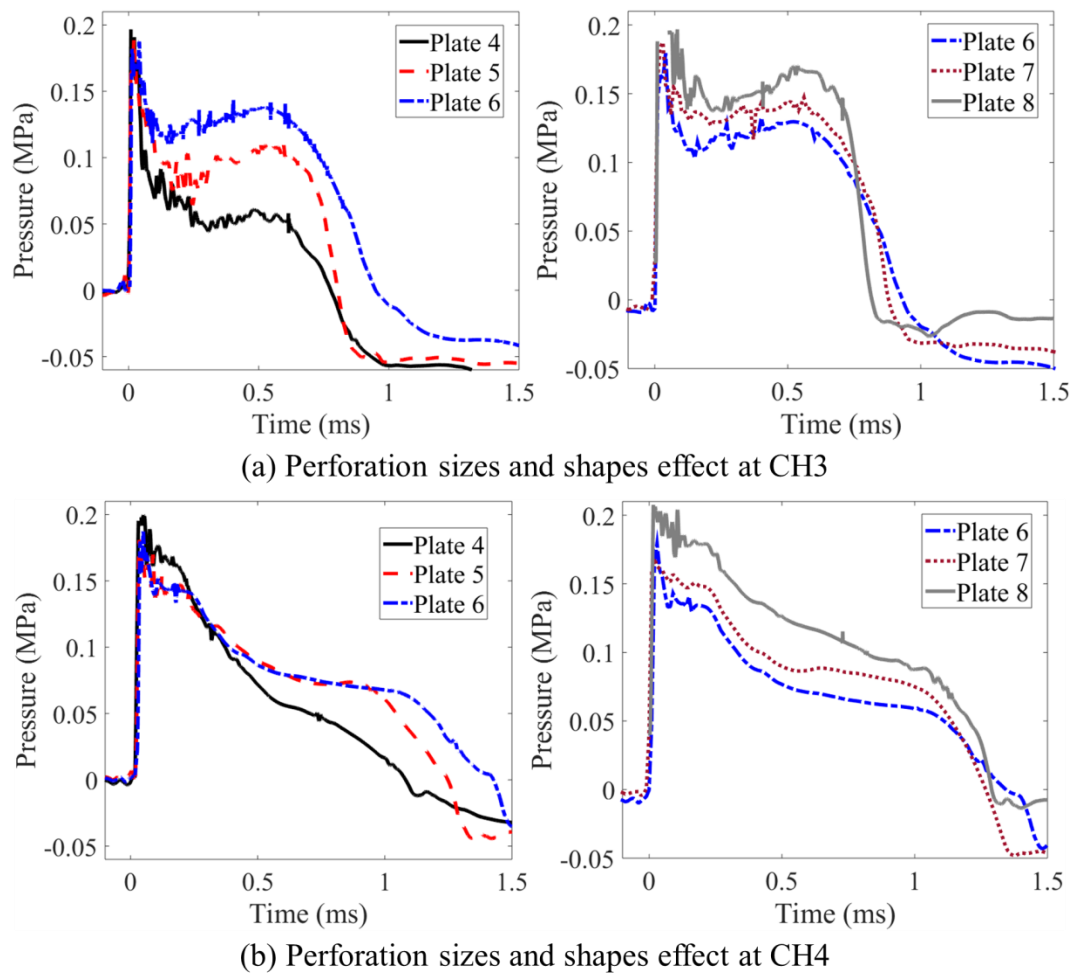
Fig. 20: Transmitted pressure profiles for different perforation sizes and shapes (a) 21 mm and (b) 73 mm downstream of the perforated plates.

3.2.2 Effect of Incident Shock Wave Mach Number

In order to study the effect of the incident shock wave Mach number on the pressure history, experiments have been carried out at three shock Mach numbers, i.e., 1.76, 2.0, and 2.4. Figure 21a shows the incident pressure profiles with different incident peak pressures of 0.3, 0.41, and 0.55 MPa. The reflected pressure profiles measured for plate 1 (BR=100%) at different incident shock levels are shown in Fig. 21b. These experiments (Fig. 21) were used as a baseline for the performance of other specimens as a function of incident Mach number (or incident pressure). The experiment for plate 6 (BR=65%) was taken as a typical example to explain the effect of the incident shock wave Mach number on the reflected and transmitted pressure history. Figure 22 shows the reflected pressure profiles at CH2 for different incident shock levels and Figure 23 presents the transmitted pressure profiles at CH3.
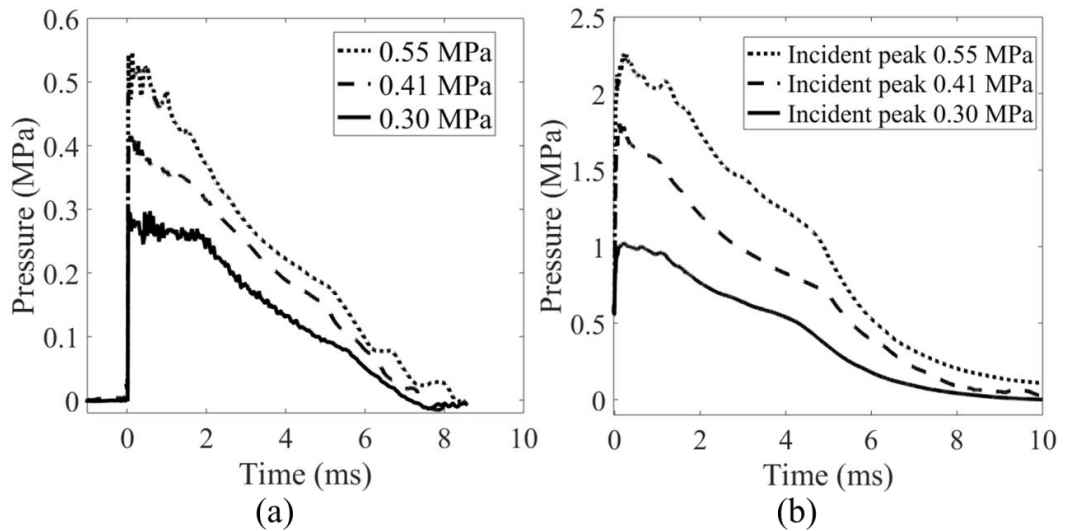
Fig. 21: (a) Incident pressure profiles with different incident peak pressure and (b) reflected pressure profiles measured for plate 1 (BR=100%) at different incident shock levels

Once the incident shock wave reflected head-on from the front face of the porous sample (plate 6) the pressure acting on the front face of the sample reached its maximum peak values, which for the above mentioned Mach numbers, 1.76, 2.0, and 2.4 were 0.75, 1.5, and 1.9 MPa, respectively (see Fig. 22a). For all Mach numbers examined, the reflected shock waves showed an exponential decay period of approximately 8.0 ms. The influence of varying the incident shock wave Mach number on the reflected pressure profile was better represented by the areal impulse imparted to the plate (Fig. 22b). It was seen that an increase in the incident shock wave Mach number led to a higher impulse imparted to the plate. However, this effect does not scale linearly with the incident shock wave Mach number. In other words, when the incident shock wave Mach number initially increased by 14% (from 1.76 to 2.0), there was an extremely rapid increase in the areal impulse percentage of about 40% (from 4000 Pa.s to 5600 Pa.s). Whereas, this impulse effect continually becomes shallower of about 16 % when the incident shock wave Mach number increased by another 20% (from 2.0 to 2.4).
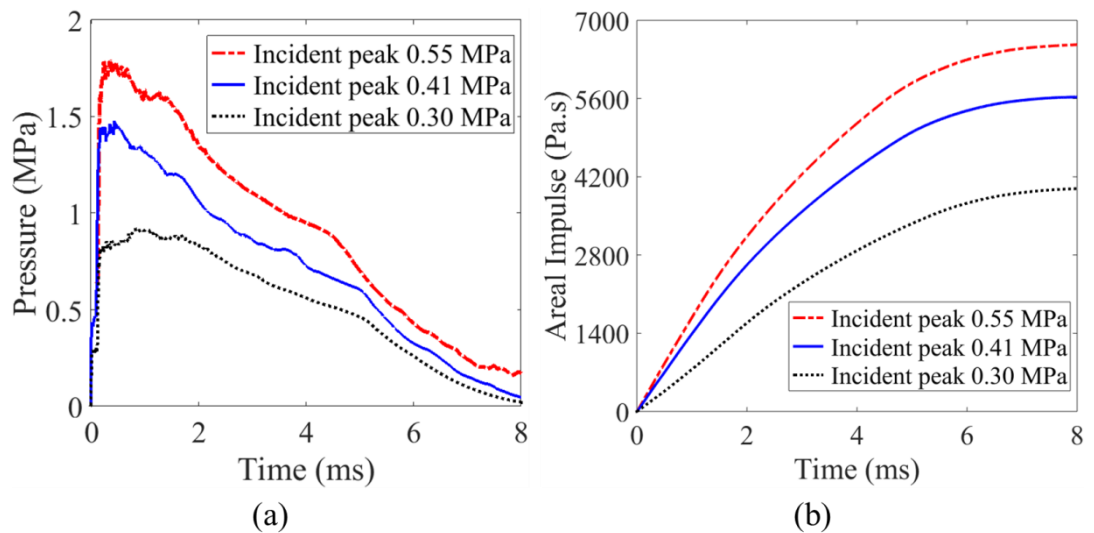
Fig. 22: (a) Recorded reflected pressure profiles and (b) their calculated areal impulse at different incident shock levels measured for plate 6

As the shock wave passed through the barrier with different incident shock wave Mach numbers of 1.76, 2.0, and 2.4, transmitted peak pressures of approximately 0.20, 0.30, and 0.36 MPa were observed respectively (see Fig. 23a). For incident Mach numbers of 1.76, 2.0, and 2.4, the transmitted shock waves showed different exponential decay periods of approximately 0.8, 0.6, and 0.3 ms respectively. In comparison to the incident shock waves, which showed incident peak pressures (0.3, 0.41, and 0.55 MPa) and had an exponential decay period of approximately 8.0 ms (see Fig. 21a), the strength of the generated shock was reduced due to its passage through the porous media. In $M_S=1.76$ case, the incident peak pressure of the shock wave was reduced by 33%, while it was reduced by 27%, and 36% for $M_S=2.0$, and 2.4 respectively. The results indicated that the strength of the resulting waves increased linearly with increasing shock Mach number.
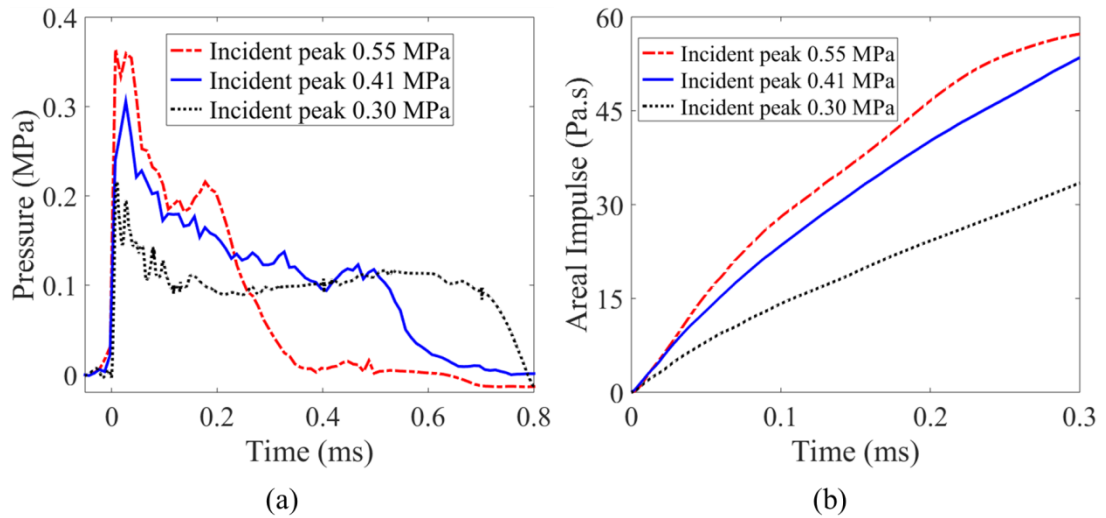
Fig. 23: (a) Recorded transmitted pressure profiles and (b) their calculated areal impulse at different incident shock levels measured for plate 6

The influence of varying the incident shock wave Mach number on the transmitted pressure profile was better represented by the areal impulse (Fig. 23b). It

was seen that an increase in the incident shock wave Mach number led to a higher impulse transmitted through the plate up to t= 0.3 ms. However, this effect does not scale linearly with the incident shock wave Mach number. In other words, when the incident shock wave Mach number initially increased by 14% (from 1.76 to 2.0), there was an extremely rapid increase in the transmitted impulse percentage of about 64% (from 33 Pa.s to 54 Pa.s). Whereas, this impulse effect continually became shallower of about 6 % when the incident shock wave Mach number increased by another 20% (from 2.0 to 2.4).

3.3 Effect of Boundary Conditions

In order to understand the effect of boundary conditions on the reflected shock pressure history, Fig. 24a shows a direct comparison between free standing and rigid boundary conditions for Plate 6. This figure shows the pressure profiles measured by the pressure transducer closest to the front face of the specimens (15 mm away from specimen front face). For different boundary conditions, the incident shock wave traveled inside the muzzle with an average velocity of 600 m/s and was reflected with an average velocity of 300 m/s, translating to approximate Mach numbers of 1.76 and 0.88, respectively. The incoming shock waves had an average incident peak pressure of 0.3 MPa and reflected peak pressures of 0.75 MPa. The reflected shock waves had a short rise time of about 0.02 ms. The reflected shock wave of the freestanding and fixed perforated plate showed an exponential decay period of approximately 1.5 ms, and 6.0 ms respectively. The overall time period of the load acting on the specimen (reflected pressure) changed with boundary condition. The time period of the reflected shock wave of fixed and freestanding perforated plate decreased from 8.0 ms to 6.0 ms

respectively, where the time period is defined as the time at which the pressure became equal to the atmospheric pressure. Figure 24b shows the impulse imparted to plate 6 for freestanding and rigid boundary conditions. The free standing perforated plate obtained a maximum areal impulse of 1373 Pa.s from the shock loading. When the boundary condition changed from free to fixed, the maximum areal impulse imparted to the perforated plate was increased by approximately 194% (1373 Pa.s to 4000 Pa.s).

It can be seen in Fig. 24 that the imparted impulse for the freestanding plate was significantly less than that for the corresponding fixed plate. For a free-standing plate, the impact of a blast wave caused the plate to recede. The receding motion of the plate relieved the pressure experienced by the plate and resulted in a decrease in the impulse transmitted to the plate.
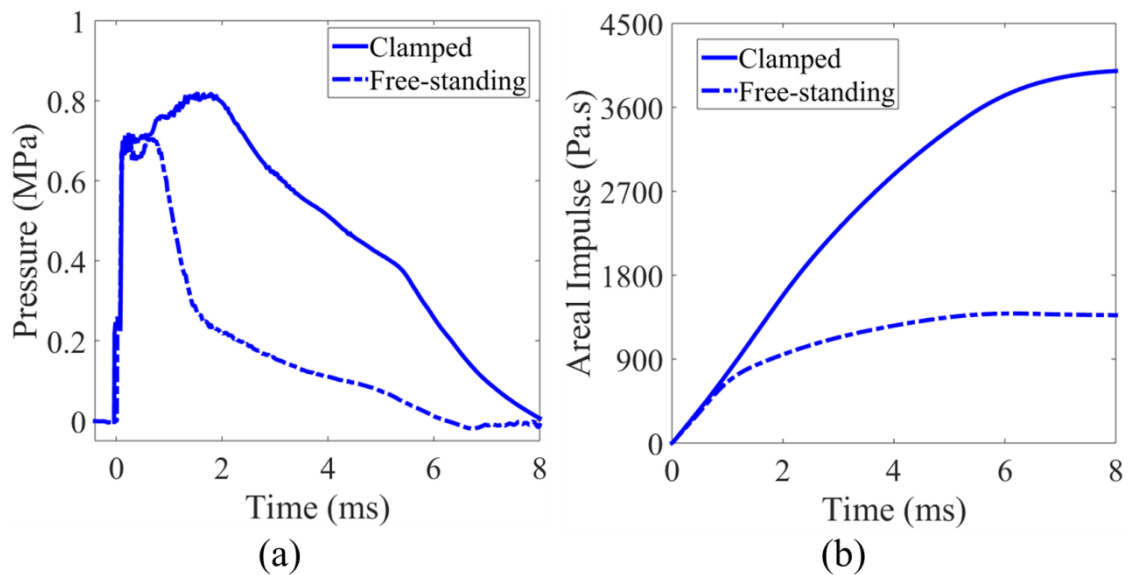
Fig. 24: Direct comparison of the (a) reflected pressure profiles and (b) true duration of imparted areal impulse measured for plate 6 at different boundary conditions. In all cases $M_S=1.76$

4. Conclusions

In the first part of this study, shock wave loading experiments on freestanding perforated plates was conducted to evaluate the reflected pressure pulses and the motion response for all the targets with and without perforations. The second part of this study was on clamping all the targets inside the shock-tube to evaluate the reflected and transmitted pressure pulses for all the targets. Through these experiments, the following major conclusions have been drawn:

- The experimental results showed that as the blockage ratio of the freestanding perforated plate decreased from 100% to 65%, the reflected peak pressure decreased by 26%, the maximum impulse imparted to the perforated plate decreased by 33%.

- During the fluid-structure interaction process, as the blockage ratio of the freestanding perforated plate decreased from 100% to 65%, the plate's momentum, velocity and kinetic energy decreased by approximately 60%, 61%, and 84% respectively. At constant plate's blockage ratio, the results indicate that the hydraulic diameter or the net perforation perimeter had no influence on the plate's velocity and kinetic energy profiles during the fluid-structure interaction process.

- Furthermore, it was determined that the hydraulic diameter of the perforated plates had an effective influence on the reflected and transmitted shock waves at close by regions upstream and downstream. For larger distances upstream and downstream, the specific shape and size of the perforations on the plate

had practically no influence on the recorded pressures as long as the porosity was kept at a constant value.

- An increase in the incident shock wave Mach number led to a higher impulse of the reflected and transmitted shock waves. However, this effect does not scale linearly with the incident shock wave Mach number.

- When the boundary condition changed from free to fixed, the maximum areal impulse imparted to the perforated plate was increased by approximately 194% (1373 Pa.s to 4000 Pa.s).

Acknowledgment

References

[1] Britan, a., Karpov, a. V., Vasilev, E. I., Igra, O., Ben-Dor, G., & Shapiro, E. (2004). Experimental and Numerical Study of Shock Wave Interaction with Perforated Plates. Journal of Fluids Engineering, 126(3), 399

[2] Britan, A., Igra, O., Ben-Dor, G., & Shapiro, H. (2006). Shock wave attenuation by grids and orifice plates. Shock Waves, 16(1), 1–15

[3] Ram, O., & Sadot, O. (2013). A simple constitutive model for predicting the pressure histories developed behind rigid porous media impinged by shock waves. Journal of Fluid Mechanics, 718, 507–523

[4] Ram, O., & Sadot, O. (2015). Analysis of the pressure buildup behind rigid porous media impinged by shock waves in time and frequency domains. Journal of Fluid Mechanics, 779, 842–858

[5] Zhou, X. Q., & Hao, H. (2008). Prediction of airblast loads on structures behind a protective barrier. International Journal of Impact Engineering, 35(5), 363–375

[6] Langdon, G. S., Nurick, G. N., Balden, V. H., & Timmis, R. B. (2008). Perforated plates as passive mitigation systems. Defence Science Journal, 58(2), 238–247

[7] Langdon, G. S., Rossiter, I. B., Balden, V. H., & Nurick, G. N. (2010). Performance of mild steel perforated plates as a blast wave mitigation technique: Experimental and numerical investigation. International Journal of Impact Engineering, 37(10), 1021–1036

[8] Langdon, G. S., Nurick, G. N., & du Plessis, N. J. (2011). The influence of separation distance on the performance of perforated plates as a blast wave shielding technique. Engineering Structures, 33(12), 3537–3545

[9] Al-qananwah, A. K., Koplik, J., Andreopoulos, Y., Al-qananwah, A. K., Koplik, J., & Andreopoulos, Y. (2013). Attenuation of shock waves propagating through nano-structured porous materials. Physics of Fluids, 76102(7)

[10] Wilgeroth, J. M., Nguyen, T.-T. N., & Proud, W. G. (2014). Interaction between blast wave and reticulated foam: assessing the potential for auditory protection systems. Journal of Physics: Conference Series, 500(10), 102005

[11] Igra, O., Falcovitz, J., Houas, L., & Jourdan, G. (2013). Review of methods to attenuate shock/blast waves. Progress in Aerospace Sciences.

[12] Wang, E., Wright, J., & Shukla, A. (2011). Analytical and experimental study on the fluid structure interaction during air blast loading. Journal of Applied Physics, 110(11), 1–12

CHAPTER 5: THE INFLUENCE OF SURFACE ROUGHNESS ON BLAST MITIGATION

by

Emad A. Makki, Murat Yazici and Arun Shukla

Corresponding Author: Emad A. Makki

Dynamic Photo Mechanics Laboratory

Department of Mechanical, Industrial and Systems

Engineering

University of Rhode Island

94 Upper College Road

131 Kirk Applied Engineering Laboratory

Kingston, RI, 02881, USA

Phone: +1-401-874-2283

Email Address: emakki@my.uri.edu

Abstract

An experimental study was conducted to investigate the performance of different surface roughness of 1018 mild low carbon steel panels under blast loading. These experiments were performed to understand the potential use of changing the surface texture in reducing the total work done by the shock load and in improving the overall structural response. Specimens were machined to have three different surface finishes of (0.8, 1.4, and 5.0) μm. The shock tube apparatus was utilized to generate controlled blast loadings. To implement the simplest boundary condition, specimens were simply supported on the backside during experimentation. For each experiment, the incident and reflected shock wave pressure profiles were recorded using pressure transducers located on the muzzle of the shock tube. The real-time deformation of the specimens was recorded using two high-speed cameras. Three-dimensional Digital Image Correlation was used to analyze the high-speed images and compute the full-field deformation, in-plane strains, and velocities during the blast loading event. In addition, another high speed camera was utilized to record the side-view deformation images and this information was used to validate the data obtained from the 3D stereovision DIC technique. The results indicated that the impulse imparted to the plate decreased as the surface roughness (R_a) increased from 0.8 μm to 5.0 μm. Due to this impulse reduction along with high surface roughness, the plates demonstrated a decrease in back face deflection, in-plane strain and out-of-plane velocity.

Keywords: Shock loading • Surface texture • Digital image correlation • High speed photography • Blast mitigation • Deformation energy

1. Introduction

Blast loading events that arise from the detonation of explosives pose a severe threat to the lives of civilians and military personnel alike [1, 2]. Hence, there has been extensive research on how to mitigate blast wave effects. There currently exists a variety of blast and shock-proofing methods that are implemented in a variety of applications including passive mitigation systems. These mitigation techniques leverage four approaches towards blast mitigation, including impedance mismatching, sacrificial cladding, blast deflection as well as blast and shockwave disruption [3]. The employment of plastically deforming metal plates and sandwich structures to absorb energy for impact and blast loading applications are reported widely in literature [4-8]. Extensive studies have been conducted on various core configurations from closed cell, lattice corrugation, pyramidal truss, honeycomb and composite functional graded structures [9-15]. However, these methods often involve complex and costly materials and/or fabrication methods. Thus, it is the aim of this work to investigate the blast mitigation effectiveness of a relatively simple and cost-effective treatment: the application of surface roughness to the face of a normally loaded material.

Prior literature has explored the problem of shock wave interaction on the boundary layer over a rough wall in transonic circular bump geometry. However, shock being normally loaded or impinged onto a rough surface structure (as is typical with an explosive event) has not previously been investigated even though it is of importance in any treatment of shock wave attenuation. According to A. Kumar et al and J. Mendonca et al, shock wave interaction on the boundary layer causes many noticeable features on the local as well as the whole flow field such as flow separation

and reattachment, boundary layer thickening, shock unsteadiness etc. [16, 17]. When the surface roughness is considered as a flow parameter, an added complexity in the physics of transonic flow is integrated [17]. Understanding the fluid structure interaction behavior during blast loading plays a major role in blast mitigation and helps in evaluating the blast performance of structures and consequently benefits in the design of higher blast resistance structures [18].

The blast wave propagation and reflection from structures with various shapes has been widely studied [91-21]. A 2-D numerical model simulating interactions between a blast wave and a V-shaped or a cone-shaped structure was developed by W. Peng et al. [22]. Normal, oblique, and Mach stem reflections are types of reflection when a blast wave impinges on a surface. The Normal reflection occurs when the incident angle is 0°. The angle between the incident shock front and the reflecting surface of a structure is defined as the incident angle [22]. The authors reported that when the incident angle is greater than 40°, Mach stem reflection occurred. The Mach stem reflection resulted in noteworthy decrease of reflected pressure, as well as the transmitted impulse. The influence of Mach stem reflection in reducing blast wave impact decreased with the decrease of blast intensity [22].

To expand on the aforementioned work already conducted in this field which investigates only the effect of surface roughness on transverse shock loading, specimens made of 1018 mild/low carbon steel were manufactured with a variety of surface roughness values and subjected to normal blast loading. Using a shock tube to initiate the shock and DIC techniques to analyze full field deformation, it was determined that blast mitigation improves as surface roughness increases, insofar as

damage to the structure itself is concerned. That is to say, specimens with higher surface roughness values deformed less than specimens with lower surface roughness values when subject to the same loading. Furthermore, pressure sensors were used to obtain the pressure profiles as a function of time at various distances from the specimen. It was found that the reflected peak pressure measured 23 mm from the specimen decreased as surface roughness increased. Peak pressures measured further away from the specimen (183 mm) were determined to be unaffected as surface roughness varied from specimen to specimen.

2. Experimental Setup and Procedures

Shock tube experiments were performed to establish the dynamic behavior of 1018 mild/low carbon steel panels at different surface roughness of (0.8, 1.4, and 5.0) μm. At least three experiments were performed for each case to ensure repeatability.

2.1 Specimen Geometry and Preparation

The material used in this experimental study was 1018 mild/low carbon steel, supplied by McMaster-Carr. In the present study, rectangular plates measuring 2 in (50.8 mm) wide, 8 in (203.2 mm) long and 0.125 in (3.175 mm) thick were used. Alloy 1018 is the most commonly available of cold-rolled steels and has a fine surface roughness of about 0.8 μm.

The geometrical characteristic of a surface is defined by macro-deviations, surface waviness, and micro-irregularities. In the present work, the surface roughness was evaluated by the mean roughness index (R_a) of the micro-irregularities. A pocket surface roughness gage was used to measure the texture of the surface roughness. The

roughness tester profile-meter has an estimate design to check the surface finish with measured values displaced on digital read out in various surface roughness parameters.

Two machining techniques were applied to the front (loaded) side of the panels to obtain higher surface roughness. These machining techniques were the surface grinding and vertical milling. The surface texture obtained from the grinding process and the vertical milling was about 1.4 and 5.0 µm respectively. The average areal density of the specimens was 24.8 kg/m^2. A photograph of the specimen with three different surface finishes is shown by Fig. 1.

Fig. 1: 1018 mild/low carbon steel specimen with mean roughness index (a) fine [R_a = 0.8 µm], (b) grinded [R_a = 1.4 µm], and (c) milled [R_a = 5.0 µm]

2.2 Shock Tube

A shock tube apparatus was used to generate a concentrated in air shockwave that is imparted on the panels (Fig. 2a). The total length of the shock tube is 8 m and is composed of three separate sections: driver section, driven section, and reduced diameter muzzle section. A Mylar diaphragm separates the driver and driven sections, while the driver section is pressurized using helium gas. Under critical pressure the diaphragm bursts, releasing a high pressure wave. The high pressure wave travels down the length of the driven section and develops into a shock wave front. The shockwave then travels through the muzzle section and the pressure of the event is captured by two dynamic pressure transducers (Fig. 2b). The pressure transducers capture the magnitude of the pressure while velocity of the wave can be inferred from the time between pressure histories and established positions of the sensors. The shockwave then leaves the muzzle, impacts the specimen and the pressure from the impact is reflected back into the muzzle. The reflected pressure is the pressure that loads the specimen. A detailed dimension of the muzzle section is shown by Fig. 2b.
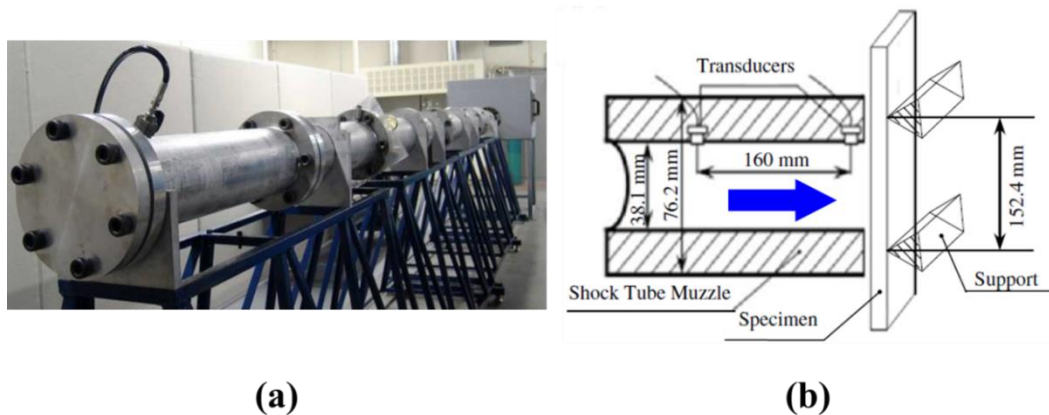
Fig. 2: (a) Shock tube apparatus and (b) detailed dimensions of the muzzle

In this study, the final muzzle diameter was 0.0381 m (1.5 in). The distance between the two sensors was 0.160 m and the distance between the second sensor and the end of the muzzle was 0.020 m. The pressure of the shockwave was created using a 0.35 mm thick Mylar diaphragm with a burst pressure of about 0.75 MPa. Two PCB Piezoelectric pressure transducers were mounted flush to the interior of the muzzle. Data was recorded using a Tektronix DPO 3034 Digital Phosphor Oscilloscope. The consistent burst pressure of the Mylar diaphragm and set muzzle standoff distance produce repeatable experiments. The specimen was placed in the supports and positioned 3 mm away from the end of the muzzle. The support fixtures ensured simply supported boundary conditions with a span length of 152.4 mm. To reduce the effects of friction during deformation, the panels were positioned over a block, where contact is only on the edge of the back face. The specimen was then secured to the simple support using Nickel-Chrome wire with a diameter of 0.05 mm, which easily breaks during shock loading and deformation.

2.3 High Speed Photography Systems

High speed photography coupled with 3D Digital Image Correlation (DIC) was utilized to provide full field displacements, strain, and velocities of shock tube specimens during in air shock loading. Two high speed cameras were setup to view the back face of the specimen for 3D DIC while a side view camera was positioned to view the out of plane deflection as shown by Fig. 3. The cameras used during experimentation were Photron FastCam SA1. Images of the event from all cameras were taken at 50,000 fps for an inter-frame time of 20 μs.
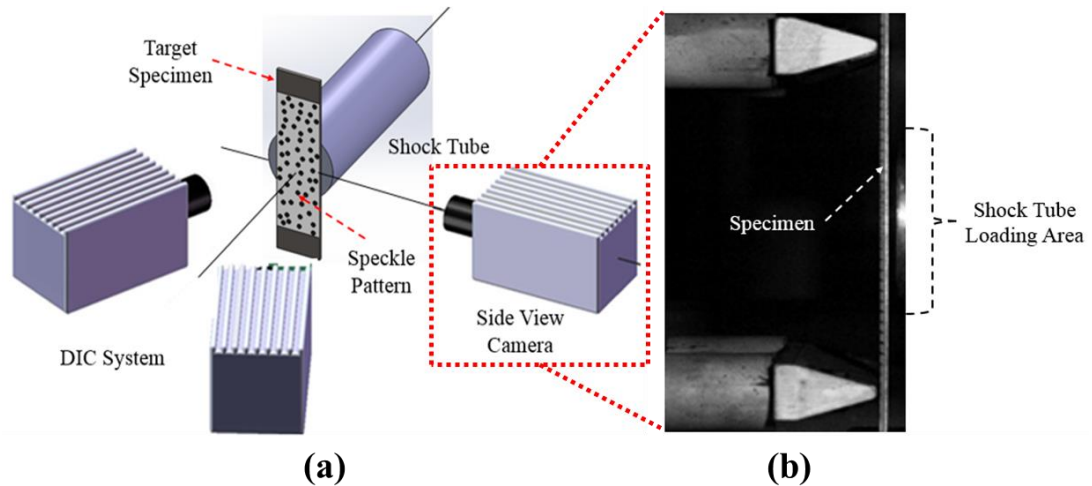
Fig. 3: (a) schematic of high-speed photography systems with respect to the muzzle, and (b) typical side-view image of the simply supported boundary condition

To record the transient response with the high speed system, the cameras were calibrated and had synchronized image recording throughout the event. The calibration of the cameras was performed by placing a grid containing a known pattern of points (dots) in the test space where the specimen was located during the experiment. This grid was then translated and rotated in and out of plane while manually recording a series of images. This grid pattern was predetermined and the coordinates of the center of each dot was extracted from every image thus allowing for a correlation of the coordinate system of each camera. Prior to conducting the experiments, the face of the plate facing the cameras was painted with a random speckle pattern as shown by Fig. 3a and then the plate was positioned vertically in the simple support with a muzzle gap of about 3.0 mm (see Fig. 3b).

The Photron Fastcam Viewer (PFV) software was employed to synchronize the high speed cameras and record the images during the experiments. PFV is a user interface that enables the editing and storage of captured images and videos. The post

processing was performed with the VIC-3D software package which matches common pixel subsets of the random speckle pattern between the deformed and un-deformed images. The matching of pixel subsets was used to calculate the three-dimensional location of distinct points on the face of the plate. This provides a full field deformation history of the transient event with time.

3. Experimental Results and Discussion

The experimental data obtained were carefully analyzed to obtain the impulse imparted to the specimen, back-face deflections, in-plane strains, and the energy used in deforming the specimens.

3.1 Pressure Profile and Impulse

The pressure history for each experiment is shown in Fig 4. Recall that channel 1 is the closest to the specimen (23 mm away) and channel 2 is the furthest from the specimen (183 mm away) (see Fig 2b). For each experiment, the incident shock wave traveled inside the muzzle with an average velocity of 900 m/s and was reflected with an average velocity of 250 m/s, translating to approximate Mach numbers of 2.64 and 0.73, respectively. The reflected shock wave had a short rise time of about 0.05 ms and showed an exponential decay period of approximately 1.0 ms. The overall time period of the load acting on the plates (reflected pressure) was the same for different plate's surface roughness. The time period is defined as the time at which the pressure becomes equal to the atmospheric pressure. The time period of the reflected pressure was about of 6.0 ms.
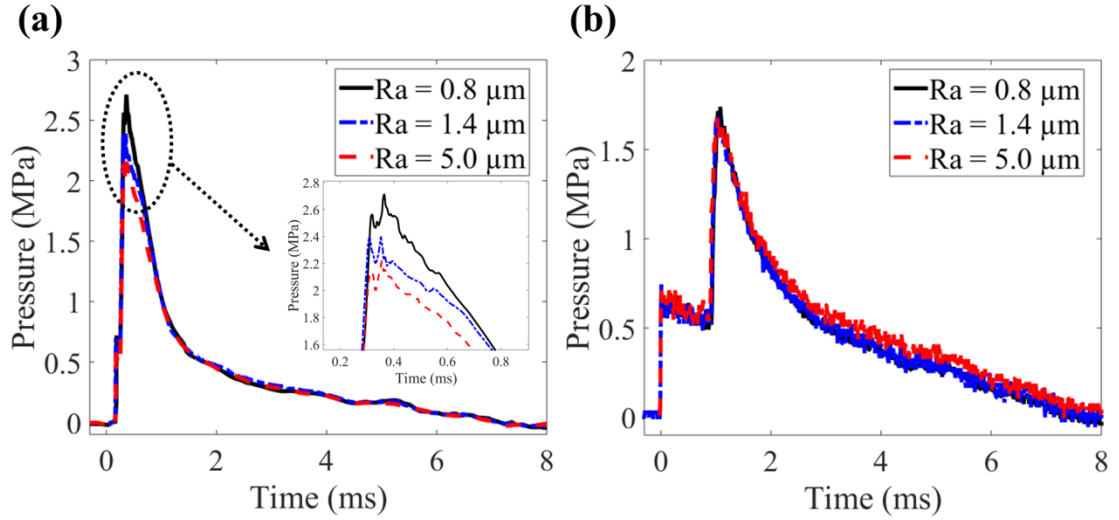
Fig. 4: Recorded pressure profiles measured for different plate's surface roughness (a) 23 mm (b) 183 mm upstream

For the same incident peak pressure, reflected peak pressures were not the same for different plates' surface roughness (see Fig. 4a). The plate with fine surface roughness showed a reflected peak pressure of approximately 2.6 MPa, whereas plates, which have grinded and milled surface showed reflected peak pressures of about 2.4 MPa and 2.2 MPa respectively. This indicates that when the surface roughness of the plate was increased from 0.8 μm to 5.0 μm, the reflected peak pressure decreased by approximately 15%. For further distance at sensor located 183 mm away from the specimens, the specific surface roughness of the plates had no influence on the reflected peak pressure (vanished) as shown by Fig. 4b. This indicates that the effect of different plate's surface roughness is highly localized, and that effect vanished at greater distances upstream.

The pressure reduction due to higher plate's surface roughness can be better seen as represented by the areal impulse imparted to the plate as shown by Fig. 5. The

areal impulse was calculated by integrating the pressure-time data of the reflected pressure profile. The plate with fine surface roughness obtained a maximum areal impulse of 3000 Pa.s from the shock loading. When the surface roughness of the plate was increased from 0.8 µm to 5.0 µm, the maximum areal impulse imparted to the plate decreased by approximately 15% (3300 Pa.s to 2800 Pa.s).
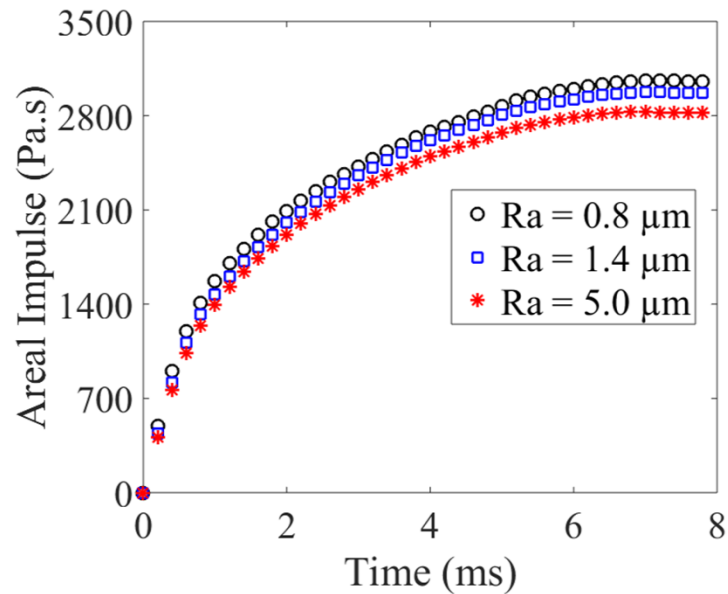
Fig. 5: The true duration of imparted impulse on plates with different surface roughness at channel 1

3.2 Real Time Deformation Images

The real-time observations of the transient behavior of 1018 mild/low carbon steel specimen under shock loading for different surface roughness are shown in Fig. 6. The shock wave is propagating from the right side of the image to the left side causing deformation in the specimens. Time t = 0 µs corresponds to the beginning of the event where the shock wave impinged on the specimen and the final image for

each surface roughness represents the maximum deflection of the specimen. These images were later used to calculate the midpoint deflections in the specimens.

At fine surface roughness, large elastic–plastic deformation was observed at the center of the specimen during the shock loading which resulted in global bending. Compressive stresses in the front-face and tensile stresses in the back-face of the specimen were generated during the global bending deformation. The mid-point deflections increased monotonically with time. By t = 2000 μs, the specimen had deflected by 36.4 mm on the back-face and reached a maximum deflection of 67.0 mm at t = 5400 μs. The impulse imparted to the specimen had the tendency to increase even after this time (t = 5400 μs) as shown in Fig. 5. However, the pressure applied was not high enough to cause further deformation in the specimen.

Similar to fine surface experiment, large plastic deformation was observed for grinded and milled surface experiments and the specimens compressed monotonically with time. The specimens with grinded and milled surfaces reached maximum midpoint deflections of 60.0 mm and 49.0 mm at 5000 μs and 4000 μs respectively. As shown in Fig. 5, the impulse imparted to the specimens at higher surface roughness was significantly less than that at fine surface finish which resulted in lower peak deflections. The manner in which the shock wave was reflected by a surface is dependent on the microscopic shape characteristics of the surface. A smooth surface may reflect the shock wave in a single direction, while a rough surface will tend to scatter the shock wave in various directions. Consequently, for the same applied pressure, specimens with higher surface roughness deformed for a shorter time and reached lower deflections than the fine surface roughness specimen.
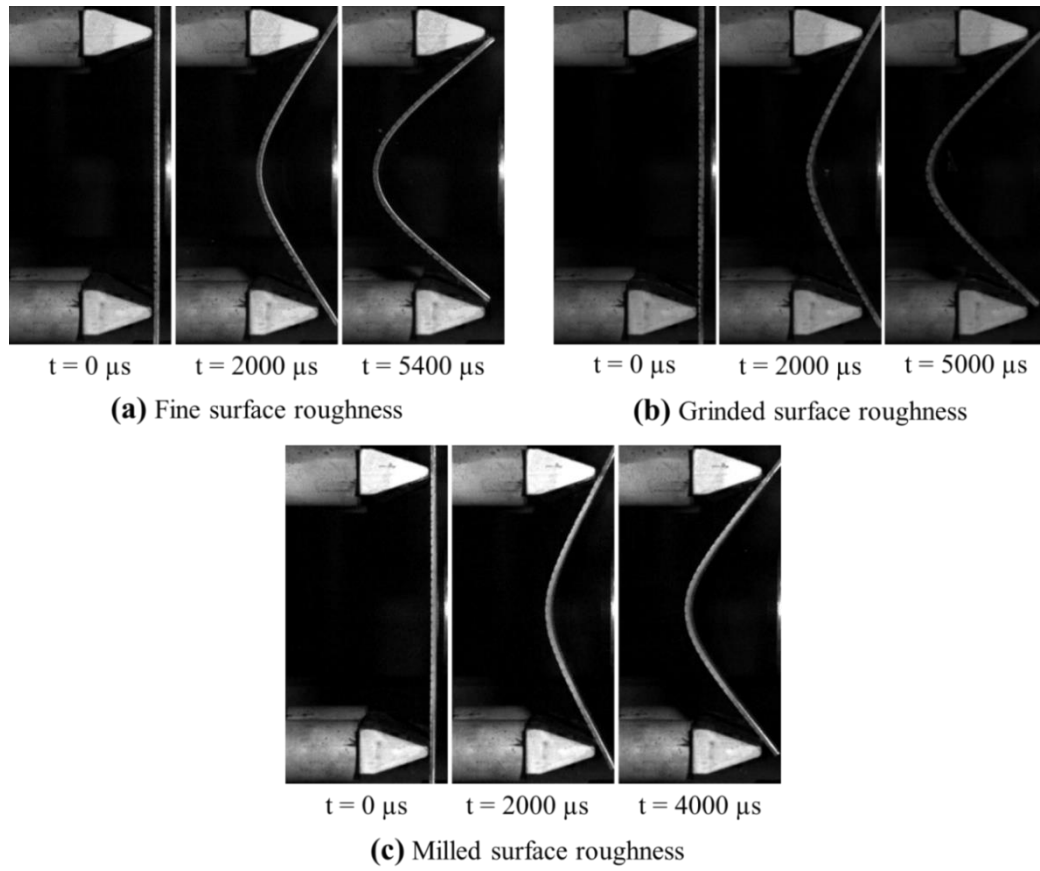
Fig. 6: Real-time side-view deformation images of 1018 mild/low carbon steel at different surface roughness

3.3 Digital Image Correlation Analysis

The deflection, in-plane strain (ε_{yy}), and the velocity of the back face for each experiment were generated using 3-D Digital Image Correlation (DIC) technique. To verify the performance of the DIC method, the back-face mid-point deflections obtained using the proposed DIC technique were compared with the deflections measured from the side-view images (Fig. 6). The comparison of the deflections obtained from the DIC and the side-view images for the fine and milled surface finish experiments is shown by Fig. 7. For both experiments, the deflections obtained from the DIC matched very well with the deflections measured from the side-view images

133

(maximum difference at peak deflections is less than 2%). The results confirm the accuracy of the DIC technique.
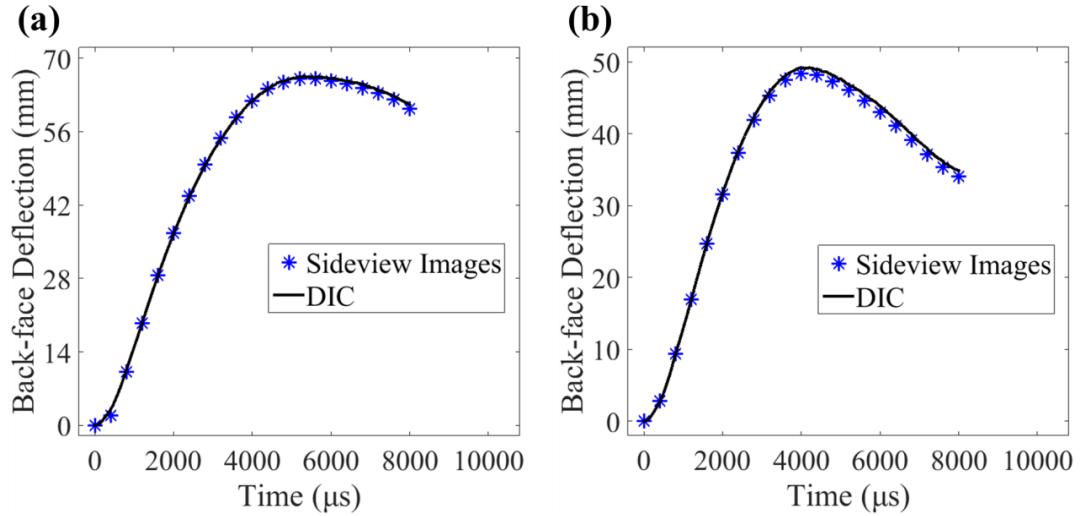
Fig. 7: Comparison of mid-point deflections obtained from the DIC technique with side-view images for specimen at surface finish (a) [$R_a = 0.8$ μm] and (b) [$R_a = 5.0$ μm]

According to Abotula et al, the structural response of monolithic plates subjected to a shock loading is partitioned into two consecutive phases [8]. The first structural response is referred to the initial fluid structure interaction process, where non-uniform or transient deflection contours observed and the effects of the boundary conditions had no influence on the structural dynamic response of the plate. The second structural response is referred to the retardation phase, where the plate is brought to rest by plastic bending and stretching.

The deflection on the back face of the specimen during the fluid structure interaction between the gas and the specimen is shown in Fig. 8. The shock impinged on the specimen at t = 0 μs. The localized deflection contours were observed during the early stages of the event. The transient deflection contours on the back-face evolve

with time. After a critical time (~100 μs), the non-uniform loading disappears and a near-uniform loading was achieved, where the stress wave effects became stabilized. This time interval can be related to the characteristic fluid–structure interaction time. The characteristic FSI time was approximately 100 μs for all experiments studied. Similar fluid structure interaction time for steel and sandwich plates was reported by Xue and Hutchinson [23].
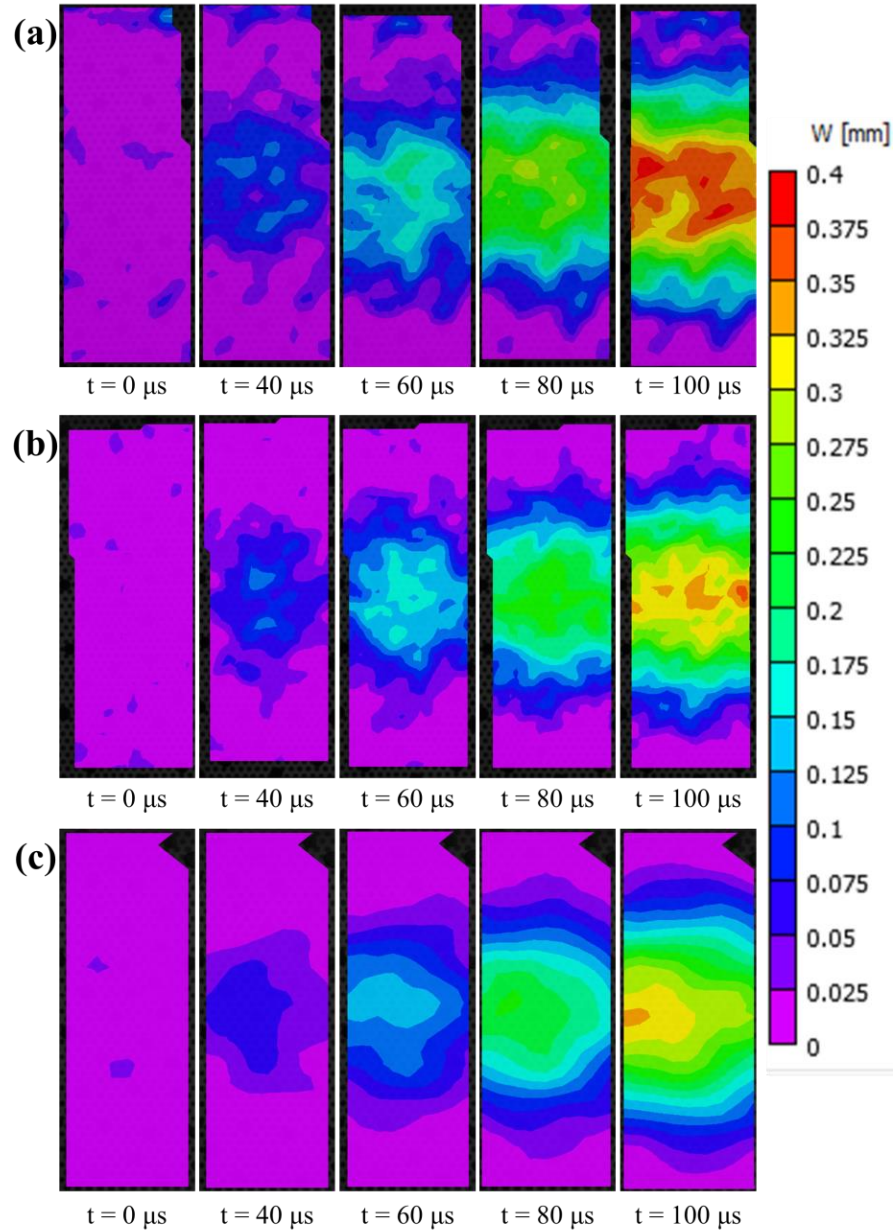
Fig. 8: Deflection of the back face during fluid structure interaction time for (a) fine, (b) grinded, and (c) milled surface finish specimens

The data at the center point of the back face for each experiment was evaluated and plotted using the point-inspection tool from the digital image correlation software. The surface roughness effect on the mean back-face deflection history is shown in Fig. 9. All of the curves exhibit a maximum elastic–plastic deformation in the first peak,

followed by elastic reverberations and damping. For all experiments, the specimens deflected in a similar manner prior to reaching their maximum deflections and beginning to reverberate. As discussed earlier in Fig. 6a, the fine surface finish specimen ($R_a = 0.8$ μm) showed a maximum deflection of 67.0 mm at t = 5400 μs and then began to reverberate. As the surface roughness increased to $R_a = 1.4$ and 5.0 μm for the same incident pressure loading, the panel reached maximum back-face deflections of 60.0 mm and 49.0 mm at 5000 μs and 4000 μs and then began to reverberate respectively. It should be noticed that the specimen with higher surface finish began to reverberate ahead of time, 400 μs and 1400 μs (for grinded and milled surface cases respectively), as compared to fine surface experiment. At t = 8000 μs, the specimen which had a surface finish of $R_a = 5.0$ μm settled with 43% less out-of-plane deflection as compared to the specimen of $R_a = 0.8$ μm surface finish.
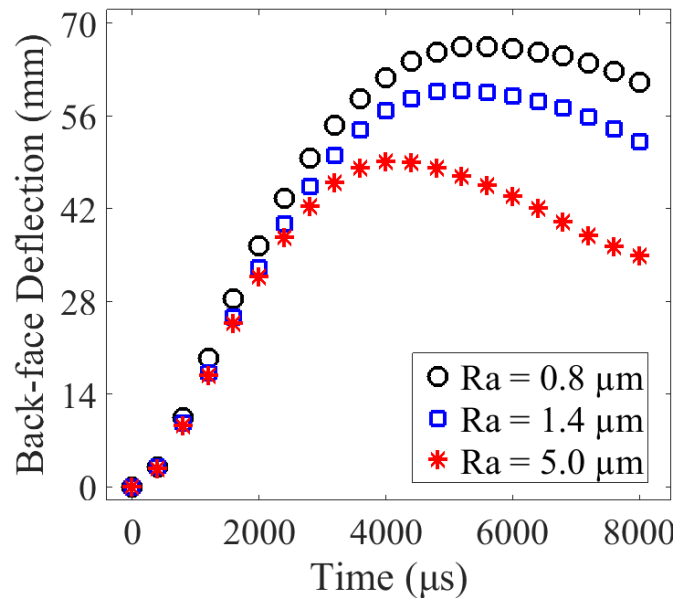
Fig. 9: Mean mid-point back-face deflections using stereo-DIC analysis for different surface finish specimens

The full field out-of-plane deflection (W) images for different surface finishes, with a scale of 0 mm (purple) to 67.0 mm (red), are shown in Fig. 10. It is important to note here that these deflections were obtained for much longer times than shown in Fig. 8. For a better comparison, the time scales were kept constant for all experiments. At time t = 0 μs, the shock wave impinged on the specimen. For all experiments, similar deflection contours were observed during the early time of the event until t = 600 μs and the specimens exhibited out-of-plane deflections of 5.0 mm. For the specimen with Ra = 0.8 μm surface finish, between t = 600 μs and t = 2000 μs, a significant amount of deflection was observed of 36.5 mm (see Fig. 10a). At this time (t = 2000 μs), the specimens with (Ra = 1.4 and 5.0 μm) surface finish had shown significant mid-point back-face deflections of 33 mm and 31 mm respectively (see Fig. 10b, c). At t = 4000 μs, as the specimen with (Ra = 5.0 μm) surface finish had maximum deflection of 49.0 mm and began to reverberate, the specimens with lower surface finish continued to deform. The specimen with (Ra = 1.4 μm and 0.8 μm) surface finish deformed further for 1000 and 1400 μs before reaching its maximum deflection of 60.0 and 67.0 mm at 5000 and 5400 μs respectively. It should be noticed that the maximum back-face deflection of the specimen with Ra = 5.0 μm was approximately 27% lower than the back-face deflection of the specimen with Ra = 0.8 μm.
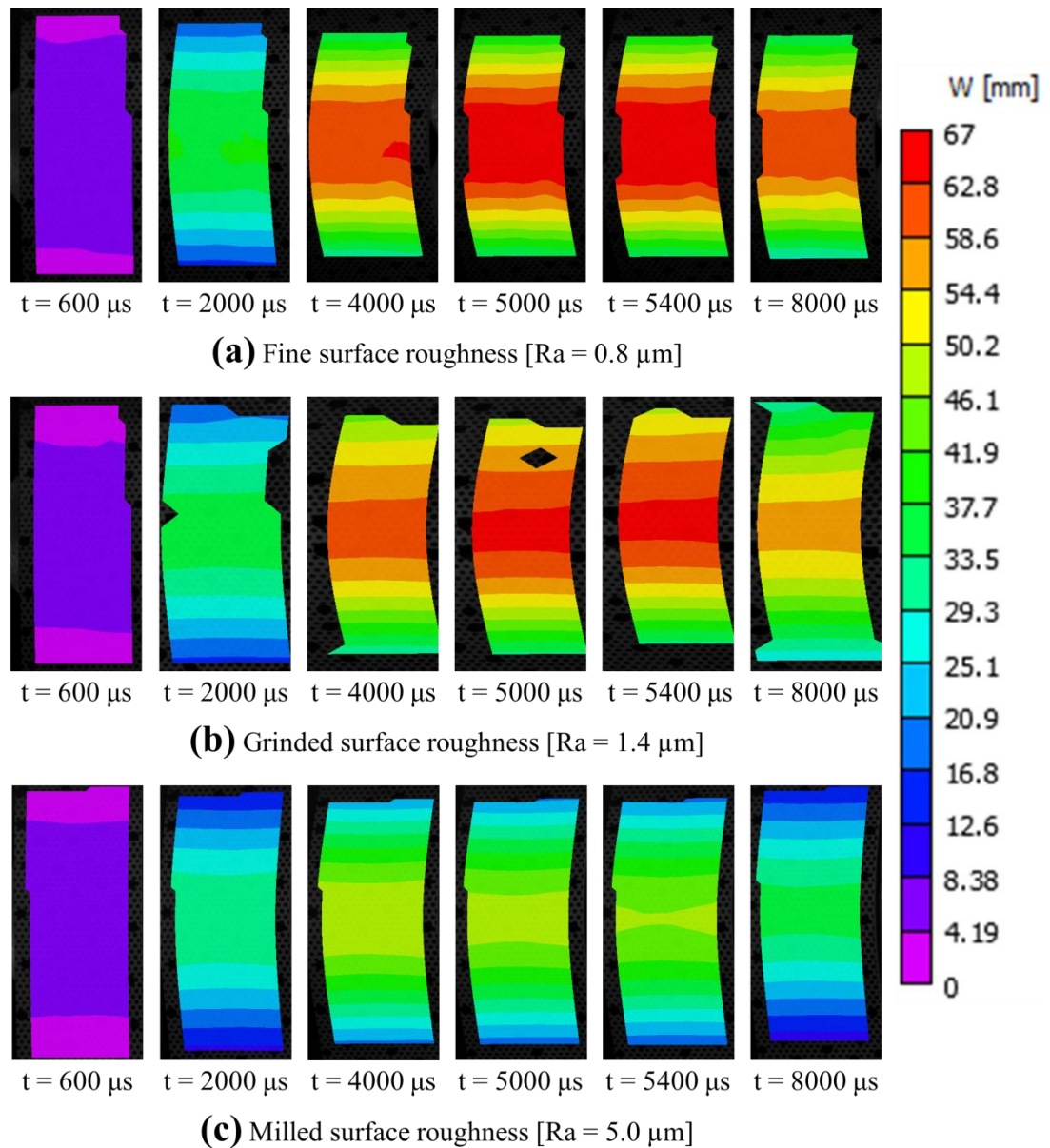
Fig. 10: Full-field out-of-plane deflection contours of specimen for different surface finishes with a scale of 0 mm (purple) to 67 mm (red)

The mid-point in-plane strains (ε_{yy}) on the back-face of the specimen are plotted in Fig. 11. It can be observed from the figure that all the specimens exhibited similar in-plane strain profile of about 0.27% up to t = 400 μs. After t = 400 μs, the specimens showed significant bending, which resulted in higher in-plane strain values.

At surface roughness of R_a = 0.8 μm, a maximum in-plane strain of 7.0% was observed at t = 5400 μs. As the surface roughness increased, the specimens exhibited lower deflections (less bending, see Fig. 6), causing a decrease in the in-plane strain values. For R_a = 1.4 μm and R_a = 5.0 μm experiments, the specimens showed maximum in-plane strain of 5.5% and 4.2% at 5000 μs and 4000 μs, respectively. In comparison to the fine surface roughness experiment, the specimens with R_a = 1.4 μm and R_a = 5.0 μm showed a decrease in ε_{yy} of 22% and 40%, respectively.
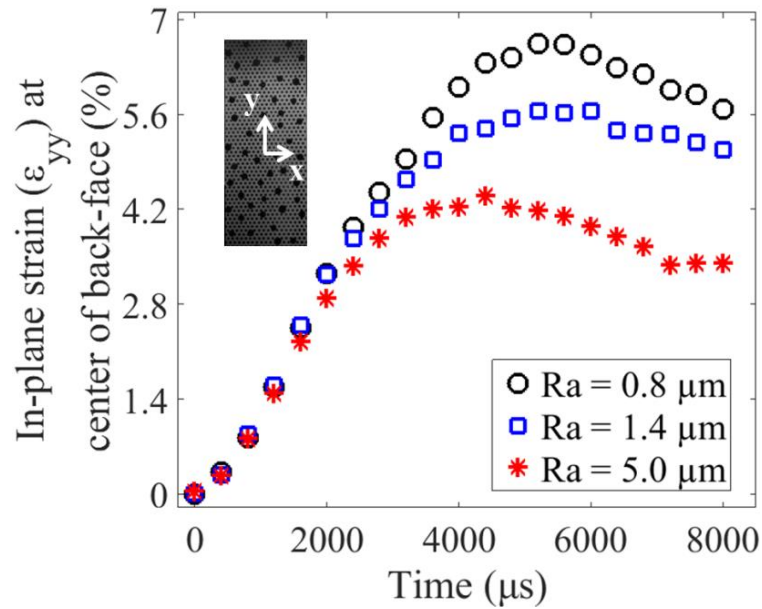
Fig. 11: Mid-point back-face in-plane strains at the center of the specimen for different surface finishes

The out-of-plane particle velocity (dW/dt) on the back face of the specimen at different surface finishes is plotted in Fig. 12. All the experiments showed similar velocity profiles up to t = 400 μs at which time the specimens reached a velocity of 12 m/s. At fine surface roughness (R_a = 0.8 μm), the specimen reached a maximum velocity of 24 m/s at t = 800 μs and started to decelerate after that. The velocity

continues to be reduced to approximately 0 m/s as the specimen reached its maximum

deflection (at t = 5400 μs) and began to reverberate. Under high surface roughness

experiments at R_a = 1.4 μm and R_a = 5.0 μm, a maximum velocity of 20 m/s and 18

m/s was observed at t = 800 μs respectively. At t = 5000 μs and t = 4000 μs, the

specimens with R_a = 1.4 μm and R_a = 5.0 μm reached their maximum deflection and

began reverberating as shown by the negative velocities.
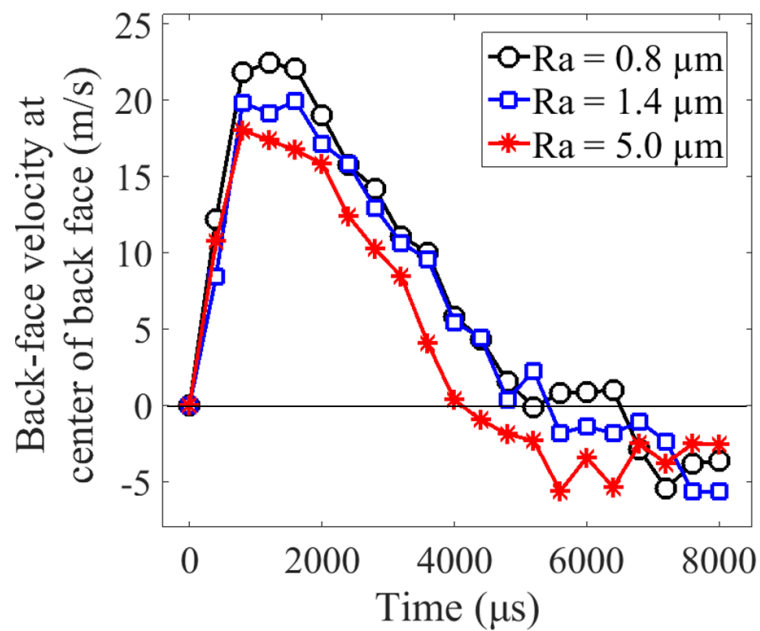
Fig. 12: Back face out-of-plane velocity profiles of specimen at different surface
finishes calculated from DIC

3.4 Deformation Energy Evaluation

According to Wang and Shukla [24], the total work done by the gas to deform

the plate is defined as the deformation energy. The deformation energy was calculated

by evaluating the deflection-time data from the side-view images (Fig. 6) and the

force-time data (Fig. 5) from the reflected pressure profile. Combining the deflection-

time data and the force-time data resulted in force–deflection data. The deformation energy could then be obtained by integrating the force–deflection data using Equation 1. This energy imparted into the plate is equal to the summation of energies used in panel response outlined in Equation 2.

$$E_{plate} = \oint_{S_{shock\ tube}} \left(\int P_{reflected}\ (t) * dl_{deformation} \right) dS$$

(1)

where,

$$E_{plate} = E_{deformation} + E_{kinetic} + E_{dissipated}$$

(2)

The deformation energy for different plate's surface roughness is plotted in Fig. 13. The maximum deformation energy of 34 J was observed for the plate with milled surface finish. The plates, which have grinded and fine surface finish showed maximum deformation energies of 40 J and 45 J, respectively. The deformation energy for the plate with R_a = 5.0 μm was approximately 25% lower than that for the plate with R_a = 0.8 μm. This indicates that the plates with higher surface finishes absorbed significantly less energy during the shock loading process. As stated in the previous section, the impulse was higher for lower plate's surface roughness. This allows for greater deflections for a given shock load, resulting in higher work done on the specimen during fluid structure interaction.
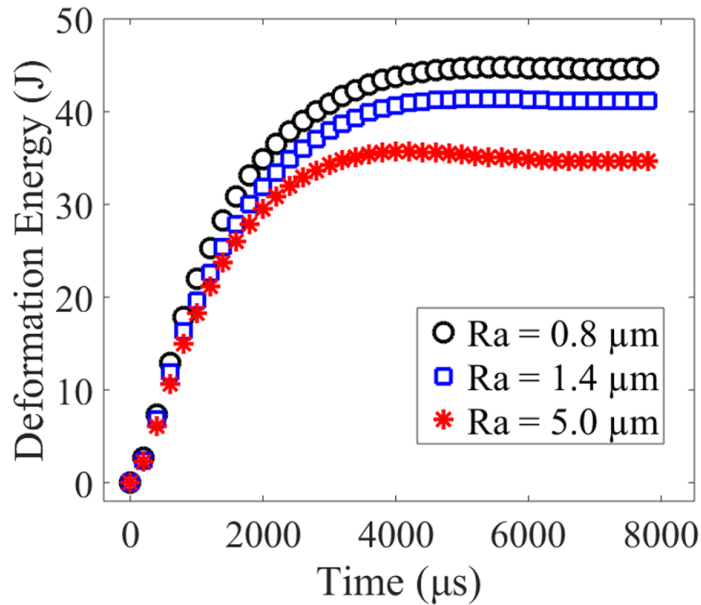
Fig. 13: Deformation energy for different plate's surface roughness

4. Conclusions

Based on results from shock loading experiments of 1018 mild low carbon steel panels with specific machined surface roughness, the following conclusions were drawn:

- In order to decrease the reflected pressure, thus reducing the transmitted impulse and improving the blast wave mitigation, the surface roughness of structures subjected to blast waves should be considered.

- The impulse imparted to the plate decreased by 15% as the surface roughness (R_a) increased from 0.8 μm to 5.0 μm.

- The effect of different plate's surface roughness on the reflected peak pressure is highly localized, and that effect vanished at greater distances upstream.

- The maximum in-plane strain showed a decrease of 40% (from 7.0% to 4.2%) as the plate's surface roughness (Ra) increased from 0.8 μm to 5.0 μm.

- The maximum back-face deflection of the specimen with Ra = 5.0 μm was approximately 27% lower than the back-face deflection of the specimen with Ra = 0.8 μm.

- The amount of deformation energy absorbed by specimens decreased by 25% as plate's surface roughness (Ra) increased from 0.8 μm to 5.0 μm.

Acknowledgment

References

[1] Perl R and O'Rourke R (2001). Terrorist attack on USS Cole: Background and issues for Congress. Emerging Technologies: Recommendations for counter-terrorism. Institute for Security Technology Studies, Dartmouth College

[2] Perl R (1998). Terrorism: US responses to bombings in Kenya and Tanzania: A new policy direction? Congressional Report. Congressional Research Service, The Library of Congress

[3] Langdon, G. S., Nurick, G. N., Balden, V. H., & Timmis, R. B. (2008). Perforated plates as passive mitigation systems. Defence Science Journal, 58(2), 238–247

[4] Nurick GN, OlsonMD, Fagnan JR, Levin A (1995) Deformation and tearing of blast-loaded stiffened square plates. Int J Impact Eng 16(2):273–291

[5] Nurick GN, Shave GC (1996) The deformation and tearing of thin square plates subjected to impulsive loads - An experimental study. Int J Impact Eng 18(1):99–116

[6] Teeling-Smith RG, Nurick GN (1991) The deformation and tearing of thin circular plates subjected to impulsive loads. Int J Impact Eng 11(1):77–91

[7] Wierzbicki T, Nurick GN (1996) Large deformation of thin plates under localised impulsive loading. Int J Impact Eng 18(7–8):899–918

[8] Abotula, S., Heeder, N., Chona, R., & Shukla, A. (2014). Dynamic Thermo-mechanical Response of Hastelloy X to Shock Wave Loading. Experimental Mechanics, 54(2), 279–291

[9] Ajdari, A., Jahromi, B. H., Papadopoulos, J., Nayeb-Hashemi, H., & Vaziri, A. (2012). Hierarchical honeycombs with tailorable properties. International Journal of Solids and Structures, 49(11–12), 1413–1419

[10] Dharmasena, K. P., Wadley, H. N. G., Xue, Z., & Hutchinson, J. W. (2008). Mechanical response of metallic honeycomb sandwich panel structures to high-intensity dynamic loading. International Journal of Impact Engineering, 35(9), 1063–1074

[11] Wang, E., Gardner, N., & Shukla, A. (2009). The blast resistance of sandwich composites with stepwise graded cores. International Journal of Solids and Structures, 46(18–19), 3492–3502

[12] Hassan, M. Z., Guan, Z. W., Cantwell, W. J., Langdon, G. S., & Nurick, G. N. (2012). The influence of core density on the blast resistance of foam-based sandwich structures. International Journal of Impact Engineering, 50, 9–16

[13] Yazici, M., Wright, J., Bertin, D., & Shukla, A. (2014). Experimental and numerical study of foam filled corrugated core steel sandwich structures subjected to blast loading. Composite Structures, 110(1), 98–109

[14] Tekalur, S. A., Shukla, A., & Shivakumar, K. (2008). Blast resistance of polyurea based layered composite materials. Composite Structures, 84(3), 271–281

[15] Gardner, N., Wang, E., Kumar, P., & Shukla, A. (2012). Blast Mitigation in a Sandwich Composite Using Graded Core and Polyurea Interlayer. Experimental Mechanics, 52(2), 119–133

[16] Arun Kumar R, H.D Kim. (2013). Wall Roughness Effects on Shock Boundary Layer Interaction Flows, International Journal of Innovative Research in Science, Engineering and Technology, 2(1), 387–394

[17] J. Mendonca & M.A.R. Sharif (2010) Effects of Surface Roughness on Turbulent Transonic Flow Over Circular Arc Bumps in a Channel, Engineering Applications of Computational Fluid Mechanics, 4:2, 164-180

[18] Wang, E., Wright, J., & Shukla, A. (2011). Analytical and experimental study on the fluid structure interaction during air blast loading. Journal of Applied Physics, 110(11), 1–12

[19] Shi, Y., Hao, H., & Li, Z. X. (2007). Numerical simulation of blast wave interaction with structure columns. Shock Waves, 17(1–2), 113–133

[20] J.Y. Yang, Y. Liu and H. Lomax, (1987). Computation of shock wave reflection by circular cylinders, AIAA journal, Vol. 25, No. 5, pp. 683-689

[21] S. M. Liang, J. L. Hsu and J. S. Wang. (2001), Numerical study of cylindrical blast-wave propagation and reflection, AIAA Journal, Vol. 39, No. 6, pp. 1152-1158

[22] Peng, W. (2009). Modeling And Simulation Of Interactions Between Blast Waves And Structures For Blast Wave Mitigation. Mechanical (and Materials) Engineering--Dissertations and Student Research

[23] Xue Z, Hutchinson JW (2004) A comparative study of impulse resistant metal sandwich plates. Int J Imp Eng 30(10):1283–1305

[24] Wang E, Shukla A (2010) Analytical and experimental evaluation of energies during shock wave loading. Int J Impact Eng 37(12):1188–1196

CHAPTER 6: RECOMMENDATIONS AND FUTURE WORKS

Upon completing this dissertation, research gaps have been identified and could be addressed during future works. Based on the results from the shock loading and mitigation research studies, the following recommendations are made:

1. Response of Coated Laminated Glass Panels Subjected to Combined Blast and Temperature Loadings

- For a strong blast performance of coated laminated glass panels, both the interlayer and the coating film should have high ductility and strength at the target temperatures. Different coating materials designed for more extreme temperature ranges (below -10 °C and higher that 110 °C) should be considered.

2. Novel Impact Mitigation Technique using Shock Loading

- The impactor design and independent trigging mechanism should be improved so the capacity of a bladder as well as the trigger mechanism increases in mitigation efficiency.

- An optimization analysis should be performed to find the ideal needle length and shock release time so the energy mitigation is maximized.

- This device could be investigated towards reducing the effects from shrapnel.

3. Blast Performance of Perforated Structures

- Quantitative 3D-density measurements of the transmitted shock waves could be evaluated using a Background Oriented Schlieren (BOS) technique with high-speed photography.

4. The Influence of Surface Roughness on Blast Mitigation

- An increased range of surface roughness could be investigated to the (R_a) profiles of each texture and to obtain the optimal roughness and reduce the imparted impulse.

- A finite element model could validate experimental results and be used to investigate the fluid structure interaction and how the surface roughness changes this interface.

- A post-mortem study could be undertaken using the Scanning Electron Microscope (SEM) imaging to look at any surface roughness alteration.

APPENDICES

APPENDIX A: DETAILED SCHEMATIC OF EXPERIMENTAL SETUP
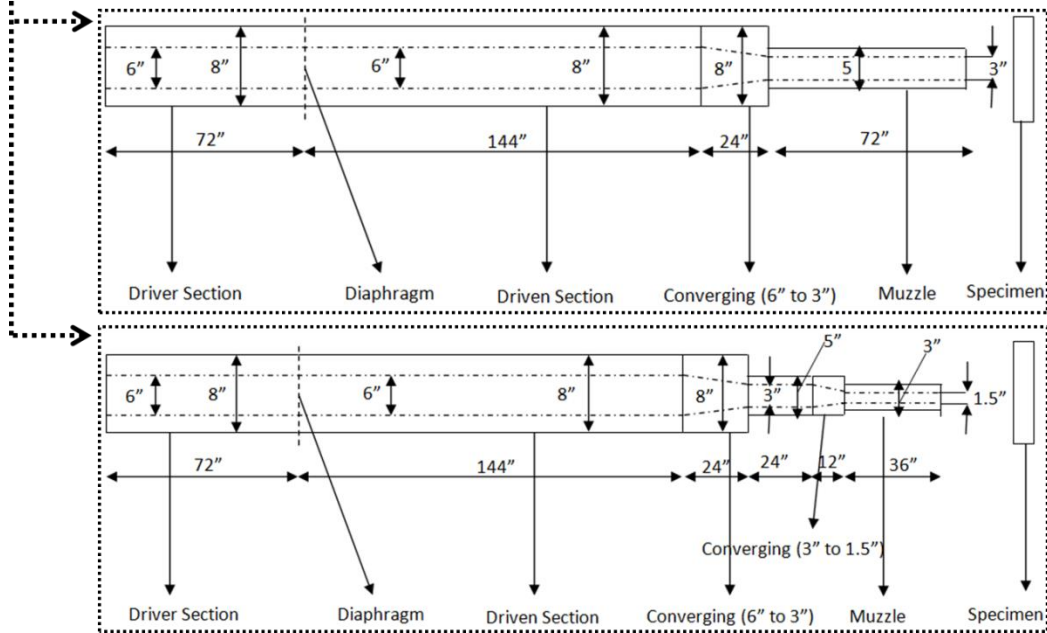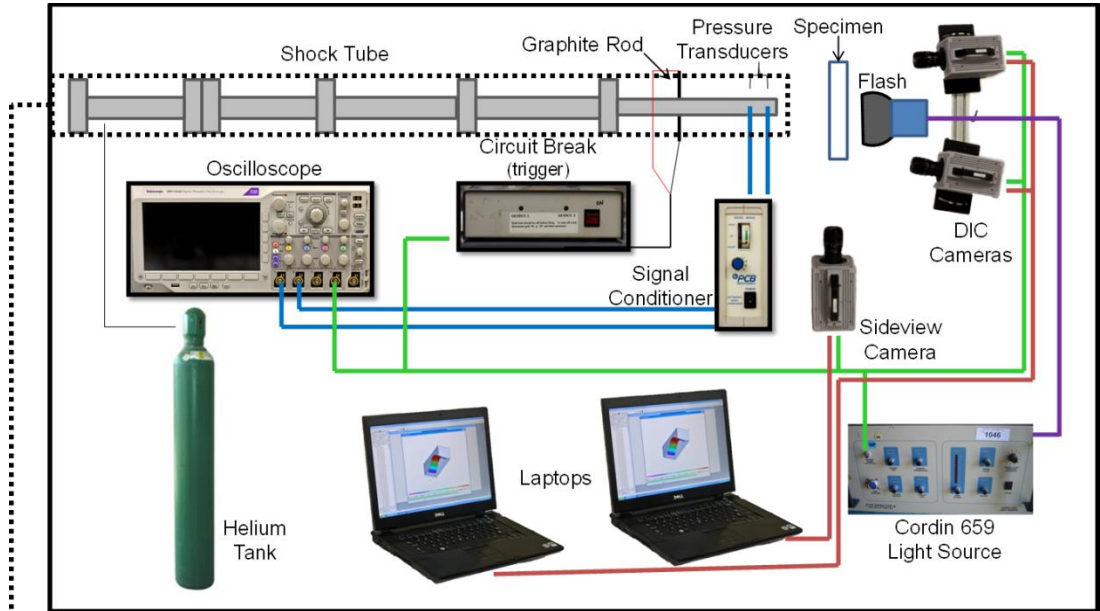
APPENDIX B: STANDARD OPERATING PROCEDURES (SOP)

SHOCK TUBE

Checklist Before Experiments:

Shock Tube Related:
☐   Do you have enough **GAS** and **GAS PRESSURE**?
☐   Do you have enough **MYLAR SHEETS**?
Dump Tank Related:
☐   Is the support **FIXTURE** tight in the dump tank?
☐   Are the supports in the right **SPAN** position?
☐   According to your experiment, do you need the **EXTRA SPACERS** for the support?
☐   Is the side window, **LEXAN SHEET**, clean?
☐   Are the back windows, **LEXAN SHEETS**, clean?
☐   Are the back windows, **LEXAN SHEETS**, **1/2 in.** thick?
Visualization System Related:
☐   Does every **LIGHT** work fine?
☐   Does every **CAMERA** work fine?
☐   Does **LAPTOP** work fine?
Specimen Related:
☐   Have you measured the specimen's **SIZE**?
☐   Have you measured the specimen's **WEIGHT**?
☐   Is your **SPECKLE PATTERN** OK?
☐   Have you taken the **pre-blast IMAGES** of the specimen?

Checklist During Experiments:

Shock Tube Related:

☐   Have you changed the **MYLARS**?

☐   Are all the screw connections **TIGHT**?

☐   Have you put the **PRESSURE SENSORS** in the shock tube?

☐   Is the shock tube **PERPENDICULAR** to the supports, and centrally located?

Dump Tank Related:

☐   Is the specimen in the right position and secure?

☐   Is the shock tube close enough to the specimen, 1/16 in?

☐   Have you put the side doors on the dump tank?

☐   If no back side DIC system is required, have you installed a good protection for the back side LEXAN windows ?

DIC System Related:

☐   Have you double checked the camera **CABLE CONNECTIONS**?

☐   Is the back view camera system **PERPENDICULAR** to the back side window?

☐   Is the side view camera **PERPENDICULAR** to the side window and specimen?

☐   Have you set the right **FRAME RATE**?

☐   Have you done the **BLACK CALIBRATION (SHADING)**?

☐   Is the viewing area acceptable (make the view of the specimen as large as it can)?

☐   Have you **FOCUSED** on the specimen (use iris 2.8 or smaller)?

☐   Have you increased the **IRIS** to at least 5.6?

☐   Have you set **SYNC MODE** for all slave cameras (E-SYNC)?

☐   Have you done the correct **CALIBRATION (grids used to track particle distance)**?

☐   Have you set the right **TRIGGER MODE**?

☐   Have you double checked that the cameras can take the desired images?

DIGITAL IMAGE CORRELATION (DIC) ANALYSIS

TEST AND CAMERA PROCEDURE

Physical Setup – Prior to any software

1. Set up lamps
2. Keep lens caps on cameras
3. Plug in cameras
    1. Turn on master
    2. Turn on slave
    3. Wait for "sync in" light on slave camera before starting any software
    4. Make sure IP light is also on

Software Setup

1. Start software – PFV
2. Go to Cam2 window
    1. Right click
        1. CAM options
            1. I/O
                1. Set sync in to "ON CAM POS"
                    1. E-Sync shows up in window
3. Set frame rate to 20,000 fps (or desired rate)
4. Shading
    1. Make sure lens cap is on
        1. Click calibrate
    2. Do this for each camera!!!

5. Now all set with software setup

Camera Setup (Focus and Calibration)

1. Take lens caps off
2. Focus and set aperture on the lens itself
    1. Set aperture to 2.8 initially for focusing the camera
    2. Maximize window of interest in the software for focusing and hit fit
    3. Set aperture to 5.6 for calibration
    4. Repeat for each camera
3. Calibrate the Cameras
    1. Trig Mode = Random, 1 frame
    2. Hit Record button in software
    3. Move the calibration sheet and hit the trigger button repeatedly while rotating and translating the cal sheet
    4. Once sufficient images (>100) are captured hit record done
4. Data Save Tab
    1. Select the folder to save the calibration iimages
        1. Save CAM 1 (Cal_0_), Type = TIFF
        2. Save CAM 2 (Cal_1_), Type = TIFF
        3. Run Through the calibration process in VIC-3D

Camera Usage (Actual Test)

1. In the camera software
    1. Camera Tab
        1. Hit Display "Live"
2. Set Trigger mode to "END"
3. Hit record button (software) one time
    1. Light goes to orange, and will say Trig In
4. Hit the Trigger (physical) button to begin recording
5. Hit the Trigger button again to stop recording

1. The software will record the images for the 1 second prior to the stop recording push. Therefore you should stop the recording as soon as possible after the event or you will miss the data.
6. DO NOT TURN OFF THE CAMERAS UNTIL THE DATA HAS BEEN SAVED
7. Check the start point of motion with the red slider bar (the middle number is the current frame)
    1. Hit left facing arrow to set begin point to current frame
    2. Play until end of motion and hit stop
    3. Hit right arrow to set end of frames

You have now isolated the frames that comprise the event

Data Save

1. Set the folder for the data to be saved to
    1. This is different than the folder the calibration is saved to
2. Select Camera 1
    1. File names (Data_0_), Type = TIFF
    2. Save
3. Select Camera 2
    1. File names (Data_1_), Type = TIFF
    2. Save

DATA CALIBRATION AND POST PROCESSING

1. Open VIC-3-D Program
2. Click Grid Icon (Cal Images)
    1. Find Calibration images from test
    2. Open all
3. Click caliper button
    1. Select Target (12x12x9 or whatever used during test)
    2. Extract
    3. Auto

4. Calibrate
    1. Standard Deviation should be <0.1 and should have used at least 75 images
5. Now you are done with the calibration part
4. Click the speckle images icon
    1. Select the images recorded during the test
    2. Under AOI tools tab
        1. Select the type of view area (rectangle, polygon, etc.)
        2. Select the view area
        3. Take the green box and move to a area of low deformation with a high quality speckle dot
        4. Click the "?" icon
            1. Dic_0 → camera 1
            2. Dic_1 → camera 2
            3. Verify that both cameras are seeing the dot with a checkmark next to the image by scrolling through the images with the down arrow. If there is not a chackmar next to each image then go back and select a new green box location
            4. Click close
        5. Now all ready for post processing
5. Click the "start analysis" button
    1. Run
    2. The code will run through the images with Z Displacement initially
    3. Done
6. Data drop down menu
    1. Post processing
        1. Calculate curvature
        2. Calculate strain
        3. Calculate velocity
            1. Input time step as the inter frame time

4. Close

7. Data tab under AOI Tools

    1. Can click on the individual pictures now

    2. Right click to change contour levels

    3. Plot tools → Autoscale

        1. Uncheck Boxes

    4. Contour, set range

    5. Right click to create animations

        1. Different coding methods increase or decrease the file size

    6. Inspector tools

        1. Point, Line etc.

            1. 'X' icon to extract time histories

DIC Coordinate System
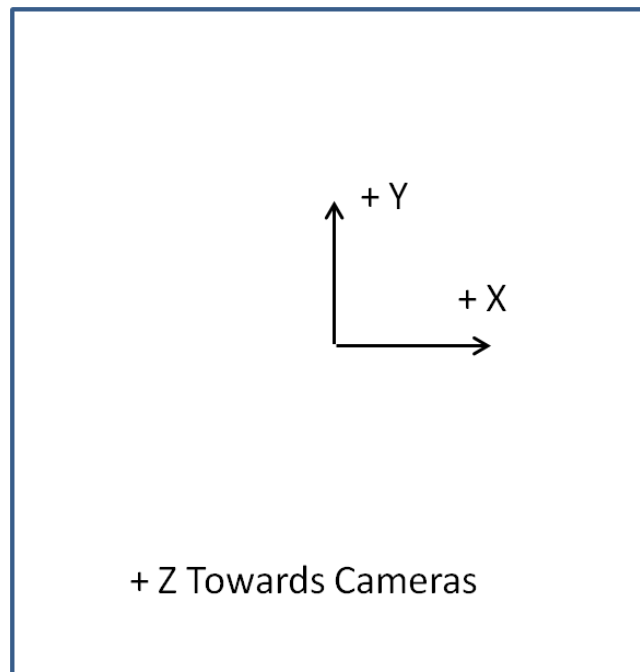
ENERGY ANALYSIS

This manual is designed for the steps to use the energy and impulse analysis code.

    (1) Obtain the original data

The original data of shock tube experiments are from the Tektronix oscilloscope (TDS3014 or 3014C). The data must have following name:

First channel: TEK00000.csv

Second channel: TEK00001.csv

Normally, there are two columns in these files. The unit of the first column is second (s). The unit of the second column is voltage (v).Please copy these files into the folder named "experimental data backup".

    (2) Analyze the original data. This step is to analyze the original data to obtain the shock wave velocity, the peak pressure and the modified pressure profiles.

This step is carried out in the folder named "original data analysis". In this folder, the m file named profile_analysis.m is necessary. Other files can be deleted or replaced. You must copy the original data files into this folder and then run the code. The running process is as follow,

    (1) The code will first ask you how many plys you use in the experiment. This information is only for your record. It does not matter the analysis process.

    (2) The code will ask you the sensitivity of the sensors. This value is given in the box of the sensors. This value means how many milli-voltages related to 1 psi.

    (3) Then, a figure with two plots of the pressure profiles will be given. Look at this figure carefully and determine an approximate biggest time before the first jump time of channel 1. (This time should be less than and as close as possible to the first jump time of channel 1. Normally, should not be farer from the first jump time than 200 microsecond)

    (4) Then the code will inform you as follow,

"The peak and velocity data have been saved into the file, which isnamed peak&velocity.txt and in the same folder of this code.

There are two more pressure data files in this folder:

inc_sp.dat

ref_sp.dat

They can be used for energy and impulse evaluation.

The code will give some plots to verify your data.

Please double check them very carefully.

press any key to continue"

(5) After pressing any key, the code will give four images:

Figure 1 Original Data

Figure 2 Modified Pressure Profiles

Figure 3 Pressure profile of Channel 1 with key point marks

Figure 4 Pressure profile of Channel 2 with key point marks

Look at these figures very carefully, especially Figure 3 and 4. If the jump points and peak points are not right, you may need to manually pick up the jump points and peak points.

(6) There will be three saved files in the same folder,

inc_sp.dat

ref_sp.dat

peak&velocity.txt

The first two files will be used to analyze the energy and impulse. There are two column data in these two files. The first column is time with unit second (s). The second column is pressure data with unit psi.

The last file records the physical parameters, which needs to be input in the energy and impulse analysis.

(7) Please cut these three data files into the folder named "experimental data backup" and delete all of these files in the current folder.

(3) Analyze the incident and remaining energy and impulse

This step is to use the data obtained in step 2 to analyze the incident and remaining energy and impulse in a shock tube experiment.

This step is carried out in the folder named "gas energy and impulse analysis". In this folder, seven m files are necessary. They are,

Main code: energy_impulse_analysis.m

Function 1: load_data.m

Function 2: skip_points.m

Function 3: density_change.m

Function 4: sound_speed.m

Function 5: velocity_change.m

Function 6: spline_integ.m

Other files can be deleted or replaced. You must copy the data files: inc_sp.dat and ref_sp.dat, into this folder and the correlated blank test data file, inc.dat, from the folder named "blank test data". The code running process is as follow,

(1) The code will first show the format and unit of the data. Please be sure that the data should be the exact format.

(2) Then the code will give the total number of the data and ask you how many points you want to skip. This means if the original data is

Original Data

1	4
2	8
3	5
4	11
5	15
6	7
7	6
8	17
9	12
10	19

Skip two points ⟹
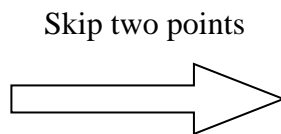
New Data

1	4
4	11
7	6
10	19

160

(3) Then the code will ask you to input physical parameters obtained in step 2 (saved in peak&velocity.txt).

(4) The code will calculate the physical parameter profiles. This process is automatic.

(5) Then the code will integrate the parameter profiles to obtain the energy components. This process is automatic.

(6) Finally, the code will ask you to input the name of the file which you want to save data into. Then all of the data will be saved into filename_gas_energy.mat. The energy and impulse components are saved into ten files as follow,

filename_incident_internal_E.dat	incident internal energy
filename_remaining_internal_E.dat	remaining internal energy
filename_incident_translational_E.dat	incident translation energy
filename_remaining_translational_E.dat	remaining translational energy
filename_incident_work_E.dat	work done by the incident gas
filename_remaining_work_E.dat	work done by the gas behind the reflected shock wave
filename_total_incident_E.dat	total incident energy
filename_total_remaining_E.dat	total remaining energy
filename_total_energy_loss.dat	absolute difference between the total incident and remaining energies
filename_total_impulse.dat	total impulse

Please copy and save these data into a safe folder.

(4) Analyze the deformation energy of the gas, momentum and kinetic energy of the specimen

This step is to use the data obtained in step 2 and the high-speed side-view images to analyze the deformation energy of the gas, momentum and kinetic energy of the specimen in a shock tube experiment.

This step is carried out in the folder named "specimen momentum and energy". In this folder, only one m files, Deformation_momentum_kinetic_photron.m, are necessary. Other files can be deleted or replaced. You must copy the data files: ref_sp.dat, and a series of high-speed images into this folder. The code running process is as follow,

(1) The code will first show the format and unit of the data. Please be sure that the data should be the exact format.

(2) load the time series of the images

You will have three ways to load the time series of the images.

(i) The time between two frames is same. You can input total number of frames and time between two frames. Then the code will generate the time series automatically.

(ii) The time between two frames is not same. You can input total number of frames and input time between two frames frame by frame.

(iii) The time between two frames is not same. The time between two frames is not same. Then you can just load that time series data file.

You can choose anyone and following the instruction.

(3) Length calibration. You can choose any image for length calibration. You will need to choose two points on this image and the vertical distance between these two points will be used to calibrate the length. Therefore, you need to know one real vertical scale between two points on the image. For example:

(i) the span of the supports is 6 inches

(ii) the outer diameter of the shock tube is 5 inches

The process will repeat three times. Thus, totally you will pick six times. Please follow the instruction.

(4) Then you can do real measurement. Normally, you need to measure the deformation shape of the front face for every image. For each image, you need to choose seven points on the front face. The code will let you pick up the top point of the front face first. Then it will let you pick up the bottom point of the front face. After this, the code will base on these two points to

draw seven lines with equivalent distance. Please pick up the points from the top to the bottom.

(5) The code will ask you to input the mass of the specimen.

(6) The code will ask you to input the name of the file which you want to save you data into.

APPENDIX C: SAFETY GUIDELINES FOR EXPERIMENTAL EQUIPMENT

<u>**SHOCK TUBE**</u>

1. Do not stand near shock tube when it is being fired
   a. Stand no closer than 30 feet in any direction
   b. Stand next to person who controls Helium Tank
2. Wear ear and eye protection
3. Warn everyone around you that shock tube is to be fired
   a. Make sure Fluids Labs and Microfluidics labs know
   b. Make sure no classes are going on in Design Studio
   c. Make sure Design Studio students are not there
      i. If Design Studio is occupied, and no class is going on, ask students to leave for the test
4. Double check to make sure no one is in specimen lab
5. Check to make sure door to outside is closed and locked
6. Have the shock tube area roped off prior to test
7. Place "warning sign" in front of Microfluidics lab door and close divider off to design studio
8. Be sure to yell "firing" when releasing gas and also around the pressure where the diaphragm is expected to burst
9. Make sure bolts are completely tightened in the enclosure at end of shock tube.
10. Make sure all lexan is in place and both sliding doors are closed
11. Attach vacuum if sample that is to be blasted will cause excessive debris
12. If for any reason someone comes within 30 feet of tube shut off gas immediately and ask person to leave

<u>Procedure For Running a Safe Shock Tube Experiment</u>

1. Load up cart in DPML lab with proper equipment that is to be used

a. Oscilloscope, High Speed Camera, proper cables, extension cords, duct tape, research notebook, pressure sensors, mylar sheets, etc

　　　　b. Ask someone to help you move the cart and camera

　　　　　　i. Under no circumstance is the High Speed Camera to be moved by less than 2 people.

　　　　　　ii. This includes loading and unloading the camera

2. Enter Shock Tube area through garage door and place cart in position

3. Set up Camera in proper position

4. Set up flash bulbs and/or proper lights

5. Attach cables to necessary components and to triggers

6. Once High Speed Camera and components are set up, then place sample in enclosure

　　　　a. Use rubber band for positioning and then tape the sample in place

　　　　b. Adjust camera for experiment and focus on sample

7. Set up computer software (Imacon200, or Photron SA1)

8. Trigger camera and adjust images accordingly

9. Once Camera and computer are in place, properly set up oscilloscope place pressure sensors in the shock tube

10. Make sure everything is turned on and set up properly for given test

　　　　a. Camera images and triggers for both oscilloscope and camera are dependent on the number of plies being used

11. Make sure mylar is in place between driver and driven section

12. Once mylar is in place and both the camera and oscilloscope are set up properly, double check sample and make sure it is in place and shock tube muzzle is touching it.

13. Check everything over one more time and make sure nothing triggered prematurely

14. Make sure tank is completely shut and **follow the safety rules**

15. If sample is known to make mess attach vacuum to enclosure tank Go to helium tank and slowly begin releasing gas into the shock tube

16. Remember to yell "firing" when loading and when burst is expected

17. Once sample has been blasted, shut off gas and proceed to checking the scope and camera for data

18. Make sure to save data to respected positions

    a. Camera data saved under "users"

    b. Oscilloscope data saved on floppy and then on your computer

        i. Double check to make sure data is there

19. Remove sample from shock tube and piece back together

    a. Once the piece pertaining to the sample have been collected and the sample put back together as well as possible, **take pictures**

        i. Remember the longer you wait the more time the sample has to creep back and lose shape…which means losing crucial information

APPENDIX D: ASTM STANDARDS

ASTM (D-882)

Standard Test Method for Tensile Properties of Thin Plastic Sheeting

---

ASTM INTERNATIONAL

Designation: D 882 – 02

Standard Test Method for
Tensile Properties of Thin Plastic Sheeting[1]

This standard is issued under the fixed designation D 882; the number immediately following the designation indicates the year of original adoption or, in the case of revision, the year of last revision. A number in parentheses indicates the year of last reapproval. A superscript epsilon (ϵ) indicates an editorial change since the last revision or reapproval.

These test methods have been approved for use by agencies of the Department of Defense to replace Method 1013 of Federal Test Method Standard 406.

1. Scope *

1.1 This test method covers the determination of tensile properties of plastics in the form of thin sheeting, including film (less than 1.0 mm (0.04 in.) in thickness).

NOTE 1—Film has been arbitrarily defined as sheeting having nominal thickness not greater than 0.25 mm (0.010 in.).

NOTE 2—Tensile properties of plastics 1.0 mm (0.04 in.) or greater in thickness shall be determined according to Test Method D 638.

1.2 This test method may be used to test all plastics within the thickness range described and the capacity of the machine employed.

1.2.1 *Static Weighing, Constant-Rate-of-Grip Separation Test*—This test method employs a constant rate of separation of the grips holding the ends of the test specimen.

1.3 Specimen extension may be measured in these test methods by grip separation, extension indicators, or displacement of gage marks.

1.4 A procedure for determining the tensile modulus of elasticity is included at one strain rate.

NOTE 3—The modulus determination is generally based on the use of grip separation as a measure of extension; however, the desirability of using extensometers, as described in 5.2, is recognized and provision for the use of such instrumentation is incorporated in the procedure.

1.5 Test data obtained by this test method is relevant and appropriate for use in engineering design.

1.6 The values stated in SI units are to be regarded as the standard. The values in parentheses are provided for information only.

1.7 *This standard does not purport to address all of the safety concerns, if any, associated with its use. It is the responsibility of the user of this standard to establish appropriate safety and health practices and determine the applicability of regulatory limitations prior to use.*

NOTE 4—This test method is similar to ISO 527-3, but is not considered

technically equivalent. ISO 527-3 allows for additional specimen configurations, specifies different test speeds, and requires an extensometer or gage marks on the specimen.

2. Referenced Documents

2.1 *ASTM Standards:*
D 618 Practice for Conditioning Plastics for Testing[2]
D 638 Test Method for Tensile Properties of Plastics[2]
D 4000 Classification System for Specifying Plastic Materials[3]
D 5947 Test Methods for Physical Dimensions of Solid Plastic Specimens[4]
D 6287 Practice for Cutting Film and Sheeting Test Specimens[4]
E 4 Practices for Force Verification of Testing Machines[5]
E 691 Practice for Conducting an Interlaboratory Study to Determine the Precision of a Test Method[6]
2.2 *ISO Standard:*
ISO 527-3 Plastics—Determination of Tensile Properties—Part 3: Test Conditions for Films and Sheets[7]

3. Terminology

3.1 *Definitions*—Definitions of terms and symbols relating to tension testing of plastics appear in the Annex to Test Method D 638.

3.1.1 *line grips*—grips having faces designed to concentrate the entire gripping force along a single line perpendicular to the direction of testing stress. This is usually done by combining one standard flat face and an opposing face from which protrudes a half-round.

3.1.2 *tear failure*—a tensile failure characterized by fracture initiating at one edge of the specimen and progressing across the specimen at a rate slow enough to produce an anomalous load-deformation curve.

---

[1] These test methods are under the jurisdiction of ASTM Committee D20 on Plastics and are the direct responsibility of Subcommittee D20.10 on Mechanical Properties.

Current edition approved April 10, 2002. Published June 2002. Originally published as D 882 – 46 T. Last previous edition D 882 – 01.

[2] *Annual Book of ASTM Standards*, Vol 08.01.
[3] *Annual Book of ASTM Standards*, Vol 08.02.
[4] *Annual Book of ASTM Standards*, Vol 08.03.
[5] *Annual Book of ASTM Standards*, Vol 03.01.
[6] *Annual Book of ASTM Standards*, Vol 14.02.
[7] Available from American National Standards Institute, 25 W. 43rd St., 4th Floor, New York, NY 10036.

---

*A Summary of Changes section appears at the end of this standard.

1

ASTM (D-6287)

Standard Practice for Cutting Film and Sheeting Test Specimens

Designation: D 6287 – 05

Standard Practice for
Cutting Film and Sheeting Test Specimens[1]

This standard is issued under the fixed designation D 6287; the number immediately following the designation indicates the year of original adoption or, in the case of revision, the year of last revision. A number in parentheses indicates the year of last reapproval. A superscript epsilon (ε) indicates an editorial change since the last revision or reapproval.

1. Scope*

1.1 This practice covers equipment and techniques for cutting film and sheeting specimens for testing.[2] The specimens are nick-free, non-stretched and can be rapidly prepared.

1.2 The values given in SI units are to be considered the standard. The values given in brackets are for information only.

1.3 *This standard does not purport to address all of the safety concerns, if any, associated with its use. It is the responsibility of the user of this standard to establish appropriate safety and health practices and determine the applicability of regulatory limitations prior to use.*

NOTE 1—There is no similar or equivalent ISO standard.

2. Referenced Documents

2.1 *ASTM Standards:* [3]
D 882 Test Methods for Tensile Properties of Thin Plastic Sheeting
D 2838 Test Method for Shrink Tension and Orientation Release Stress of Plastic Film and Thin Sheeting
F 88 Test Method for Seal Strength of Flexible Barrier Materials

3. Significance and Use

3.1 Many test methods including Test Methods D 882, D 2838 and F 88 require the use of narrow strips of varying length. The quality of the sample preparation directly affects test results. This practice describes two techniques for preparing samples with straight, clean, parallel edges with no visible imperfections.

NOTE 2—After cutting, each specimen should be examined visually to insure the edges are undamaged (free of nicks). On a periodic basis specimen edge quality should be evaluated by microscopic examination. To determine when cutting blades need to be replaced or sharpened, a control chart of tensile strength and percent elongation at break (see Test Method D 882) of a uniform material may be maintained. Tensile strength and percent elongation at break will decrease as the quality of specimen cutting decreases.

4. Apparatus and Materials

4.1 *Procedure A*—A hand rotatable drum cutter (Fig. 1) containing a 12.7 cm [5 in.] diameter drum with grooves at 12.7 mm [0.5 in.] intervals and a blade holder allowing a blade to ride in each groove or be raised above the groove.[4]

NOTE 3—Plas-Tech in Boston offered a rotary drum cutter in the 1950's and 1960's which was shown to be an excellent instrument with respect to yielding nick free non-stretched film specimen(s) at high rates.[5] However, Plas-Tech disappeared in the late 1960's and the cutter with them. This type of cutter has been redesigned to meet current government regulations and retain its original desirable characteristics plus additional improvements.

4.2 *Procedure B*—A dual blade shear cutter (Fig. 2) with parallelism tolerances within 0.0254 mm [0.001 in.]. The cutter cuts individual strips of a particular sample width.

4.3 *Scissors.*

4.4 *Marker.*

4.5 *Tape.*

5. Procedure

5.1 *Procedure A*:

5.1.1 Cut film or sheeting (with scissors) approximately 30 by 30 cm [12 by 12 in.] or desired size within these dimensions. It is recommended to cut only an individual (single) sheet of film.

5.1.2 Mark or number all samples as to identity, direction with respect to material flow, etc.

5.1.3 Place sample on work surface in desired direction and place a strip of tape on the sample edge with half the width of the tape overlapping the edge to enable the tape to adhere to the drum of the cutter.

5.1.4 Remove the taped sample from the work surface and place taped edge on the drum of the cutter below the blade holder allowing the sample to lie across the top of the cutter.

---

[1] This practice is under the jurisdiction of ASTM Committee D20 on Plastics and is the direct responsibility of Subcommittee D20.19 on Film and Sheeting.
Current edition approved March 1, 2005. Published March 2005. Originally approved in 1998. Last previous edition approved in 1998 as D 6287 - 98.
[2] This practice does not cover all types of techniques which may be used for cutting film and sheeting specimens.
[3] For referenced ASTM standards, visit the ASTM website, www.astm.org, or contact ASTM Customer Service at service@astm.org. For *Annual Book of ASTM Standards* volume information, refer to the standard's Document Summary page on the ASTM website.

[4] The sole source of supply of the rotary drum film and sheeting cutter known to the committee at this time is Zebedee Corporation, P.O. Box 395, Landrum, SC 29356. If you are aware of alternative suppliers, please provide this information to ASTM International Headquarters. Your comments will receive careful consideration at a meeting of the responsible technical committee [1], which you may attend.
[5] Patterson, Gordon D., "An Interlaboratory Study of Cutting Plastic Film Tension Specimens," *Materials Research and Standards*, April 1964, p. 159.

*A Summary of Changes section appears at the end of this standard.

1